Spectral Element Methods for Predicting the Die-Swell of Newtonian and Viscoelastic Fluids

by

Giancarlo Russo

A dissertation submitted for the degree of Philosophi Doctor of Cardiff University

CARDIFF UNIVERSITY, CARDIFF

School of Mathematics

25 September 2009

Declaration

This work has not previously been accepted in substance for any degree and is not being concurrently submitted in candidature for any degree.

Signed _____ (candidate)

Date _____

Statement 1

This thesis is the result of my own investigations, except where otherwise stated. Other sources are acknowledged by giving explicit references. A bibliography is appended.

Signed _____ (candidate)

Date _____

Statement 2

I hereby give consent for my thesis to be available for photocopying and for inter-library loan, and for the title and summary to be made available to outside organizations.

Signed _____ (candidate)

Date _____

Acknowledgements

First of all, I wish to thank Tim Phillips for his constant and encouraging supervision during the past years. He has always found the right words at the right time, to give me a boost when I was a bit lazy, to encourage me when I felt a bit down and to teach me what research is about. Working with Tim has been a pleasure and a privilege. I wish him all the best and I truly hope we will keep collaborating in the future. I wish also to thank Russell Davies and Mike Webster for agreeing in being my examiners, as well as J.E. Jones for his invaluable work in chairing the viva.

Thanks to the postgraduate crew I met at the School of Mathematics, they helped to make my life in Wales very comfortable from the beginning. In particular, I appreciated the patience of Mike, Benedetto and Ross in sharing the office with me!

Thank you to the people who gave me the chance to experience teaching and tutoring maths. In particular, thanks to Chris Davies, Marco Marletta and Rob Wilson for trusting me in helping their students.

Nat Inkson has been of great help in finalizing the implementation of the XPP model. I am grateful for all the discussions we had about rheology of branched polymers and a few other relevant aspects of life. I wish him all the best.
James Osborne is the guy who introduced me to the Advance Research in Computing at Cardiff (ARCCA). Thanks James, without your support and your advices my computational life would have been a nightmare!

Thanks to all the folks I have met during my numerous trips, the people who hosted me and the people I hosted. My constant (and perhaps too much) travelling and all the wonderful experiences which came with it would have not been possible without Couchsurfing.

Thank you to all the friends who made Cardiff a special place. Thanks

to Federica, Lorenzo, Lydia, Raul, Renato, Tadas, Valentina, Vilija, the whole basketball crew, Marcus and David for being amazing landlords and remarkable guests, and all the others who reached Cardiff later on or just for a while. Without you the past four years would have been a different story.

Special thanks to Mikol, who, beside being a good friend, has also had the patience to be my housemate, and to Stefano for sharing, since the very beginning and among few other things, my tennis addiction and my questionable sense of humour.

Thanks, once again and five years later, to all the friends who have always been there since decades ago. Despite living thousands of miles apart, they want it or not, directly or indirectly, Roberto, Antonello, Stefania, Vincenzo, Flora, Antonio, Valentina, Davide, Enrica, Pancrazio, Wanda, Gianluca, Daniela, Carletto, Roberta, Angelo, Prospero, Sale, Bruno, Michele, Lello and Andi are a constant presence in my life.

I am extremely grateful to Saulius, Zita, Matas, Vaida, Rita and Aušra for making Lithuania a second home.

I will never be able to properly thank my family for loving me despite my constant attitude to run away! Their support has been invaluable, but of course this is no news. They have been there for thirty years and they will be there for much longer.

A special, deep thought goes to Stefania, Vincenzo and someone else about whom, as of now, we only know that he will be named Edoardo. To him this thesis is dedicated.

And to Ieva, for whom words are simply not the right tool.

Summary

This thesis is concerned with the development of numerical methods for free surface problems. In particular, the die-swell problem is analyzed for Newtonian and viscoelastic fluids. For several materials comparisons with experiments are presented. The viscoelastic models explored are the Upper Convective Maxwell model, single and multi-mode Oldroyd-B and the single and multi-mode eXtended Pom-Pom models.

The numerical method employed is based on a spectral element method. The time marching scheme follows a pseudo-transient approach. Discretization in time is performed by means of the Operator Integration Factor Splitting method of first and second order. The free surface evolves according to an Adams-Bashforth scheme of order three. Comparison with first and second order schemes are also presented for the Newtonian case. The viscoelastic scheme is uncoupled. The fully discretized constitutive equation is solved using a Bi-Conjugate Gradient Stabilized method, while the mass and momentum equations are solved simultaneously by means of the Conjugate Gradient method. Preconditioners are used to accelerate the inversion process.

The die-swell of a Newtonian fluid is investigated. The physical interpretation of the phenomenon for Newtonian fluids is also revisited, with the goal of reanalyzing findings from the literature and enrich them by means of specifically addressed numerical simulations. The effect of inertia and surface tension are considered. Analysis of convergence is performed and comparison with available results are presented.

Numerical simulations of viscoelastic die-swell are performed for the UCM, Oldroyd-B and XPP models. The effect of elasticity is analyzed through the stress fields, normal stress difference, pressure drops and swelling ratios. For the Oldroyd-B and XPP models, several materials are fully characterized for quantitative comparisons. For the XPP model, the effect of orientation and polydispersity on extrusion is discussed.

Contents

Chapter 1

Introduction

In this very first chapter of the thesis we provide a background to the field of rheology. An historical review of rheology is given in in §1.1; the rapid developments in numerical methods following the increase in computational power over the past few decades is then highlighted in §1.2. In the same section the framework and the aim of the research in this thesis is presented. In §1.3, a general description of the numerical algorithm and the computer code developed is summarized. Finally, in §1.5 the content of the thesis is summarized, addressing the main problems that will be studied.

1.1 A brief history

The word Rheology comes from the Greek "$\rho\varepsilon\iota$", meaning "flows". While in philosophy the concept of "everything in a state of flux" is attributed to Heraclitus, the name Rheology was coined by E. C. Bingham, Professor of Chemistry at Lafayette College, Pennsylvania. He introduced the concept of yield stress explained in §2.4; the Bingham plastic is named after him.

The idea was that every substance can either deform elastically or flow viscously depending on the timescale of the phenomenon. In other words, everything flows if we wait long enough. Bingham, together with another Professor of Chemistry at the University of Reading, G. W. Scott-Blair, and a mathematician from Israel, M. Reiner, were among the founders of the

Society of Rheology in 1929. This had a great impact in the recognition of Rheology as a distinct branch of fluid mechanics.

It is not surprising that the call for a scientific effort towards the systematic study of rheology came from chemists, since the explanation for the rheological behaviour of fluids like polymer melts or concrete lies in the molecular structure of the material. The key was (and still is) to understand how, when following neither Newton's equation of viscosity nor Hooke's elastic law, a certain material would react when a stress is applied. Once again, this initiated the search for appropriate models.

Despite empirical evidence that led scientists like Maxwell and Lord Kelvin (see §2.6) to deduce their constitutive relations already in the nineteenth century, it was not until the second post-war period that a rigid and axiomatic approach to constitutive modelling was proposed. J. G. Oldroyd [90] made a huge contribution in suggesting several principles to be satisfied by a constitutive relation, and eventually proposed one himself, the so-called Oldroyd model (see §2.6). Following Oldroyd, W. Noll [89] provided an alternative and axiomatic framework which is still widely used.

Since the 1950's several modelling philosophies flourished. They were usually the outcome of either new challenges posed by new materials or an increase in computational power. For instance, different models arise whether we analyze a material at a microscopic level (molecular dynamics), or at a macroscopic level (continuum mechanics); whether we need a description of the recent past of the flow (differential models) or its whole history (integral constitutive equations). Entire families of models have been developed, and, as always happens, there is no best model, but only models that are more suitable than others for a certain problem. Chapter 2 describes in detail a few differential macroscopic models.

1.1.1 The High Weissenberg Number Problem (HWNP)

Computational power has dramatically increased over the last three decades. The task of solving numerically any of the models, and therefore the asso-

ciated fluid mechanics problems, is the remit of the field of Computational Rheology. This represents in fact the combined effort of understanding and investigating the dynamics of non-Newtonian fluids by means of numerical analysis and computational methods. The monograph of Owens and Phillips [94] records the evolution of computational rheology, analyzing the biggest challenges this new branch of computational fluid dynamics poses. A vast part of the book reviews benchmark problems and how a whole variety of numerical approaches has been more or less successful in simulating those test flows. A whole chapter of the book is then devoted to what is seems to be the nightmare of every computational rheologist: the so-called High Weissenberg Number Problem (HWNP). As soon as enough powerful computational resources became available to scientists in order to set up a detailed and constructive development of numerical algorithms, the simulations of Non-Newtonian fluid flows revealed themselves being unable to investigate flows over a (often frustratingly low) threshold for Wi (or De). Above a certain value of the Deborah (or Weissenberg) number the algorithms simply did not converge.

A detailed analysis of the HWNP can be found, for instance, in Owens and Phillips [94]. Here we highlight the main issues related to it.

Twenty five years ago Mendelson et al. [81] first attempted to classify different possible ways of how a variable, say Y, in the flow, could vary with De, and how existence and stability properties could depend on a certain critical value De_{crit} . Apart from the ideal situation in which Y is a one-to-one function of De, a bifurcation De_{crit} has been hypothesized, in correspondence of which two families of solutions are possible for Y. The authors also identified a turning point situation, where De_{crit} is a maximum limit point, but solutions could still be found going back to lower De. An "ultimate limit" configuration, in which the limit De_{crit} marks the very last chance of observing a solution whatsoever has been then highlighted by Brown et al. [18] and Keunings [62].

It is broadly accepted that the reasons behind the HWNP are to be sought

in the numerical approximation of viscoelastic problems. Among the several causes identified as responsible for numerical breakdown above a threshold value of the Weissenberg number, some do not depend on the particular flow we are looking at (as it could be for a flow with steep boundary layers or singularities). First of all, the system of equations governing the flow, in the most general case, is of mixed hyperbolic/elliptic/parabolic type. This is itself a problem because some numerical schemes are not appropriate for mixed systems of PDEs. Moreover the choice of finite dimensional spaces in which the variables are approximated has to be chosen carefully, otherwise spurious oscillations could propagate into the flow domain. In fact, compatibility has to be satisfied between velocity and pressure fields [2, 17] and between velocity and stress fields [41, 40]. Moreover, finite dimensional compatible spaces are also required [73]. Last, but not least, although the constitutive equation does preserve the positive definiteness of the extra stress tensor (or the conformation tensor) in its continuous version, numerical algorithms often cannot ensure this property is satisfied by the discrete solution. This observation, together with the fact that polynomial-based algorithms tend to create oscillations when trying to approximate the highly steep stress profiles often occurring in viscoelastic flows, have been the main reasons behind the idea of approximating, rather than the conformation tensor itself, its matrix logarithm. Fattal and Kupferman [34] first proposed this approach in 2004 and a year later supported it with numerical results tested on the lid driven problem [35]. Later on, together with Hulsen [55], they applied such a formulation to perform simulations of the flow past a cylinder using a discrete stress splitting technique together with discontinuous Galerkin method.

A lot of effort has been devoted to computational rheology in the last decade, mainly because most of the problems involving viscoelastic fluids are theoretically intractable due to the complexity of the constitutive equations. Moreover, the availability of accurate predictions, aided more and more by a huge increase in computational power, has had an enormous influence on the fields. However, this is not preventing researchers from carrying on investigating different fluids and proposing more and more accurate mathematical

representations of their chemical and physical properties, as described in §2.7.4.

1.2 Framework of this research and aim of the thesis

The numerical simulation of viscoelastic flows is of primary interest because of they pervade our everyday lives. Non-Newtonian models have been developed to help us achieve a more realistic understanding of the physics of most liquids whose structure cannot be approximated at all by Newton's law of viscosity. To give a generic flavour of the world spinning around computational rheologists we describe some of the benchmark problems Owens and Phillips [94] presented in their monograph. We will not present many details at this stage, because these phenomena are not the particular subject of the present work. The interested reader will find a deep analysis and an exhaustive list of references in [94] to gain further insight into the problems.

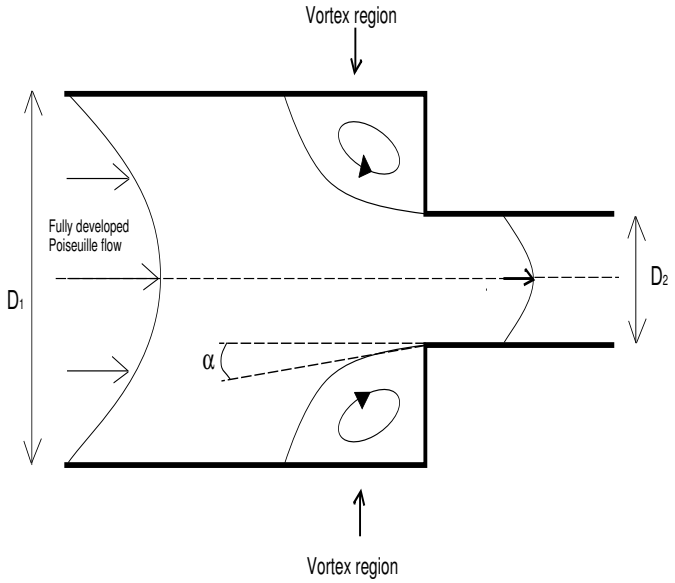

Figure 1.1: Flow through an abrupt contraction.

The first is the *abrupt contraction flow.* A fluid flows in a channel whose

width suddenly decreases. This is a very common geometry that is used in industry to extrude polymers. It is also present in various rheometric devices, e.g. the *capillary rheometer*. The most commonly used contraction ratios are $4:1$ and $8:1$. This problem involves a whole range of flow types: due to the pressure drop across the contraction, along the centreline a highly extensional region appears. On the other hand, a shear flow prevails at the walls. Finally, vortices arise in the corners. The response of an elastic fluid to these phenomena is anything but trivial. Investigating the response of a fluid to changes in flow rate and geometry generates a gold mine of information about the nature of the liquid. For example, the vortex activity increases with both contraction ratio and flow rate, and is reduced by rounding the re-entrant corner. Obviously, changes to the fluid characteristics have a great impact on the process. Increasing elasticity leads to a higher extensional response along the centreline, and might lead to a breakdown of the symmetry of the flow.

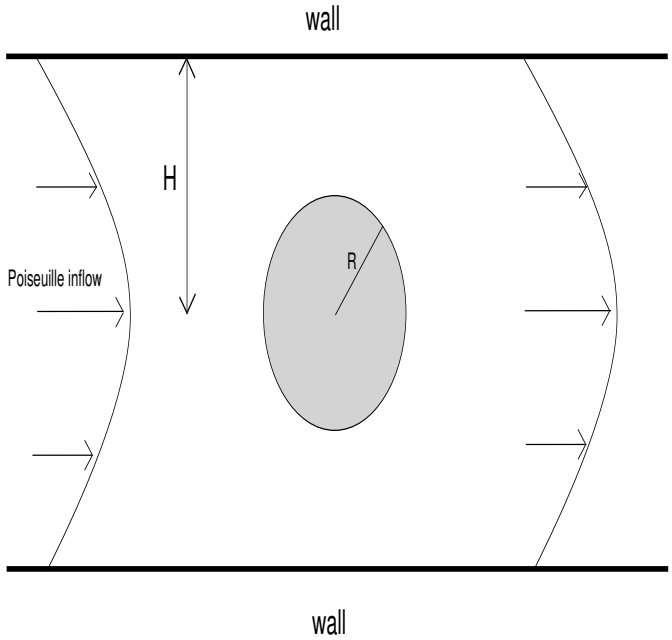

Figure 1.2: Flow past a cylinder in a confined channel.

The absence of geometrical singularities links the other three problems. The attention to the problem of *flow past a cylinder* arose principally to better understand the behavior of probes or sensors in an elastic fluid. Once again every sort of flow type is encountered: strong shear flow in the gap between the walls and the cylinder; highly extensional flow along the cylinder axis upstream and in the wake of the cylinder; formation of cavities behind the obstacle. Changes in elasticity and flow conditions once again are reflected through the drag coefficients, the streamline patterns, eventual breakdown of symmetry , length of the wake and so on. In particular, simulations with different models highlight the several configurations polymer chains can attain in different regions of the flow due to the different mechanisms different models are able to describe. Accurate computations of the stress boundary layers in the gaps between the cylinder and the walls remains a difficult problem.

The aforementioned boundary layers are concentrated along streamlines downstream of flow stagnation points. As far as polymer solutions are concerned, the effect of the concentration of the diluted particles on the flow downstream of a stagnation point has been studied by Harlen et al. [47]. They observed a sequence of birefringence structures which appear for values of the polymeric concentration above a certain threshold. In the case of a Finitely Extensible Non-Linear Elastic (FENE) model, they calculated the modification of the flow due to the transition from solid birefringent streamlines to pipe streamlines. They also determined the thickness of the birefringent strands as a function of the polymer concentration. Their calculations are in qualitative agreement with the experiments.

A similar problem is *flow past a sphere*, which is actually represented by a sphere falling in a tube filled with a liquid. Settling of suspensions and rheometry are two major applications. One of most fascinating features of this flow is the formation of so-called *negative wakes*. The vortex activity taking place in the wake of the falling sphere quickly decays to zero for Newtonian fluids; reversal flow, often several radii downstream, might instead be observed in the viscoelastic case. Different explanations have been proposed

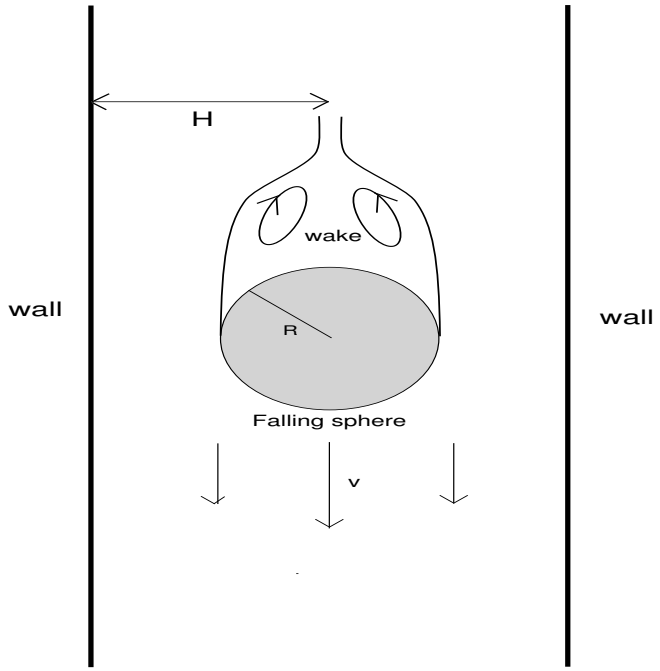

Figure 1.3: Sphere falling in a liquid.

for the formation of negative wakes. A few people thought the mechanism is due to the geometry of the flow, while the majority agree that both elasticity and shear-thinning are necessary for the presence of negative wakes. Again we refer to [94] and references therein for further details.

The last benchmark problem comes from automotive industry, and aims to assess the performance of lubricants over a range of engine operating conditions. The *flow between eccentrically rotating cylinders*, also known as the *journal bearing problem*, became important in computational rheology when it was thought that the introduction of elasticity in lubricating oils could have a beneficial effect on the load-bearing characteristics of the bearing. Results from Li et al. [67] showed that, especially when the eccentricity ratios are large (i.e., when the journal is really close to the bearing), elasticity tends to increase the minimum oil film thickness (MOFT), producing a sort of *safety cushion*. Moreover, due to the large negative pressures produced in the journal bearing, the lubricant oil vaporizes, leading to cavitation.

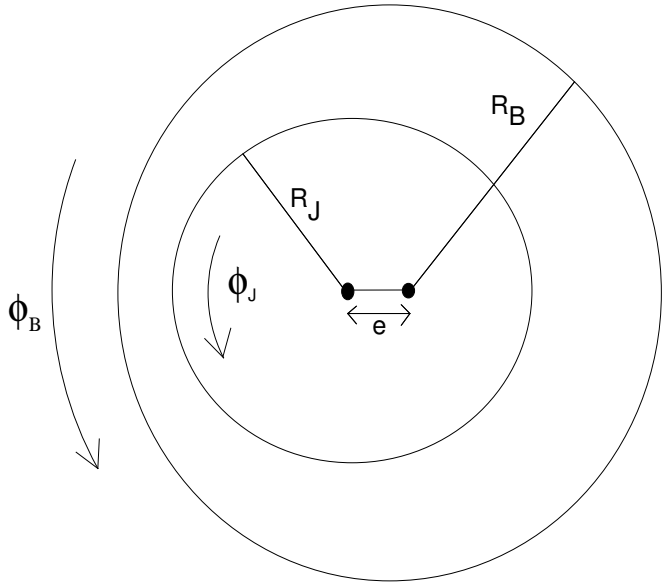

Figure 1.4: Flow between eccentrically rotating cylinders. The different angular velocities of the journal and the bearing are ϕ_J and ϕ_B respectively.

Another problem which is considered a benchmark problem by some is the so-called *stick-slip* problem. A fluid flows in channel in which, at a certain position, the no-slip boundary condition is removed. Therefore the particles, from sticking to the wall start slipping. The velocity profile then changes from parabolic to becoming flat, a plug flow. Even if this thesis is not directly related to any benchmark problem, the die-swell problem shares with the stick-slip problem the sudden removal of the no-slip condition at the exit. In the die-swell case the wall is also removed. In §4.2 a few remarks on the stick-slip problem will be made, particularly related to the occurrence of the singular point which marks the change in the boundary condition.

The present work investigates free surface flows of Newtonian and non-Newtonian fluids. Free surface flows are encountered in every type of industrial application. Bubble dynamics in foams, droplet deformation in gas dynamics, lubrication, injection moulding, surface wetting and coating, me-

teorology and many others. Moreover, free surface flows are at the core of two of the most commonly used procedures in rheometry: filament stretching, performed by means of the *extensional rheometer*, and extrusion, where a *capillary rheometer* is used in most cases. We give here a review of the most significant issues regarding the filament stretching problem. Roughly

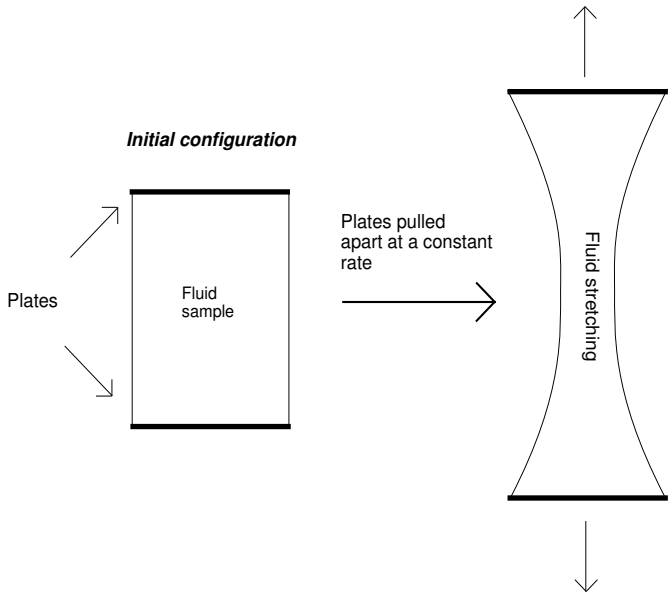

Figure 1.5: A sample of fluid is stretched.

speaking, the extensional rheometer is an instrument in which two plates which have a sample of fluid between them are pulled apart. This happens quite often in industrial polymer processing as well as in rheometry. In the latter case, the main goal is to reproduce a flow which is almost ideally extensional. Some extensional rheometers keep the bottom plate fixed while pulling only the top one. Others proceed with both symmetrically. The whole process is clearly started by velocity fields applied to the plates. Usually the plates are pulled apart at an exponential rate, and their motion obeys evolution equations of the following type:

$$L(t) = L_0 \exp(\frac{1}{2}\dot{\epsilon}t) \qquad V(t) = \frac{1}{2}\dot{\epsilon}L(t). \tag{1.1}$$

Looking at Fig. 1.5 it is obvious that the second equation in (1.1) provides

the only Dirichlet boundary conditions the problem requires. The rest of the boundary is free . On the fluid boundary, force balance free surface conditions will be applied. In the interior of the domain the field equations i.e. the mass and momentum conservation laws will hold, together with the choice of constitutive equation.

In Fig. 1.6 the filament has been stretched over a certain period of time t. On the basis of the new positions of the plates, namely the length of the filament $L(t)$, a strain rate $\dot{\epsilon}$ can be determined using equations (1.1). The relevant quantity, called the *Hencky strain*, can then be calculated as function of the new position $L(t)$:

$$\epsilon = \ln \frac{L(t)}{L_0} = \dot{\epsilon} t. \tag{1.2}$$

The first equality in (1.2) is actually the definition of the Hencky strain. It is also called natural strain, and it comes from integrating small increments of strain, say δl, over the total length. The larger the Hencky strain, the larger is the stretch that the fluid undergoes. A key point to underline regarding

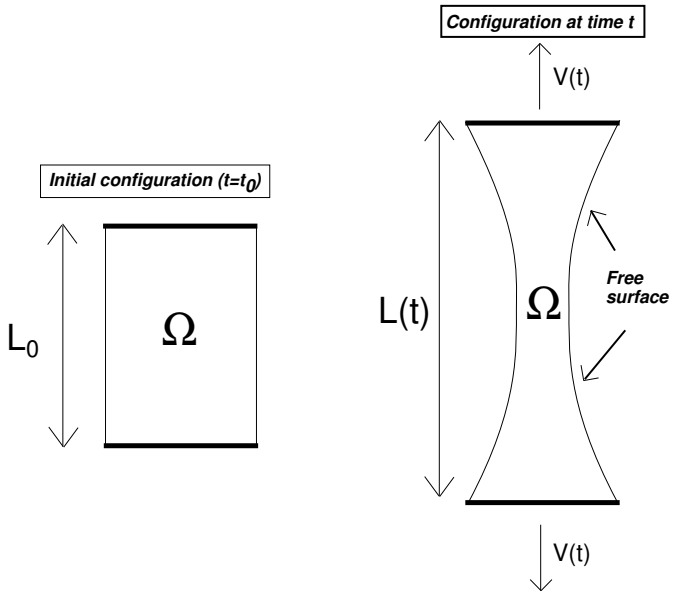

Figure 1.6: The evolution of the flow at time t.

this approach is that what happens in theory is that, if measurements are based only on the position of the plates, the whole column of fluid seems to experience the same strain rate, which would clearly be $\dot{\epsilon}$. Unfortunately, this is not what really happens. Different regions of the filament undergo different strain rates, so the flow is not homogeneous.

The approach described above is mostly used in industrial simulations. The reason is that in these tests the fluid dynamics is more relevant than the rheological properties of the fluid. On the other hand, if the ideal uniaxial extensional flow needs to be reproduced, a little bit more care is required.

The main purpose of an ideal uniaxial extensional flow is the measurement of the transient Trouton ratio. It is defined as the ratio of the extensional and zero shear viscosity:

$$Tr = \frac{\eta^{+}_{ext}(\dot{\epsilon}, t)}{\eta_{shear}}. \tag{1.3}$$

For Newtonian fluids its value is always three, due to the nature of Newton's law of viscosity. For viscoelastic fluids it might be orders of magnitude larger. In other words, this is a non-dimensional measure of the extensional viscosity as a function of the strain rate and time. When the measurement of this material function is of primary importance, then it has to be recalled that the filament stretching flow, as described above, is not ideal. In fact, the filament stretching rheometer suffers from an intrinsic problem. The ideal uniaxial extensional flow is achieved when the configuration is shear-free. This means that a perfectly elongated filament should look like a cylinder. When the plates are pulled apart, the initial cylinder obviously loses its configuration because of incompressibility and no-slip on the plates. Therefore, necking effects caused by shear flows show up near the plates. On the one hand enough strain rate is required to avoid these influencing the flow in the middle of the filament: on the other hand, larger strain rates mean longer filaments, which in turn means a smaller radius. In other words, the price to pay to obtain an almost ideally extensional flow in the middle of the filament is stronger and steeper necking effects near the plates.

Over the last fifteen years a substantial effort has been expended studying the extensional rheology of different fluids. The research group at the University of Wales, Swansea [22, 77, 116, 137], has focused on the prediction of filament stretching by means of their hybrid finite element/finite volume code, to test and compare different numerical techniques.

An extensive experimental research programme has been carried out in the past decade by a group in the Danish Polymer Centre based in Lyngby. They performed [4, 87, 88, 100] a number of experiments to investigate the extensional response of different types of polymers. Moreover they analyzed [48, 101, 5] different mechanisms for the growth of three dimensional instabilities in both experiments and simulations by distributing equally a number of perturbations on the circular rim on the bottom plate. Then they recorded pictures of the development of the instabilities.

Yao, Spiegelberg, McKinley and other collaborators [114, 115, 139, 140, 141] at Harvard and the M.I.T. focused on the dynamics of weakly strain-hardening fluids in stretching experiments. They also analyzed and reported failure and decohesion of the fluid sample from the plates under severe strain conditions. On the other hand, they paid particular attention to the influence of shear flow in the vicinity of the solid/liquid interface.

Another important centre of research on extensional rheology is Monash University, Australia, where in 1993 Tirtaatmadja and Sridhar [122] first proposed a type of extensional rheometer which has been widely used ever since. Research moved forward and focused on the investigation of the extensional properties of different constitutive models [123, 11]. Not surprisingly joint efforts from some of these groups also appeared [78, 11].

In this thesis, we focus our attention on the second phenomenon we mentioned, and which represents at the same time a challenging physical problem and a flow of industrial relevance: die swell of Newtonian fluids and extrusion of polymer solutions and melts.

1.2.1 The swelling phenomenon

Extrusion is a process which takes place every time a fluid is pushed through a die of a certain length. When the fluid leaves the tube it is said to be *extruded*. This process is performed daily in factories to extract food dough, concrete, polymer liquids. It also happens at much smaller scales in ink jet printers. Accurate numerical predictions of this type of flow aids engineers in optimizing both flow characteristics and design of extrusion devices. This obviously results in enhanced performances as well as massive savings in time and expense. Extrusion is also performed to collect data and analyze material functions and rheometric characteristics of various non-Newtonian fluids. The capillary rheometer is the most commonly used device.

This phenomenon is also referred to as *die-swell*. The reason is that the fluid expands when leaving the die. The measurement of this expansion, together with the tracking of the fluid surface, is of the utmost importance. The pressure drop is another quantity which is usually measured to better understand the physics of the flow. The investigation of these quantities, and their response to changes in geometrical and physical flow conditions and fluid characteristics are the ultimate aim of every simulation. This is exactly what is pursued in the present work.

Swelling takes place in every type of fluid. It is much more evident and significant in viscoelastic fluids, with peaks of well above 200%. On the other hand Newtonian fluids experience swelling in the range $13\% - 19\%$. Middleman and Gavis [84] first provided experimental evidence of swelling of a Newtonian fluid in the 1960's. They eventually found that a Newtonian fluid can also contract if the flow rate is sufficiently high. Since then the Newtonian case has been mostly used to test numerical schemes and used as a stepping stone to investigate the corresponding viscoelastic problem. For example, this was the approach of Batchelor et al. [7] and Nickell at al. [86] , who developed a finite element based code. Also Chang et al. [23] and Omodei [91, 92] pursued a similar approach, although the latter produced a remarkable number of simulations for many different flow conditions. Ho and Patera [50] tested their spectral element code while Horsfall [53] used

a finite difference approach. At the end of the day it turns out that the Newtonian die swell is not fully understood. The first half of Chapter 5 addresses this problem. A novel physical interpretation is proposed, supported by a complete set of numerical predictions.

The situation is slightly different for the viscoelastic case. The industrial importance of the problem energised the search for theoretical and numerical predictions. Almost forty years ago, Tanner [117] proposed a theoretical approach to the problem. The author revisited the theory recently and modified it to deal with different types of fluids [118, 120]. Together with Crochet and Keunings [28, 29], he was the pioneer of numerical studies on extrusion. On top of this, numerical and experimental work has been carried out over the last three decades. Liang [68, 69, 70, 71] analyzed experimental data of different types, tests several fitting equations, with the outcome of providing a remarkable set of informations and sources. Dangtungee and his collaborators [31, 30] do similarly, while Tomé and coauthors [124, 125] focused in the last years on extrusion as a benchmark free-surface problem for their marker-and-cell (MAC) code.

The second part of Chapter 5 is devoted entirely to the numerical simulation of extrusion of polymeric liquids. Different flow conditions are analyzed and different models are used. The Oldroyd-B [90] and the Upper Convected Maxwell fluids model polymer solutions. The eXtended Pom Pom model from Verbeeten et al. [132] is considered when investigating polymer melts. Whenever possible, numerical results are compared with predictions available in the literature and from experiments.

1.3 General description of the numerical code developed

The code developed to perform our simulations is written using Fortran language. Parts of the code, mainly involving iterative solvers and preconditioners, were developed by Xavier Escriva, Marc Gerritsma and Roel Van Os in Aberystwyth. A whole new scetion has been developed and imple-

mented to deal with free surface problems.

All the simulations were run either on the Condor network using a Visual Fortran compiler or on the Merlin servers at the Centre for Advanced Research in Computing at Cardiff (ARCCA) using an Intel Fortran compiler.

1.4 Notation used in the thesis

In this thesis, plain characters are used for scalar variables, arrows denote vectors (e.g. $\vec{F}$) and bold characters denote tensors (e.g. $\boldsymbol{T}$). The only operations specified by symbols are the scalar product $\cdot$ (between vectors), the tensor product $\otimes$ and the dyadic product :(between tensors). When no symbol is used, it is assumed that the standard product between two object of the same type is used. For example, multiplication between scalar or row-by-column multiplication between second order tensors. All the remaining symbols and notations used are specifically defined.

1.5 Contents of the thesis

This work is organized as follows. In Chapter 2 the continuum mechanics background is provided. The mathematical description of fluids in terms of the conservation laws is presented, together with physical explanations of the main variables involved. A review of models then follows, from the Navier-Stokes equations to more sophisticated models for polymer melts including mechanisms such as constraint release and chain stretch. The numerical methods we employ is the subject of Chapter 3. The spatial and temporal discretization of the problem is explained in depth, together with the description of the preconditioning and upwinding techniques utilized. Compatibility and stability issues are addressed and the numerical algorithm is described, with particular attention to the treatment of the free surface. Chapter 4 is devoted to the Newtonian die swell problem. A novel physical interpretation of the purely viscous phenomenon is proposed and supported by numerical simulations. Numerical simulations of the extrusion of polymer solutions and melts are presented in Chapter 5. Comparison with

theory and other numerical results are reported. A possible interpretation of the non-dimensional parameters related to chemical structure of the fluid is investigated. A quantitative approach is finally attempted in Chapter 6. A few materials are characterized and quantitative comparisons are performed. A discussion on the relationship between the fitted dimensional parameters and the chemical structure of the materials is presented, often interfacing with the previous chapter. Finally, conclusions are drawn in Chapter 7.

Chapter 2

Modelling Continuum Mechanics

This chapter is devoted to the description and analysis of different models used to represent continuous media. A first definition and classification of fluids will be given in the introduction. In §2.2 some theoretical fundamentals will be described, on which most of the physics described in the models rely.

Different constitutive equations leading to different models will be then presented. Section §2.3 deals with the Newtonian constitutive law, and the corresponding Navier-Stokes equations. Non-Newtonian fluids will be characterized in Section §2.4, and particular care will be given to viscoelastic fluids, which will be analyzed in Sections §2.6 and §2.7.

2.1 Introduction

In this thesis the approach adopted for modelling fluids is *macroscopic*. This means that the portion of fluid we will be analyzing will always be large enough for the distance between different molecules to be neglected. Another way of putting this is calling the medium a *continuum*, so the first thing we briefly turn our attention to in this chapter is the word *continuum*. The definition of a continuum material depends on the mathematical property

of continuity of its density; precisely, if we call V a small volume of the material corresponding to a certain region S, and m its mass, then the density of that material in the region S will clearly be

$$\rho = \frac{m}{V}.$$

Mathematical continuity of this quantity will simply mean that if we squeeze the volume to an infinitely small value V_ϵ, then the following limit has to exist:

$$\lim_{V \to V_\epsilon} \rho.$$

To be fair, this would mean that our medium is a continuum with respect to the density. For our purposes we will assume that our media are continua with respect to all the quantities involved in our problem; we will not really take into account temperature because all the phenomena analyzed will be isothermal. This is also the reason why, among the conservation laws described in the next section, the principle of conservation of energy will not be mentioned.

Any continuous medium can be subject to two different types of forces: *body* and *surface* forces. Body forces are usually effects of external causes acting from a certain distance, such as gravity, or magnetic fields. Surface forces act instead on any surface defined within the fluid. If we think of a point A and a small surface S surrounding it, then we define the *average stress* to be the ratio between the surface force $\vec{F}$ acting on S and the surface itself:

$$\vec{T} = \frac{\vec{F}}{S}.$$

Since the surface S has two sides, one will be uniquely determined by its outward normal $\vec{n}$; then the component of the stress aligned with $\vec{n}$ is called the *normal stress*, while the component lying in the tangential direction is named the *shear stress*. We can now state the definition of a viscous fluid; we remark that such a definition does not apply to viscoelastic fluids, and will be the starting point of our primary classification.

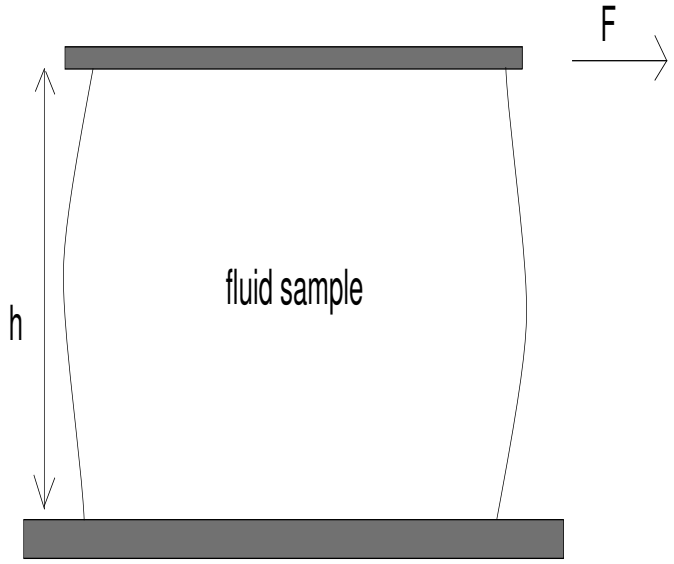

Figure 2.1: Shear stress experiment.

A fluid is a continuous medium which cannot support any shear stress while at rest.

This definition can be better understood with reference to Fig. 2.1. In the figure there is a sample of a material at rest, between two parallel plates. If F is a generic stress applied to the top plate, then the material is a fluid if the plate moves in the same direction as the stress, no matter how small the stress applied is. In other words, a fluid cannot support *any* stress.

Immediately, and fairly intuitively, we wonder how the stress applied relates to the velocity of the plate. The stress is proportional to the plate velocity V, and inversely proportional to the distance between the plates h through a constant called *dynamic viscosity*, i.e.

$$T = \mu \frac{V}{h}. \tag{2.1}$$

Since the shear stress is a surface force, equation (2.1) applies also to two different but very close layers of fluid moving at a different speed; if dy

is the distance between them, and du is the gradient of velocity, then (2.1) becomes

$$T = \mu \frac{du}{dy}. \tag{2.2}$$

In general, for a multi-dimensional flow, (2.2) is replaced by

$$\boldsymbol{T} = \mu(\nabla \vec{u} + \nabla \vec{u}^T). \tag{2.3}$$

A detailed description of the stress tensor, its properties and its relation to the deformation tensor will be given in §2.2 and §2.2.2.

Equation (2.3) is called *Newton's law of viscosity*, and fluids obeying this law are therefore called Newtonian. On the other hand (2.3) is a mathematical statement, and no one can be sure that it holds for all the fluids on earth. The first distinction comes out then: Non-Newtonian fluids are fluids to which (2.3) does not apply. This class of fluids is by far the broadest in nature; in fact, in §2.4 it is explained why no fluid is really Newtonian. On the other hand, for example, air, water and petroleum, the three most abundant fluids, agree really well with (2.3), and therefore are considered to be Newtonian from a physical point of view.

Viscoelastic fluids are a particular case of Non-Newtonian fluids. Their feature is to experience partial elastic recovery a certain amount of time after the stress has been removed. They are called sometimes *fluids with memory*, as if they could *remember* to recover.

Generally Non-Newtonian fluids are all those for which the viscosity μ is not constant but is a function of the rate of deformation tensor $\boldsymbol{d} = \frac{1}{2}(\nabla \vec{u} + \nabla \vec{u}^T)$.

Mathematical fundamentals, properties and models are described in the rest of the chapter.

2.2 Fundamentals

In this section, the equations governing the balance between different forces acting on a fluid are derived. The description of the stress is given, and the momentum equations will be deduced from investigating a small volume of fluid of cubic shape; the concept of *stress in a point* will be then pointed out through the analysis of an elementary tetrahedron of matter. This will help in defining the concept of *stress as a tensor*, which is crucial to understanding the meaning of *constitutive equations*. Together with the analysis of deformation and the application of conservation laws, the fields equations will be finally derived.

We remark again that in the constitutive equation lies the physical difference between Newtonian, Non-Newtonian and viscoelastic fluids. This will be explained and analyzed in Sections §2.3-§2.7.

2.2.1 The elementary cube

The basis of the momentum equations is Newton's second law:

$$m\vec{a} = \vec{G} + \vec{S}, \tag{2.4}$$

where $\vec{G}$ and $\vec{S}$ represent the body and surface forces respectively.

In Fig. 2.2 an infinitely small cube of fluid is highlighted in a Cartesian frame of reference, and $\vec{T}_x$ is the stress acting on the surface perpendicular to normal $\vec{i}$, namely the x direction. By the definition of stress as force per unit area, the force in the x direction on that surface can be expressed in terms of the Cartesian components of $\vec{T}_x$ as follows:

$$\vec{F}_x(x + \Delta x) = (\vec{i}T_{xx} + \vec{j}T_{xy} + \vec{k}T_{xz})\Delta y \Delta z. \tag{2.5}$$

Repeating the same analysis for all the sides, we have the resultant surface force acting on the whole cube, whose x-component is

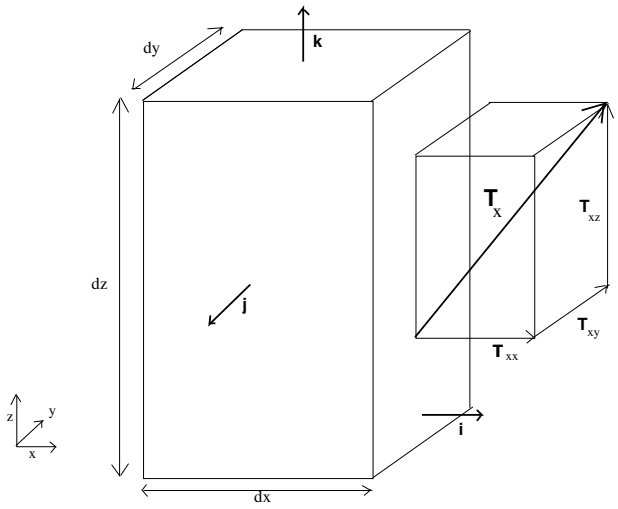

Figure 2.2: Elementary cube of fluid.

$$S_x = \Big(\frac{T_{xx}(x+\Delta x) - T_{xx}(x)}{\Delta x} + \frac{T_{yx}(y+\Delta y) - T_{yx}(y)}{\Delta y} + \tag{2.6}$$

$$+\frac{T_{zx}(z+\Delta z) - T_{zx}(z)}{\Delta z}\Big)\Delta x \Delta y \Delta z. \tag{2.7}$$

This force wis added to the body force

$$G_x = g_x \rho \Delta x \Delta y \Delta z \tag{2.8}$$

to balance the rate of change of momentum in the system expressed by

$$ma_x = a_x \rho \Delta x \Delta y \Delta z. \tag{2.9}$$

Now squeezing the cube to a point, namely taking the limit as the length of the sides approach zero, we can finally express the balance in the momentum equation:

$$\rho a_i = \rho g_i + \frac{\partial T_{ji}}{\partial x}, \tag{2.10}$$

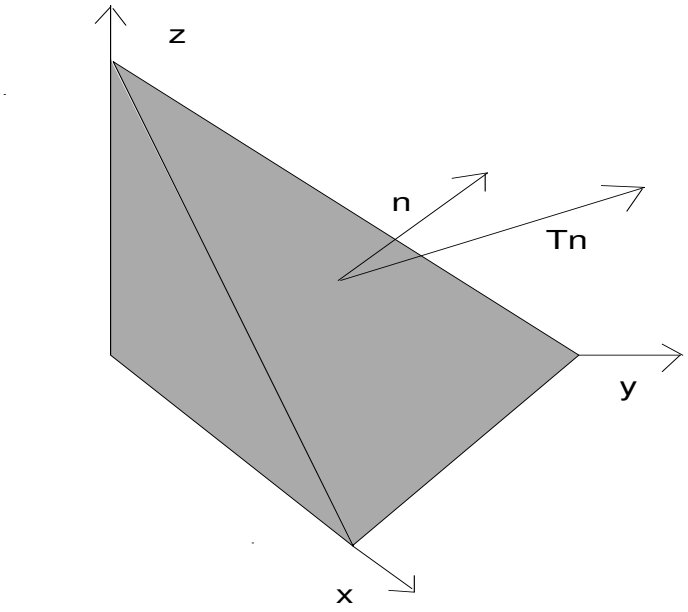

Figure 2.3: Elementary fluid tetrahedron.

in which the range and summation conventions are used and $x_1 = x$, $x_2 = y$ and $x_3 = z$.

2.2.2 The stress tensor

We now turn our attention on how to derive the stress on a generic plane provided the components T_{ij} are known on the other three sides of the tetrahedron (see fig. 2.3). We keep the index convention, so $\vec{T}_2$, the stress acting on the plane orthogonal do the y-direction is known, as well as $\vec{T}_1$ and $\vec{T}_3$. If A_n is the area of the plane P_n on which $\vec{T}_n$ is acting, then the force acting on the system is

$$-\vec{T}_1(n_1 A_1) - \vec{T}_2(n_2 A_2) - \vec{T}_3(n_3 A_3) + \vec{T}_n A_n + \rho V \vec{g}, \tag{2.11}$$

where $\vec{n} = (n_1, n_2, n_3)$ is the normal to P_n. If we now apply Newton's second law and divide by A_n with $\frac{V}{A_n} = h_n/3$, we obtain

$$\frac{\rho h_n(\vec{a} - \vec{g})}{3} = \vec{T}_n - \vec{T}_1 n_1 - \vec{T}_2 n_2 - \vec{T}_3 n_3.$$

As h_n approaches zero we finally obtain the following compact relation, in which the index notation is used again:

$$T_{nj} = T_{ij} n_i. \tag{2.12}$$

Equation (2.12) expresses the stress vector $\vec{T}_n$ acting on the generic plane P_n by mean of the components T_{ij} of the stress vectors acting on the planes orthogonal to the Cartesian frame of reference. The 3×3 matrix T_{ij} is called the *stress tensor.*

If we return to Fig. 2.3, we see that the stress acting on P_n has not been chosen to align with the normal $\vec{n}$ to give a generic description; but we can clearly rotate our frame of reference in such a way for this to happen. Of course, our directions will not be the original x_1, x_2 and x_3, but we will have new directions, always orthogonal, called *principal directions* of the stress tensor. From an algebraic point of view this means that

$$\vec{T}_n = \lambda \vec{n},$$

or, in terms of the stress tensor,

$$\det \begin{pmatrix} (T_{11} - \lambda) & T_{12} & T_{13} \\ T_{21} & (T_{22} - \lambda) & T_{23} \\ T_{31} & T_{12} & (T_{33} - \lambda) \end{pmatrix} = 0. \tag{2.13}$$

Once the three eigenvalues λ_1, λ_2, λ_3 are found, then the corresponding principal directions can be derived, and in this new frame of reference the stress tensor will clearly be diagonal with entries exactly λ_1, λ_2, λ_3, namely the *principal stresses.* From an algebraic point of view, finding the principal stresses is a problem of diagonalizing the stress tensor by similitude with principal directions as eigenvectors.

According to the definition of a fluid, we note that a fluid at rest is a case in which all the directions are principals, because no shear stress, namely, no extra-diagonal terms are allowed in the stress tensor. This being true in all frames of reference, we can deduce that for a fluid at rest the normal

stress components have the same value, which is negative and it is called the *pressure*. Another way to express this concept is Pascal's law:

In a fluid at rest, the pressure part of the stress tensor at a point is the same in all directions.

More details on fluid statics can be found, for example, in Chapter 3 of the book by Pnueli and Gutfinger [99].

2.2.3 The conservation law and the fields equations

The description of a fluid in motion is clearly more difficult than the description of a rigid body, because within the domain we are trying to analyze a fluid that can have completely different characteristics at different points. The key concept to tackle this issue is the idea of investigating a problem of fluid dynamics *following the system*; the mathematical theorem which expresses this idea is the *Reynolds transport theorem*.

Anyone interested in describing phenomena involving a thermodynamic system needs to know what is happening in that system at different times; mathematically this is translated into the knowledge of the rate of change of the relevant quantities with time. We express a quantity, say B, inside a volume V as the integral of its value per unit mass, say b

$$B = \int_V (\rho b)\, dV. \tag{2.14}$$

The rate of change of B would simply be $\frac{\partial B}{\partial t}$ in a rigid body, namely the rate of change of B in the volume V. However, when we are dealing with fluids we are *following* the system, and so we have also to take into account the flux of B from the volume V, which is caused by the fact that fluid particles are moving at a certain speed $\vec{u}$. These two features are elegantly merged by the concept of material derivative, $\frac{D}{Dt}$, defined as

$$\frac{D}{Dt}(\bullet) = \frac{\partial}{\partial t}(\bullet) + \vec{u} \cdot \nabla(\bullet) \tag{2.15}$$

By means of (2.15), the rate of change of a quantity is then calculated using the ***Reynolds transport theorem***:

$$\frac{D}{Dt}\int_V (\rho b)\, dV = \int_V \frac{\partial(\rho b)}{\partial t}\, dV + \int_S \rho b \vec{u}\cdot\vec{n}\, dS. \tag{2.16}$$

The two quantities whose rate of change with time we are interested in are mass and momentum, and the application of Reynolds transport theorem will give us the two conservations laws we need.

Conservation of mass simply requires b to be replaced by 1 in equation (2.16), since the mass per unit mass is clearly one; and since mass can neither be created nor destroyed, then we state the ***conservation law of mass***:

$$\frac{\partial}{\partial t}\int_V \rho\, dV + \int_S \rho\vec{u}\cdot\vec{n}\, dS = 0. \tag{2.17}$$

On the other side, momentum can be added or removed to the system, but always according to Newton's second law; this means that, expressing the rate of change of the momentum by Reynolds transport theorem, and balancing it with the resultant of body and surface forces, we can state the ***conservation law of linear momentum***:

$$\frac{\partial}{\partial t}\int_V \rho\vec{v}\, dV + \int_S \rho\vec{v}(\vec{u}\cdot\vec{n})\, dS = \int_V \rho\vec{g}\, dV + \int_S \vec{T}\, dS. \tag{2.18}$$

The two conservation laws above are integral laws, namely global laws, and despite their invaluable meaning, quite often are of no use if pointwise information are required. Thus *field equations* are introduced.

The concept of field comes from the idea of "sitting" on a point with coordinates (x_1, x_2, x_3) and seeing what happens there at all times. The relevant quantities then become dependent variables, while spatial and temporal coordinates are independent. A *flow field* will then have been completely described once the relevant fields, say velocity, pressure and stress of the fluid, are known at each point at all times. The field equations are derived from the two conservation laws (2.17)-(2.18) by applying the divergence theorem to the surface integrals, and removing the integral since the laws will

hold for any arbitrary control volume dV.

The conservation law of mass will then become the ***continuity equation***:

$$\frac{\partial \rho}{\partial t} + \nabla \cdot (\rho \vec{u}) = 0. \tag{2.19}$$

We will deal with incompressible flow, namely with constant density. Equation (2.19) will then simply become

$$\nabla \cdot \vec{u} = 0. \tag{2.20}$$

Moreover the conservation law of momentum will translate into the ***field equation of momentum***

$$\rho\Big(\frac{\partial \vec{u}}{\partial t} + (\vec{u} \cdot \nabla)\vec{u}\Big) = \rho \vec{g} + \nabla \cdot \boldsymbol{\sigma} \tag{2.21}$$

or

$$\rho\Big(\frac{\partial \vec{u}}{\partial t} + (\vec{u} \cdot \nabla)\vec{u}\Big) = -\nabla p + \rho \vec{g} + \nabla \cdot \boldsymbol{T}. \tag{2.22}$$

In Eq. (2.22) the stress tensor has been split into pressure terms, and the so called *extra-stress* (or *deviatoric*) tensor $\boldsymbol{T}$, namely, $\boldsymbol{\sigma} = -p\boldsymbol{I} + \boldsymbol{T}$ where $\boldsymbol{I} = (\delta_{ij})_{i,j=1,\dots,3}$. The unknowns of our problem are now clear: the pressure, which is a scalar, the velocity of the fluid, which is a vector, and the extra-stress tensor. We only have the two field equations so far, so to close the system a third relation is required. This is the ***constitutive equation***, which relates the extra-stress tensor to the *rate of strain tensor*, namely, to the gradient of the velocity. This is the equation which actually contains information about the nature of the matter we are studying, and it will be the subject of the rest of the chapter.

2.3 Newtonian fluids

A fluid has been defined as a continuum which cannot support a shear stress while at rest; this has to be true with respect to all the coordinates systems. A change of coordinate system can always be performed by means of shifting and angle-preserving rotations, this type of motion being exactly

rigid-body-like motion. This means that a bulk of fluid undergoing such type of motion, which is nothing more that a change of coordinates, will keep zero shear stress. For a fluid to exhibit shear stress a *deformation* (or *strain*) is needed. If $\vec{u}$ is again the velocity of the fluid particles, we define the *rate of strain tensor* by

$$\boldsymbol{d} = \frac{1}{2}(\nabla\vec{u} + (\nabla\vec{u})^T). \tag{2.23}$$

A brief analysis of deformation is provided for example by Pnueli and Gutfinger in [99] (chapter.5) while for a detailed description of the fundamental elastic properties of a continuum we refer to the monograph of Gould [44].

We are now in the position to extend the one-dimensional equation (2.2) to its three-dimensional generalised version; this is the first constitutive equation we find, and it defines a ***Newtonian fluid***:

$$\boldsymbol{T} = 2\mu\boldsymbol{d}. \tag{2.24}$$

In this constitutive relation the extra-stress tensor depends linearly on the rate of strain tensor.

2.3.1 The Navier-Stokes equations and the Reynolds number

We now combine the constitutive equation (2.24) with the field equation of momentum (2.22) to remove the stress from the problem. The outcome is one of the most famous equations in physics, which is named after the French scientist and engineer Claude-Louis Navier and the Irish physicist and mathematician George Gabriel Stokes:

$$\rho\Big(\frac{\partial\vec{u}}{\partial t} + (\vec{u}\cdot\nabla)\vec{u}\Big) = -\nabla p + \rho\vec{g} + \mu\triangle\vec{u}. \tag{2.25}$$

In the literature this is very often coupled with the continuity equation (2.20), and, due to their tensorial nature, the Navier-Stokes equations are interpreted as a system of nonlinear PDEs.

In the rest of the thesis we make a wide use of the dimensionless equations, particularly when numerical simulations are required to provide qualitative

results. Hence, when needed, we will describe the non-dimensionalization process and the dimensionless quantities involved. For the Navier-Stokes equation, if U is a characteristic velocity and L is a characteristic length scale, then we define the Reynolds number as

$$Re = \frac{\rho U L}{\mu}. \tag{2.26}$$

Two different non-dimensionalization processes lead to two particular equations in fluid mechanics. On the one hand, non-dimensionalizing Eq. (2.21, without splitting the total stress $\boldsymbol{\sigma}$, leads to

$$Re\Big(\frac{\partial \vec{u}}{\partial t} + (\vec{u}\cdot\nabla)\vec{u}\Big) = \nabla\cdot\boldsymbol{\sigma}. \tag{2.27}$$

If, in Eq. (2.27), $Re \to 0$, the corresponding equation models the so-called *creeping flows*, which are considered insertialess.

On the other hand, if Eq. (2.25) is made non-dimensional, the following equation is retrieved:

$$\Big(\frac{\partial \vec{u}}{\partial t} + (\vec{u}\cdot\nabla)\vec{u}\Big) = -\nabla p + \frac{1}{Re}\triangle\vec{u}. \tag{2.28}$$

In this case, if $Re \to \infty$, we have the inviscid Euler equation.

A third possibility is the existence of a critical value for the Reynolds number which marks the boundary between laminar and turbulent flows. The investigation of these particular cases are outside the scope of this thesis. The literature on these topics is very broad; detailed analysis of creeping flows can be found for instance in Pnueli and Gutfinger [99] (chapter 9) as well as in the classic book by Landau and Lifshitz [64] (chapter 2). We refer to the same monographs regarding flows at high Re; precisely they are described and investigated in [99] (chapter 10 and 11) and [64] (chapter 2). Finally, the reader interested in turbulence will find once again the same books useful: [99] (chapter 12) and [64] (chapter 3).

We conclude this by section mentioning that, although there are quite a few problems for which an exact solution has been found (see for example

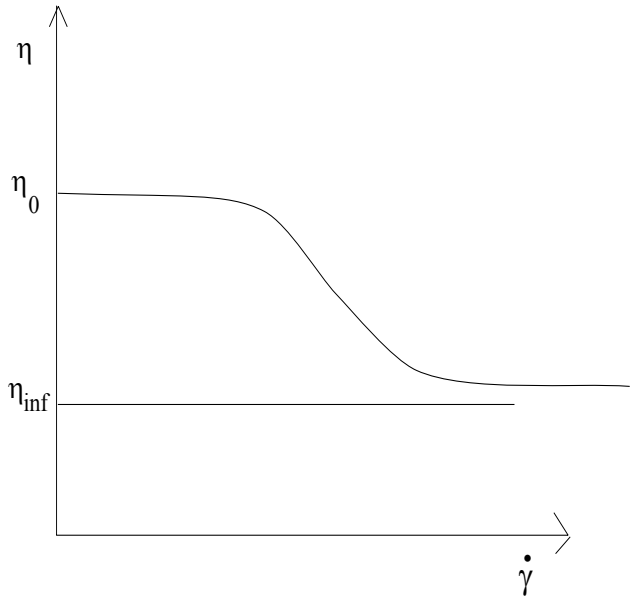

Figure 2.4: Shear viscosity versus shear rate.

[99] (chapters 5, 6), and [64] (chapter 2), a complete analytical solution of the three dimensional Navier-Stokes equations is one of the seven millennium problems and beyond the scope of this thesis!

2.4 Non-Newtonian fluids

Fluids not obeying the constitutive equation (2.24) are called non-Newtonian. Among these there are fluids exhibiting elastic properties, like stretching or elastic recovery; these will be investigated in Sections §2.6-§2.7.

The aim of the present section is to describe different types of fluids exhibiting nonlinear viscous effects. This could be expressed by a generalized constitutive equation in which the viscosity is a function of the rate of strain:

$$\boldsymbol{\tau} = 2\mu(\boldsymbol{d})\boldsymbol{d}. \tag{2.29}$$

Since equation (2.29) is a relation between the two tensors $\boldsymbol{\tau}$ and $\boldsymbol{d}$, then to preserve the rank of the equation, $\mu(\boldsymbol{d})$ has to be a scalar, namely a tensor of rank zero; but this is possible only if $\mu(\boldsymbol{d})$ is function of the invariants of

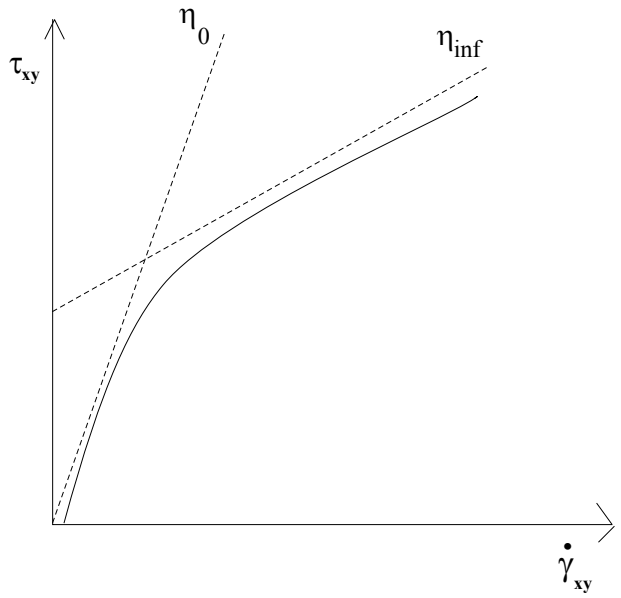

Figure 2.5: Shear stress versus shear rate.

$\boldsymbol{d}$

$$I_1 = tr(\boldsymbol{d}) \tag{2.30}$$

$$I_2 = \boldsymbol{d} : \boldsymbol{d} \tag{2.31}$$

$$I_3 = \det \boldsymbol{d}. \tag{2.32}$$

For incompressible fluids $I_1 = 0$, so the viscosity would be a function of I_2 and I_3. But we also note that for shear flows, or two-dimensional flows in general, I_3 also vanishes. This gives an explanation as to why generalized non-Newtonian fluids of this type are suitable for simple shear flows only. In this case the constitutive equation becomes

$$\boldsymbol{\tau} = 2\mu(\mid \boldsymbol{d} \mid)\boldsymbol{d}, \tag{2.33}$$

where $\mid \boldsymbol{d} \mid = \boldsymbol{d} : \boldsymbol{d}$ is called the generalized *shear rate*. Only the second invariant, the *norm* of the rate of strain tensor, will count. When (in extensional flows, for instance) elastic effects become relevant, and they are

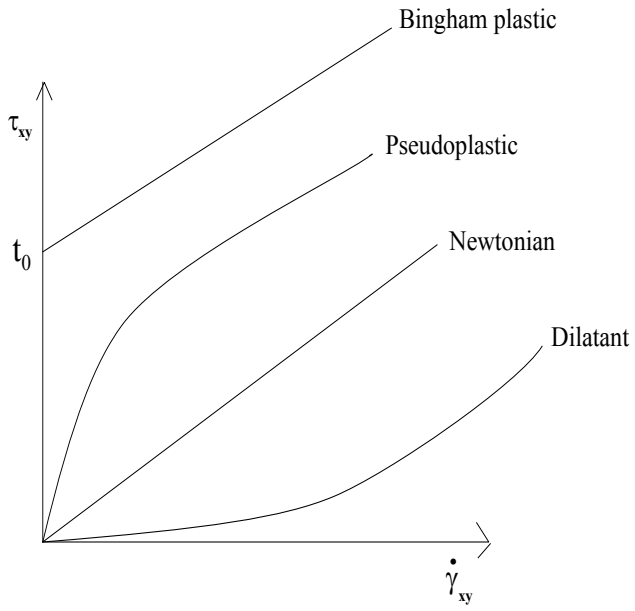

Figure 2.6: Shear stress vs shear rate for different model fluids.

mainly represented by the normal stress difference, then different constitutive relations are required.

A classification of nonlinear generalized Newtonian fluids relies on how the viscosity changes with the shear rate. In Figs. 2.4 and 2.5 the shear viscosity and the shear stress behaviour are depicted for a *shear-thinning* or *pseudo-plastic* fluid. The viscosity decreases until it reaches a plateau. This has been observed experimentally for most non-Newtonian fluids, although there are a few *shear-thickening* or *dilatant* fluids exhibiting the opposite feature.

The Bingham plastic is an example of what is known as *yielding* fluid. It does not flow below a certain threshold value of shear stress, above which is a Newtonian fluid. In Fig. 2.6 the different curves are summarized.

Finally, *thixotropic* and *rheopectic* fluids are examples of fluids in which the shear viscosity changes also with time, because at constant shear rate these fluids lose or gain structure, respectively; this leads to a decrease or

an increase of viscosity with time.

2.5 Viscoelastic fluids

The characteristic of viscoelastic fluids is that, if a stress is applied, some time is required for the fluid to completely return to its equilibrium configuration. Another way of explaining this is that the fluid experiences a partial elastic recovery a certain amount of time after a deformation occurs. These time intervals are called relaxation time and retardation time, respectively. They are two different two concepts and indeed two key quantities for understanding viscoelastic fluids.

We start our analysis by describing what happens when a sudden, or instantaneous, deformation is applied to a material. The following step function will represent this strain:

$$\theta = \begin{cases} 0, & t < 0 \\ \frac{\bar{\theta}}{2}, & t = 0 \\ \bar{\theta}, & t > 0. \end{cases} \tag{2.34}$$

For a Hookean elastic solid with Young's modulus G, the shear stress is proportional to the deformation, so the following equation will hold:

$$\tau_{xy} = G\bar{\theta}H(t). \tag{2.35}$$

On the other hand, for a Newtonian fluid with dynamic viscosity $\bar{\eta}$, the shear stress is proportional to the rate of strain:

$$\tau_{xy} = \bar{\eta}\bar{\theta}\dot{H}(t). \tag{2.36}$$

Since $\dot{H}(t) = \delta(t)$, the Dirac-delta function, and looking at Figs. 2.7 and 2.8, we can now understand the meaning of the first concept stated at the beginning of the section: the *relaxation time*. The relaxation time is zero for a Newtonian fluid, while it is infinite for a Hookean solid. The truth is that for all fluids in nature the relaxation time is a *finite* amount of time, i.e., nothing is *really* a Newtonian fluid or a Hookean solid. On the other hand, some materials are very accurately approximated by these models.

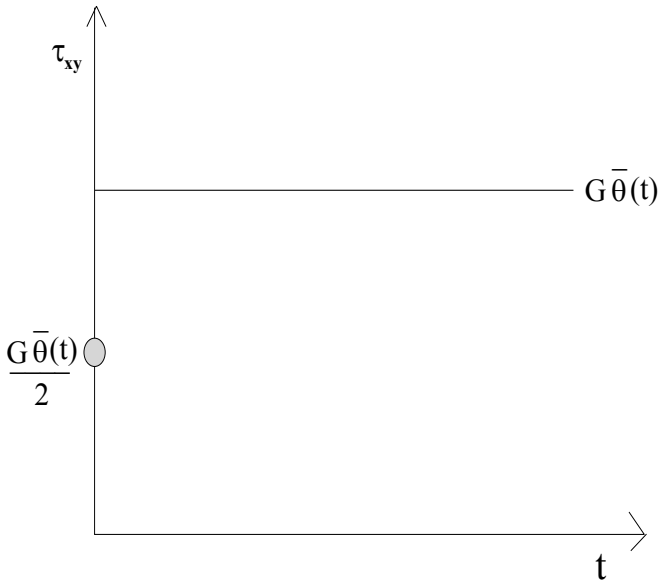

Figure 2.7: Shear stress never relaxes for a Hookean solid.

In the so called *Maxwell model*, Young's elastic modulus and Newtonian viscosity are combined in the following relation:

$$\frac{1}{G}\frac{d}{dt}\tau_{xy} + \frac{1}{\bar{\eta}}\tau_{xy} = \dot{\gamma}_{xy}. \tag{2.37}$$

In this model the time derivative of the shear stress also depends on the rate of strain through G. Integration leads to

$$\tau_{xy}(t) = \int_{\infty}^{t} \frac{\bar{\eta}}{\lambda_1} \exp\Big(- \Big(\frac{t-s}{\lambda_1}\Big)\Big)\dot{\gamma}_{xy}(s)\ ds, \tag{2.38}$$

which, integrated again by parts gives

$$\tau_{xy}(t) = \int_{\infty}^{t} \frac{\bar{\eta}}{\lambda_1^2} \exp\Big(- \Big(\frac{t-s}{\lambda_1}\Big)\Big)\gamma_{xy}(s)\ ds. \tag{2.39}$$

In (2.38) and (2.39), $\lambda_1 = \frac{\bar{\eta}}{G}$ is the relaxation time. Equation (2.39) tells us that the stress at a certain time depends on the whole strain history. At the same time, this dependence is modulated by the *memory function*

$$M(t-s) = \frac{\bar{\eta}}{\lambda_1^2} \exp\Big(- \frac{t-s}{\lambda_1}\Big), \tag{2.40}$$

so the further we move back in time, the less the strain contributes to the stress at the current time. Moreover, it can been seen that zero and infinite relaxation times in (2.40) recover the Newtonian and Hookean approximations, respectively.

A parameter which is used to measure the influence of the relaxation time whenever it is neither zero nor infinite is the *Deborah number*. It is the ratio between the relaxation time of the material and the time length of the observed phenomenon:

$$De = \frac{\lambda_1}{\bar{T}}. \tag{2.41}$$

The Deborah number is a dimensionless measure of the elasticity of a viscoelastic fluid and also explains why the same fluid has a different behaviour in different experiments: if the time of the experiment is small compared to the relaxation time, it means that the matter has had not enough time to exhibit relaxation and will respond as a solid. In the opposite case the fluid-like behaviour will be dominant due to the time available to the stress for a complete relaxation. This is the reason why when punching a bulk of a 9 to 1 mixture of corn starch and water your fist will bounce back, but when gently pouring it on a hand it will flow through the fingers.

As we mentioned at the beginning of the section, we can also apply a sudden stress of the type

$$\tau_{xy}(t) = \begin{cases} 0, & t < 0 \\ \bar{\tau}, & t \geq 0 \end{cases} \tag{2.42}$$

and observe the consequent deformation process following the *Kelvin* model

$$\tau_{xy}(t) = G\gamma_{xy} + \bar{\eta}\dot{\gamma}_{xy}, \tag{2.43}$$

where γ_{xy} and $\dot{\gamma}_{xy}$ are the deformation and the deformation rate, respectively. The Kelvin model simply combines linearly Hookean and Newtonian dependence. The solution of this equation is

$$\gamma_{xy}(t) = \frac{\bar{\tau}}{G}\Big(1 - \exp\Big(-\frac{t}{\lambda_2}\Big)\Big). \tag{2.44}$$

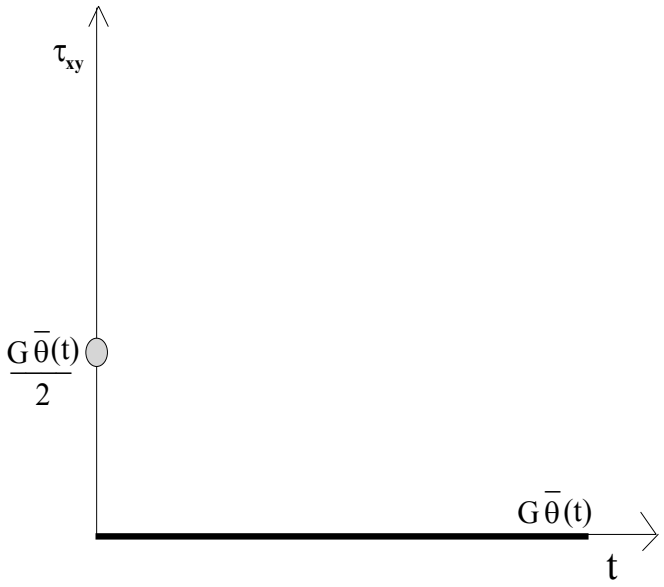

Figure 2.8: Shear stress instantaneously relaxes for a Newtonian fluid.

In this context $\lambda_2 = \frac{\bar{\eta}}{G}$ is the *retardation time*.

Apart from these time constants, which are zero for a purely viscous fluid, the other important features of viscoelastic fluids are the normal stress differences. In the shear flow of a Newtonian fluid the three normal components of the stress tensor, τ_{xx}, τ_{yy} and τ_{zz}, are the same. In fact, are simply a third of the pressure field, there being no deviatoric normal stress. For polymeric liquids, this is not true. A first and a second normal stress difference in the polymeric extra-stress $\boldsymbol{\tau}$, where $\boldsymbol{T} = 2\mu\boldsymbol{d} + \boldsymbol{\tau}$, are reported in the experiment, $N_1 = \tau_{yy} - \tau_{xx}$ and $N_2 = \tau_{zz} - \tau_{yy}$, respectively, with $N_2 \simeq 0.1 N_1$ in modulus. Such features are related to the anisotropic response of a polymeric liquid to an applied strain. In such materials, which are able to oppose a certain amount of elastic resistance to a strain, the stress tensor deforms with the velocity fields, therefore showing a non isotropic response. In viscoelastic models a first normal stress is always predicted, while N_2 usually requires a quadratic term in the stress tensor in the constitutive equation. For example, the XPP model, the Giesekus model and some K-BKZ models

incorporate such terms and predict N_2, while other models, such as Oldroyd-B and the Pom-Pom model do not.

In the remaining two sections of the chapter, two very important types of industrial viscoelastic fluids will be analyzed: disperse and concentrated polymer mixtures.

2.6 Modelling disperse polymer solutions

Disperse polymer solutions are mixtures in which the molecules are supposed to be far enough from each other such that only the interactions between them and the surrounding fluid is taken into account in the modelling process. In some way, this allows a microscopic approach to the modelling being discarded, because a global description of both the elastic contribution from the particles and the viscous contribution from the solvent is possible. Nonetheless for the Oldroyd-B model, an equivalence between macroscopic and microscopic approach will be highlighted.

2.6.1 The UCM and Oldroyd-B models

The Upper Convective Maxwell model is the simplest description of a viscoelastic fluid. Mathematically, is the constitutive tensorial equation corresponding to the Maxwell model (2.37), described in the previous section, in which viscosity and elasticity are combined in series:

$$\boldsymbol{T} + \lambda_1 \overset{\triangledown}{\boldsymbol{T}} = 2\eta \boldsymbol{d}, \tag{2.45}$$

with $\overset{\triangledown}{\boldsymbol{T}}$ defined as the upper-convective derivative as follows:

$$\overset{\triangledown}{\boldsymbol{T}} = \frac{D\boldsymbol{T}}{Dt} - (\nabla \vec{u})\boldsymbol{T} - \boldsymbol{T}(\nabla \vec{u})^T. \tag{2.46}$$

The replacement of the time derivative in (2.37) by the upper-convective derivative is required because the non- affine deformation of the fluid molecules has to be taken into account. What happens is that the material derivative $\frac{D}{Dt}$ in Eq. (2.46) accounts for the dependence of the stress on the entire strain history. Moreover, the last two terms in (2.46) are responsible for

the deformation to which the stress tensor is subject simply because of the effect of the rate of strain tensor. For these reasons in viscoelastic flows, the upper-convective derivative replaces the material derivative.

The Oldroyd-B model [90] is a combination of the Maxwell model (2.37) and the Kelvin model (2.43);

$$\boldsymbol{T} + \lambda_1 \overset{\triangledown}{\boldsymbol{T}} = 2\eta(\boldsymbol{d} + \lambda_2 \overset{\triangledown}{\boldsymbol{d}}). \tag{2.47}$$

Upper-convective derivatives of both stress and rate of strain are considered. Physically, a Newtonian viscosity is also considered in the Oldroyd-B model. We can then split the extra-stress tensor into its polymeric part $\boldsymbol{\tau}$, namely the one due to the elasticity of the dumbbells, and its viscous part $2\eta_s \boldsymbol{d}$, obeying Newton's law of viscosity. The total viscosity is then split into η_p, the polymeric viscosity, and η_s, the pure viscosity of the Newtonian solvent. By means of this, the solvent contribution of the extra-stress, obeying Newton's law of viscosity, can be inserted into the momentum equation in the same fashion as for the Navier-Stokes equations. This is not possible for the polymeric part. The full system will then read

$$\begin{aligned} \nabla \cdot \vec{u} &= 0, & (2.48)\\ \rho\Big(\frac{\partial \vec{u}}{\partial t} + \vec{u} \cdot \nabla \vec{u}\Big) &= -\nabla p + \nabla \cdot \boldsymbol{\tau} + \eta_s \triangle \vec{u}, & (2.49)\\ \boldsymbol{\tau}_p + \lambda_1 \overset{\triangledown}{\boldsymbol{\tau}} &= 2\eta_p \boldsymbol{d}, & (2.50) \end{aligned}$$

or, in its dimensionless form,

$$\begin{aligned} \nabla \cdot \vec{u} &= 0, & (2.51)\\ Re\Big(\frac{\partial \vec{u}}{\partial t} + \vec{u} \cdot \nabla \vec{u}\Big) &= -\nabla p + \nabla \cdot \boldsymbol{\tau} + \beta \triangle \vec{u}, & (2.52)\\ \tau + Wi \overset{\triangledown}{\boldsymbol{\tau}} &= 2(1-\beta)\boldsymbol{d}. & (2.53) \end{aligned}$$

In Eq. (2.52)-(2.53) the following dimensionless parameters have been used:

$$\beta = \frac{\lambda_2}{\lambda_1} = \frac{\eta_s}{\eta_s + \eta_p} = \frac{\eta_s}{\eta_{total}}, \tag{2.54}$$

is the ***viscosity ratio parameter***, and

$$Wi = \frac{\lambda_1 U}{L} \tag{2.55}$$

is the ***Weissenberg number*** [1], a crucial parameter in all rheological problems. Sometimes it is assimilated to the Deborah number, if the timescale of the experiment can be deduced from the ratio between the characteristic length and characteristic velocity. The Weissenberg number is another way of measuring the elasticity of a material. If in the Oldroyd-B model the Kelvin approach is discarded, namely the retardation time $\lambda_2 = 0$ (or $\beta = 0$) we recover the UCM model, as we expect.

The Oldroyd-B models presents some advantages: it is the only macroscopic model with a perfectly equivalent microscopic representation in which the polymeric part is represented by Hookean elastic dumbbells in which the beads are connected by a vector $\boldsymbol{Q}$ and their interaction with the solvent is described by Brownian forces through a probability density function $\psi(\boldsymbol{Q}, t)$. A full description based on the Fokker-Planck equation can be found in the book by Owens and Phillips [94] (chapter 2). Also, analytical solutions for channel flow have been derived by Waters and King [136].

On the other hand, the application of the Oldroyd-B model to real industrial problems is very limited. One reason is that for shear flow, despite predicting a non-zero first normal stress difference, the model leads to a constant shear viscosity. However, the main drawback of the Oldroyd-B model is its inability to describe accurately extensional behaviour.

We already mentioned that elastic effects in a fluid manifest mostly in extensional flows. An extensional flow is described, for example, by a velocity field of the form

$$\vec{u} = \left(\epsilon x, -\frac{\epsilon}{2} y, -\frac{\epsilon}{2} z\right), \tag{2.56}$$

[1] Throughout the thesis Wi denotes the Weissenberg number while We the Weber number defined in Chapter 4.

where ϵ is the extensional rate. If we apply the Oldroyd-B constitutive equation and compute the first normal stress difference, we find

$$\tau_{xx} - \tau_{yy} = \bar{\eta}\epsilon\Big(\frac{2(1-2\lambda_2\epsilon)}{1-2\lambda_1\epsilon} + \frac{1+\lambda_2\epsilon}{1+\lambda_1\epsilon}\Big). \tag{2.57}$$

Looking at the definition of extensional viscosity, we realize that a singularity arises for $\epsilon = 1/(2\lambda_1)$. This means that the Oldroyd- model predicts the unphysical phenomenon of infinite extensibility of the fluid, which is caused by a possible infinite stretch of the Hookean springs connecting the dumbbells modelling the molecules. This problem, which limits the real applicability of the Oldroyd-B model to low rate flows, is circumvented by Finitely Extensible Nonlinear Elastic (FENE) models.

2.6.2 The FENE models

The models described in this section, based on the hypothesis of finite extensibility of the dumbbells spring, have been proposed by Warner (original FENE) [135], Peterlin (FENE-P) [97] and Chilcott and Rallison (FENE-CR) [24]. For a detailed investigation of different features, together with the analysis of other types of dumbbells, the monograph by Bird et al. [12] is exhaustive. The aim of this section is to highlight the different versions of the model and their characteristics.

In the microscopic description of the Oldroyd-B model, the molecules are depicted as beads connected by a Hookean spring; so the elastic force is proportional to the extension. The stress tensor is then related to this force by the Kramers relation

$$\boldsymbol{T} = -nkT\boldsymbol{I} + \mu_s\dot{\gamma} + n\langle\boldsymbol{QF}\rangle, \tag{2.58}$$

where n represents the density of the dumbbells, T is the temperature, k is a constant and $\boldsymbol{Q}$ is again the vector connecting the beads. Finally, the notation $\langle\cdot\rangle$ is the ensemble average defined as

$$\langle f(\boldsymbol{Q})\rangle = \int_{R^3} f(\boldsymbol{Q})\psi(\boldsymbol{Q},t)\, d\boldsymbol{Q}. \tag{2.59}$$

The Hookean force $\boldsymbol{F} = h\boldsymbol{Q}$ is only one of the possible choices for $\boldsymbol{F}$, and as we have seen leads to unphysical consequences. A first alternative was proposed by Warner [135]; the choice of the elastic spring force

$$\boldsymbol{F} = \frac{h\boldsymbol{Q}}{1 - (Q^2/Q_0^2)} \tag{2.60}$$

leads to the FENE model. In (2.60) $Q = tr(\boldsymbol{QQ})$ and Q_0 is a constant which represents the limiting value for the extension of the spring.

The FENE-P model is an approximation to the FENE model with force law defined by the closure law proposed by Peterlin:

$$\boldsymbol{F} = \frac{h\boldsymbol{Q}}{1 - \langle Q^2/Q_0^2\rangle}. \tag{2.61}$$

This model is shear-thinning and the extensional viscosity μ_ϵ exhibits continuous dependence on the extensional rate ϵ in extensional flows (see Bird et al. [12] for details). Clearly in both FENE and FENE-P models when $Q_0 \to \infty$ the Oldroyd-B is recovered.

To describe the last of the three FENE models, we first write down the Giesekus expression which relates the stress tensor to the vector $\boldsymbol{Q}$:

$$\boldsymbol{T} = \eta_s\dot{\gamma}\frac{n}{2(1/\zeta_1 + 1/\zeta_2)}\langle\overset{\triangledown}{\boldsymbol{QQ}}\rangle, \tag{2.62}$$

where $\zeta_i, i = 1, 2$ are the friction coefficients arising from the Stokes' drag law applied to the beads. Combining (2.58), (2.61) and (2.62) we obtain the relation

$$\frac{kT}{h}\langle\overset{\triangledown}{\boldsymbol{QQ}}\rangle = \frac{1}{\lambda_1}(\boldsymbol{I} - f(Q)\langle\overset{\triangledown}{\boldsymbol{QQ}}\rangle), \tag{2.63}$$

where $f(Q)$ is the scalar function

$$f(Q) = \frac{1}{1 - \langle Q^2/Q_0^2\rangle}.$$

The so-called FENE-CR model empirically replaces the term

$$(\boldsymbol{I} - f(Q)\langle\overset{\triangledown}{\boldsymbol{QQ}}\rangle)$$

in (2.63) by $f(Q)(\boldsymbol{I} - \langle \overset{\nabla}{\boldsymbol{QQ}} \rangle)$. This model is similar to the Oldroyd-B in predicting constant shear viscosity and a quadratic first normal stress difference, but also ensures that the extensional viscosity is bounded and continuous extensibility as the other FENE models.

We conclude by remarking that the FENE models are naturally more useful in investigating extensional flows rather than shear flows, even if the FENE-P presents a shear-thinning characteristic which makes it suitable to describe polymer mixtures in shear flow. Comparisons of these three different models in transient elongational flow has been performed by Keunings [63].

2.7 Modeling concentrated polymer melts

In the models describing disperse polymer solutions, the physics of a single molecule is not affected by surrounding ones. As we have seen the assumption is that these molecules are far enough from each other such that only the interaction between them and the solvent is relevant. When the solutions are concentrated, as is the case of polymer melts, this assumption is not valid anymore. In order to investigate polymer melts it is essential to represent in a proper way the entanglement between molecules.

In this section we will describe the most popular models for polymer melts. The PTT model [98] was proposed by Phan-Thien and Tanner in 1977, and it looks at the polymer molecules and at their interaction as a network. Strands are linked through rigid junctions, and the idea is that the rate of change of a probability distribution of strands is balanced by the difference between the rate of creation and destruction of junctions. The two versions of this model, linear and exponential, will be described in §2.7.1.

The other models we will describe are based instead on the so called "tube" molecule. The influence of surrounding molecules manifests itself by means of a constrained lateral displacement. Thus this displacement is limited to a maximum value which is identified with the diameter of an imaginary tube

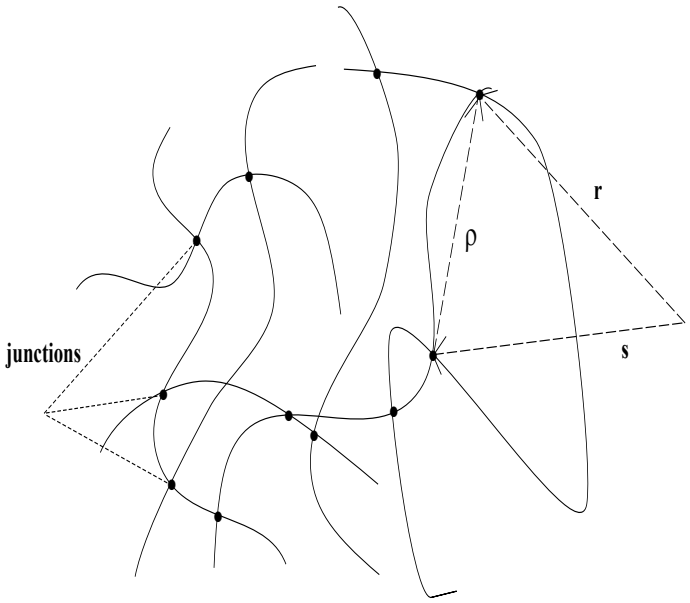

Figure 2.9: An example of a network of polymers.

along whose axis the molecules move. The original tube model was proposed by Doi and Edwards in 1978 (see the monograph [33] for instance), and only included the mechanism of reptation. Further developments came twenty years after with the Pom-Pom model of McLeish and Larson [79] and the XPP model of Verbeeten et al. [132], who, with the introduction of stretch of the backbone to support the appended arms, aimed to reproduce the rheology of branched polymers. A further step was then represented by the mechanism of convective constraint release proposed by Marrucci [75] and further developed by Marrucci and Ianniruberto [75, 76]. Such a mechanism has been included, among the others, in the full SCCR model by Graham et al. [46], whose a simplified version is represented by the Rolie-Poly model by Likhtman and Graham [72]. Differently from the XPP model, the full SCCR aims to reproduce the behaviour of entangled, linear polymers over a wide range of flow regimes.

2.7.1 The PTT models

The idea that forms the basis of the PTT model is to represent polymer molecules as a network. They cross each other forming junctions, and the segments between two junctions are the strands. The junctions are identified by position vectors, and the strands by an end to end vector, say $\vec{Q}$ (see fig. 2.9). Assuming that slip is the cause of dynamics of the strands, then an evolution equation in $\vec{Q}$ is written, which at first order reads

$$\frac{\partial \vec{Q}}{\partial t} = \boldsymbol{L}\vec{Q} + \frac{\partial \alpha}{\partial r}\vec{Q}. \tag{2.64}$$

The tensor $\frac{\partial \alpha}{\partial r}$ is the slip tensor, whose representation will be the key difference between the different models presented in this section, as we will see in §2.7.2 and §2.7.3. In the PTT model the slip tensor is assumed to be a function of the rate of deformation $\boldsymbol{d}$ and $\vec{Q}$. Equation (2.64) then becomes

$$\frac{\partial \vec{Q}}{\partial t} = \boldsymbol{L}\vec{Q} - C_1\vec{Q} - C_2\boldsymbol{D}\vec{Q}. \tag{2.65}$$

Let f be the probability distribution of junctions. As we already mentioned in the PTT model the total rate of change of $\vec{f}$, which is a function of time, space and the strand end-to-end vector $\vec{Q}$, is balanced in the following conservation law:

$$\frac{\partial \vec{f}}{\partial t} + \vec{v}\cdot\frac{\partial \vec{f}}{\partial r} + (\boldsymbol{L}\vec{Q} - C_1\vec{Q} - C_2\boldsymbol{d}\vec{Q})\cdot\frac{\partial \vec{f}}{\partial \vec{Q}} = g(\vec{Q}) - h(\vec{Q})\vec{f}, \tag{2.66}$$

where $g(\vec{Q})$ and $h(\vec{Q})$ represent the rate of creation and the rate of destruction of the junctions, respectively. Multiplying both sides by $\vec{Q}$ and averaging over configuration space, the following constitutive equation is derived, where E is a constant:

$$\lambda_0 \overset{\diamond}{\tau} + (1 + E\, tr(\boldsymbol{\tau}))\boldsymbol{\tau} = 2\frac{G_0\lambda_0}{1 - C_2}\Big(\boldsymbol{d} - \frac{1}{2}C_2(\boldsymbol{d} + \boldsymbol{d}^T)\Big). \tag{2.67}$$

We refer to the paper of Phan-Tien and Tanner [98] for the details and the derivation of equation (2.67). We remark here that a different type of derivative $\overset{\diamond}{(\cdot)}$, the so-called *GordonShowalter convected derivative*, is involved because the choice of the slip tensor described earlier leads to a deformation

factor which is not the usual velocity gradient but the so-called *effective velocity gradient* $\nabla\vec{u} - C_2\boldsymbol{d}$. Then the following relation holds:

$$\overset{\diamond}{\tau}=\overset{\triangledown}{\tau} + C_2(\boldsymbol{d}\tau + \tau\boldsymbol{d}^T).$$

This is a consequence of assuming that the end-to-end vector $\vec{Q}$ obeys the non-affine transformation (2.65).

The PTT model predicts shear thinning and bounded extensional viscosity, addressing some of the limitations of the Oldroyd-B. It also reproduces fairly well the stress overshoots at high strain rates in elongational flow, justifying the credit gained in simulating flows of polymer melts. However, the presence of the GordonShowalter convected derivative, which occurs when $C_2 \neq 0$ and is required if a non-zero second normal stress difference has to be predicted, causes unstable behaviour of the model in transient flows [65].

We conclude by mentioning the exponential version of the PTT, whose modified equation reads

$$\lambda_0 \overset{\diamond}{\tau} + (-1 + \exp(Etr(\boldsymbol{\tau})))\boldsymbol{\tau} = 2\frac{G_0\lambda_0}{1 - C_2}\Big(\boldsymbol{d} - \frac{1}{2}C_2(\boldsymbol{d} + \boldsymbol{d}^T)\Big).$$

2.7.2 The tube model

The tube model developed by Doi and Edwards [33] translates the interactions between molecules that are close to each other as topological constraints. The presence of other chains surrounding a test molecule will confine the allowed configurations within a tube of a certain diameter, a. The test molecule is represented as a chain of entangled segments, with end points connecting single molecules with a molecular weight over a certain threshold. When dense polymer melts are described, then this constrained perpendicular displacement is discarded, because the predominant effect is the reptation along the axis of the tube, and the molecule is depicted as an end-to-end segment.

The molecule is then allowed to slide, or *reptate*, leaving the original tube for another one. In Fig. 2.10 such a tube is depicted, and AB is called a

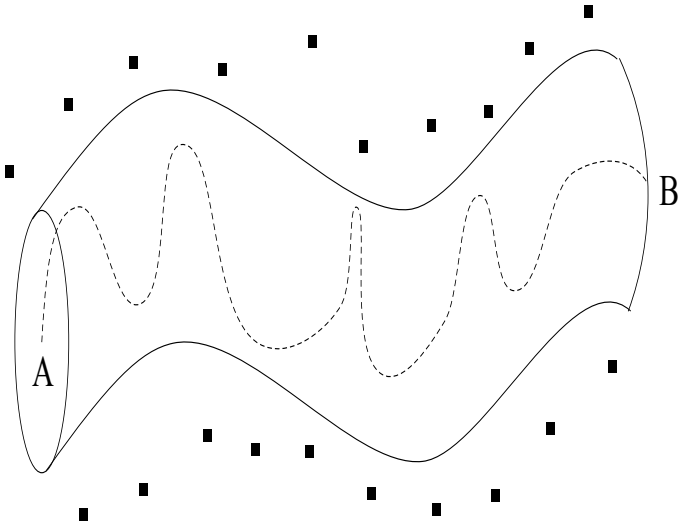

Figure 2.10: The Doi-Edwards tube model.

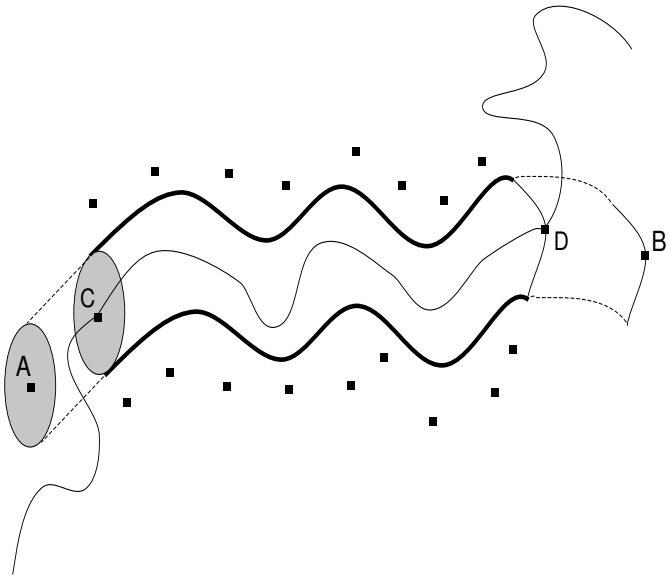

Figure 2.11: A part of the primitive chain leaves the tube.

primitive chain, whose length is L. This chain is allowed to move to the left or to the right, so the ends A and B will slide. To model this reptation Doi and Edwards use a diffusion equation for the function $\vartheta(\xi, t; s)$, namely the probability that the primitive chain slides within the tube of a curvilinear segment ξ without A and B reaching C and D, s being the length of the arc CD. When this happens, the dotted part of the tube disappears, as shown in Fig 2.11. This dynamics is translated into the the following initial-boundary problem:

$$\frac{\partial \vartheta}{\partial t} = D_c \frac{\partial^2 \vartheta}{\partial \xi^2}, \tag{2.68}$$

$$\vartheta(\xi, 0; s) = \delta(s), \tag{2.69}$$

$$\vartheta(\xi, t; s) = 0 \qquad for \qquad \xi = s \; and \; \xi = s - L. \tag{2.70}$$

In Eq. (2.68) the right-hand side includes only a diffusive term, which is responsible for the reptation of the chain. If this problem is solved averaged in space, the its solution is independent of L and reads

$$\psi(t) = \frac{1}{L} \int_0^L \int_s^{s-L} \vartheta(\xi, t; s) d\xi \; ds = \sum_{p \; odd} \frac{8}{p^2 \pi^2} \exp(-p^2 t / T_d). \tag{2.71}$$

In Eq. (2.71)

$$T_d = \frac{\zeta N^3 b^4}{\pi^2 k_B T a^2} \tag{2.72}$$

is the time required for the primitive chain to disentangle from the original tube, namely for the segments AC and BD to disappear. In (2.72), ζ is the average of the friction coefficients due to the Brownian forces, b is the average length of the entanglements, k_B is the Boltzmann constant and T is the absolute temperature. If we compare it with the Rouse relaxation time

$$T_R = \frac{\zeta N^2 b^2}{3\pi^2 k_B T}$$

which comes from the Rouse chain in which there are no displacement constraints, a stronger dependence on the number of entangled segments N is evident in the tube model. This is clearly due to the fact that in the Doi-Edwards tube, due to the presence of surrounding chains, not all possible

configurations are allowed for the chain.

The key of the tube model is all in the function $\psi(t)$, which microscopically represents the dynamics of the reptation with respect to the displacement constraints. Thus, when viscoelasticity is considered, the reptation dynamics will be responsible for the change of conformation of the primitive path and for the stress calculation from such conformations. The stress is not directly linked to the rate of deformation but to the orientation tensor $\boldsymbol{Q}$ as follows:

$$\boldsymbol{\sigma} = G\boldsymbol{Q}(\boldsymbol{E})\psi(t). \tag{2.73}$$

In (2.73), $\boldsymbol{E}$ is the deformation gradient and G is proportional to the Boltzmann constant and the temperature T, and inversely proportional to a^2. The tube model is the key for understanding the models described in the rest of the chapter, where the level of sophistication has been increasing with the introduction of additional mechanisms such as constraint release, chain stretch and contour fluctuations. We refer to Doi and Edwards [33] for all the details.

2.7.3 Modelling branched polymers: the PP and the XPP models

Following the tube idea, McLeish and Larson [79] developed the Pom-Pom model in 1998. The pom-pom molecule, shown in Fig. 2.12, is a branched polymer whose branches are attached to the ends of a primitive tube chain like the one proposed by Doi and Edwards [33]. The primitive chain is the *backbone* of the pom-pom molecule.

This model describes very accurately the two main features of low density polyethylenes (LDPE), whose irregular branches give rise to high levels of shear thinning and strain hardening. Nonetheless, some drawbacks are present in the Pom-Pom models, which will be highlighted later on; these drawbacks have been the reason for the pursuit of improvements, which are mainly represented by the Blackwell modification and the XPP model.

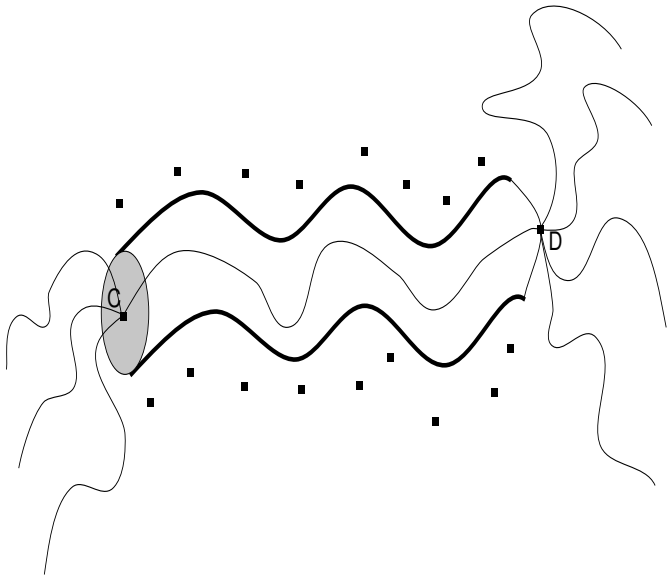

Figure 2.12: The pom-pom molecule.

In order to deal with the discontinuities in the gradient of the extensional viscosity, Blackwell [14] proposed a modification to the original Pom-Pom model. This change allows for the arms to start reptating themselves and thus to withdraw into the tube even if the stretch of the backbone is not at its maximum value, namely, even if $\lambda < q$. A smoother approach to the limit value $\lambda = q$ is achieved by smoothing the arm stretch relaxation time from T_s to $T_s \exp(-\nu(\lambda - 1))$, thus leading to the removal of the discontinuous peaks in the gradient of the extensional viscosity.

The mathematical modelling of the pom-pom molecule deals with three issues: the orientation of the tube segments in the deforming melts; the dynamics of stretch of the backbone; the dynamics of the arms of the molecule. Evolution equations are derived from the Doi-Edwards tube model. One equation is needed for the stretch $\lambda(t)$, and a similar equation follows the evolution of the arms $a_i, i = 1, ..., q$. On the other hand, the total stress $\boldsymbol{\sigma}$ is not directly related to the rate of strain but to the deformation gradient through the orientation tensor $\boldsymbol{S}(t)$, whose evolution requires another

equation. These equations are summarized here:

1) ***Evolution equation for the orientation tensor***:

$$\boldsymbol{S}(t) = \int_{-\infty}^{t} \frac{dt'}{T_b(t')} \exp\Big(-\int_{t}^{t'} \frac{dt''}{T_b(t'')}\Big) \frac{1}{\langle \mid \boldsymbol{E}(t,t') \cdot \vec{u} \mid \rangle} \langle \frac{\boldsymbol{E}(t,t') \cdot \vec{u} \boldsymbol{E}(t,t') \cdot \vec{u}}{\mid \boldsymbol{E}(t,t') \cdot \vec{u} \mid} \rangle. \tag{2.74}$$

2) ***Evolution equation for the backbone stretch***:

$$\frac{\partial \lambda}{\partial t} = \lambda(\boldsymbol{K} : \boldsymbol{S}) - \frac{1}{T_s}(\lambda - 1) \qquad for \qquad \lambda < q \tag{2.75}$$

3) ***Evolution equation for the motion of the arms***:

$$\frac{\partial s_c}{\partial t} = (q\frac{s_b}{2} + s_c)(\boldsymbol{K} : \boldsymbol{S}) - \frac{1}{2T_a(x_c)} \qquad for \qquad \lambda = q. \tag{2.76}$$

4) ***Derivation of the stress tensor***:

$$\boldsymbol{\sigma} = C\frac{s_b}{2qs_a + s_b}\Big(\frac{s_b}{2qs_a + s_b}\lambda^2(t) + \frac{2qs_c(t)}{2qs_a + s_b}\Big)\boldsymbol{S}(t). \tag{2.77}$$

In the above equations, $\boldsymbol{K}$ is the rate of deformation tensor, while $\boldsymbol{E}$ is the deformation gradient; $\vec{u}$ is the orientation; the quantities s_a and s_b are the molecular weights of the arms and the backbone, respectively, scaled by the molecular weight of the entanglement.

The part of the arms withdrawn is $s_c(t)$, and we remark that in the pom-pom model this can happen only if the backbone stretch is at its maximum value, namely q. This means that the maximum stress the backbone can support is the stress caused by the arms. The relaxation times of backbone orientation, arms and backbone stretch are T_b, T_a and T_s respectively. The constant C is proportional to the relaxation modulus plateau. The evolution equations (2.74) -(2.76) are uncoupled and are solved to then calculate the stress through (2.77).

There is general agreement on the fact that the pom-pom model represents a turning point in viscoelastic modelling, mainly because the inclusion of the mechanism of chain stretch, by means of attaching arms to the tube backbone, gives a correct qualitative response in both shear and extensional viscoelasticity of low density polyethylene melts (see Inkson et al. [57] and

Bishko et al. [13], for instance). On the other hand the model presents three drawbacks: *first*, the already mentioned discontinuities which occur in the gradient of the viscosity in the steady state extensional flow; *second*, at high strain rates the evolution equation (2.74) for the orientation stress is unbounded; *finally*, a zero second normal stress difference is predicted. The **eXtended Pom Pom (XPP)** was introduced in 2001 by Verbeeten et al. [132] to circumvent these problems.

First, the Blackwell modification [14] is retained in the XPP model to avoid overshoots in the velocity gradient. Secondly, a different approach in dealing with the slip along the backbone is instead the reason behind the bound for the orientation tensor. Doi and Edwards [33] adopted a *microscopic* approach to describe the slip of the entangled segments of the backbone; the slip was derived by solving a Fokker-Planck type diffusion equation for ψ. Here ψ represents the probability that a segment of the primitive chain, and therefore of the tube, disappears as consequence of the reptation. As described in §2.7.2 the stress tensor, as well as the relaxation modulus, were then derived from the solution of this equation.

In the XPP model the slip tensor is instead a function of the averaged *macroscopic* stress tensor, which is quadratic in Λ, namely the stretch. This direct correlation between the slip tensor (and then the orientation tensor) and the stretch has two consequences. First, it allows for the XPP model to have a constitutive equation in the classical sense, namely, a stress-rate of strain relation. Moreover, the orientation phenomenon is limited by the stretch effects also being bounded. To better understand this process we write the set of equations for the XPP model:

1) ***Viscoelastic stress***:

$$\overset{\triangledown}{\boldsymbol{\tau}} + \lambda(\boldsymbol{\tau})^{-1}\boldsymbol{\tau} = 2G_0\boldsymbol{D} \tag{2.78}$$

2) ***Relaxation time tensor***:

$$\lambda(\boldsymbol{\tau})^{-1} = \frac{1}{\lambda_{0b}}\Big(\frac{\alpha}{G_0}\boldsymbol{\tau} + f(\boldsymbol{\tau})^{-1}\boldsymbol{I} + G_0[f(\boldsymbol{\tau})^{-1} - 1]\boldsymbol{\tau}^{-1}\Big) \tag{2.79}$$

3) ***Extra function***:

$$\frac{1}{\lambda_{0b}} f(\boldsymbol{\tau})^{-1} = \frac{2}{\lambda_s}\Big(1 - \frac{1}{\Lambda}\Big) + \frac{1}{\lambda_{0b}\Lambda^2}(1 - \frac{\alpha \boldsymbol{I}_{\boldsymbol{\tau}\boldsymbol{\tau}}}{3G_0^2}) \tag{2.80}$$

4) ***Backbone stretch and stretch relaxation time***:

$$\Lambda = \sqrt{1 + \frac{\boldsymbol{I}_{\boldsymbol{\tau}}}{3G_0}}, \qquad \lambda_s = \lambda_{0,s} \exp(-\nu(\Lambda - 1)), \qquad \nu = 2/q. \tag{2.81}$$

In Eqs. (2.78)-(2.81), G_0 is the zero-shear modulus, α is the anisotropy parameter, $\lambda_{0,b}$ is the orientation relaxation time of the backbone, $\lambda_{0,s}$ is the initial stretch relaxation time, q is the number of arms, Λ is the backbone stretch. We also define here the ratio $r = \frac{\lambda_{0,b}}{\lambda_{0,s}}$, which will be widely used throughout the thesis. If we now have a look at the two terms on the right-hand side of the extra function, we realize that the first vanishes when $\Lambda = 1$, namely when the backbone is subject to no stretch. On the other hand, the second vanishes when the strain rate is dominant. This has the following meaning: the effects of the backbone tube orientation are dominant in the flow process at low strains (when no stress coming from the arms has to be supported, therefore the backbone is not strecthed); on the other hand at high strain rates (when unbounded orientation was found in the pom-pom model), the orientation process is totally dominated by the stretch, circumventing the problem of unbounded orientation tensor. In this case the second term in the right-hand side. of (2.80) vanishes. This observation connects well to the discussion we raise in Chapter 6 and 7, where the effect of the flow rate on the orientation and stretch relaxation times is investigated through the analysis of the extrusion process.

The second normal stress difference, which is clearly observed in experiments for different types of polyethylene melts, is also lacking in the pom-pom model. The introduction of the quadratic term $\boldsymbol{I}_{\boldsymbol{\tau}\boldsymbol{\tau}}$ in (2.80) appears to remedy this.

Finally, we remark that another difference from the pom-pom is clear by looking at equation (2.81). The stretch is not calculated anymore through its evolution equation, but it is updated from the stress. An open issue in

the XPP investigation is the physical meaning of some imaginary values for Λ which sometimes arise in the numerical simulations using this formula.

2.7.4 Fine modelling of entangled linear polymers: inclusion of constraint release, interchain pressure effects and stretch

The introduction of the Pom-Pom molecule and the consequent PP and XPP models certainly represent a step forward in the modelling of branched polymers. However, in the past decade a remarkable effort has been made to tune more and more finely models based on the Doi-Edwards theory for linear, entangled chains. We summarize here the most important steps in this direction and the developments over the past few years. Since these models are not the main subject of this thesis, we will not focus on the very mathematical details, for which we refer to the relevant papers. Instead, this section is intended to underline the direction towards which theoretical modelling is heading nowadays, and the different mechanisms thought to contribute to different aspects of the physics of polymers.

A great push in this direction was represented by the experimental work carried out in Lyngby by Bach, Nielsen, Rasmussen and other collaborators under the coordination of Hassager [3, 4, 87, 88, 100]. Six years ago Bach et al. [3] reported experimental data for the highly nonlinear regime present in an extensional rheometer. The two polystyrene melts that were analyzed showed a monotonic decreasing steady-state extensional viscosity up to extensional rates of the order of $\dot{\varepsilon} \approx 10^3 \frac{1}{\tau_d}$, where τ_d is the relaxation time associated with the reptation mechanism. Such a relaxation time predicts quite successfully the departure from the Newtonian value $Tr = 3$ (Tr is the Trouton ratio defined in Eq. (1.3)), but is representative exclusively of the mechanism of the reptation, namely, the only mechanism included in the original model from Doi and Edwards described earlier. Therefore, when the flow rate scales at values well beyond τ_d, different relaxation processes have to be taken into account, together with different relaxation times. In fact, the main shortcoming from the Doi-Edwards model is arguably the prediction of a minimum in the steady extensional viscosity for values of

extensional rates just above $1/\tau_d$, more precisely around $1/\tau_R$, where τ_R is the Rouse time of the chain. The physical reason behind this is related to the instant chain retraction in the Doi-Edwards model when $\dot{\varepsilon} > \tau_R$. In other words, the absence of a stretch contribution in the Doi-Edwards model prevents it from being reliable when highly nonlinear regimes occur.

The second mechanism which has been proposed is related to a dynamic change of configuration for the chain surrounding the tube. Precisely, due to flow, the entanglements between the chains are more readily untied, therefore dynamically releasing some of the constraints. Constraint release might be produced by diffusion or convection. The former case, suggested by Graessley [45], is in a way related to the reptation of the chain. Therefore, at least in principle, a mechanism already accounted for in the tube theory. On the other hand, the latter, introduced by Marrucci [75], was absent. The Convective Constraint Release (CCR) was introduced as a mechanism that came into play in the highly nonlinear regime, whereas it should be negligible in the other cases. In particular, it arose from the observation that experimental data showed a substantial difference in the measures of the extensional viscosity between the uniaxial and biaxial elongations. In the former case, a strain hardening behaviour occurs, while something very similar to a shear-thinning response characterizes the biaxial experiment.

Marrucci and Ianniruberto [76] were also among the people considering the experimental data from Bach et al. [3] a sort of crisis of the standard model. They proposed as a remedy a third mechanism called interchain pressure effect. This concept states that the diameter of the tube in which the chain lives evolves in time due to a pressure exerted towards its walls, namely, in the direction normal to the flow. The evolution equation squeezes the tube diameter, because the motion of the walls of the tube is affine with the deformation. Intuitively, the higher the flow rate, the faster the squeezing process. However, such a decrease of the tube diameter cannot continue indefinitely. In other words, the tube cannot have a zero diameter. The interchain pressure explains why this squeezing stops at some point, with the diameter reaching a steady state value. The authors then link the interchain

pressure to the CCR mechanism through the rate at which the diameter decreases. They argue that, the better the CCR works, the less the tube needs to squeeze. Again this is very reasonable indeed, because, in the ideal situation where all the topological obstacles are removed, the tube could easily keep its original diameter. The relaxation process associated to this radial contraction led Marrucci and Ianniruberto to introduce a new relaxation time, say τ_p, which turned out to be higher than the corresponding Rouse relaxation time. In fact, they estimated that a reasonable comparison with τ_d can be made, although, since they scale differently with the molecular mass, different estimates would be obtained for different materials.

The introduction of models including chain stretch and CCR mechanisms, together with the original reptation, led to significant improvements, especially from a quantitative point of view. The introduction of the CCR originally proposed by Marrucci [75] is able to reproduce the difference between uniaxial and biaxial elongation. In this regard, we have to remember that, in the filament stretching, one of the bigger problems arises from the shear flow induced next to the plates. Such flows become much more relevant when the elongation is biaxial, and the higher the strain rate, the stronger the effect of the CCR. In fact, it acts as an aid for the shear flow close to the plates, where otherwise the chains would become totally aligned to the shear direction, and the shear stress will fall to zero, being completely dominated by the extensional flow.

The SCCR (Stretch and Convective Constraint Release) model introduced by Graham et al. [46] shows an excellent agreement across the full range of deformation rates. However, such a model, together with its simplified version, the Rolie-Poly model, introduced by Likhtman and Graham [72], is not satisfactory in the steady extensional regime. The authors believe this is due to the fact that the spring coefficient of proportionality associated with the chain, which is responsible for the stretch in the model, is assumed to be linear. Therefore, when highly nonlinear deformations are analyzed, the model fails. A different way of treating the stretch term is proposed in a 2D model by Ianniruberto and Marrucci [56], even though no analysis of steady

elongation is reported. More successful in this direction are the results from the application of the interchain pressure effect. The results reported by Marrucci and Ianniruberto [76] confirm the experimental data by Bach et al. [3]. The extensional steady-state viscosity is monotonically decreasing with the extensional rate, and the slopes of the curves are very close. One suggestion the authors draw is that the Rouse time is overestimated, which would imply that the experiment simply did not hit the real Rouse time, at the reciprocal of which signs of an upturn should appear. A different option would be to revisit the interchain pressure effect as a stretch mechanism. The evolution of the diameter of the tube, together with affine, volume preserving deformations, might indeed be looked at as a means to account for stretch in the tube. Obviously further investigation in this direction is required. The consistency and validation of such models is outside the scope of the present thesis. Nonetheless, we will refer to several of these aspects throughout the thesis, in an attempt to provide a sufficiently wide research context in which to interpret our results.

Chapter 3

From the Continuous to the Discrete: Temporal and Spatial Approximation

3.1 Introduction

The spatial and temporal discretizations used to solve the governing flow equations are described in this chapter. In section §3.2 of this chapter we will derive the mathematical formulation of the physical problem. The conditions under which this approach is known to be well posed are discussed in §3.2.1 for the continuous case and in §3.2.3 for the discrete formulation. The incorporation of boundary conditions is explained in §3.2.2. Some issues regarding the stability estimates are discussed in §3.2.4. The temporal and spatial discretization techniques are then presented in §3.3 and §3.4, respectively.

Every time scientists make use of mathematical tools to describe a physical phenomenon, a model is derived which ideally aims to capture and predict the physics underlying the process, both qualitatively and quantitatively. The pursuit of these two goals usually relies on analytical modelling and numerical simulations.

So far we have presented and discussed several models to investigate flows of viscoelastic fluids, which is the object of our research. In this chapter we turn our attention to the next step: the discretization of such models and the subsequent iterative solution of the resulting systems of algebraic equations.

Unsteady problems such as fluid flows need to be discretized in time and space. Temporal discretization is usually performed by means of a finite difference scheme which replaces the time or material derivative by some approximation. Once the continuous time dependence has been removed, the equations are fixed for each time coordinate and the resulting equation is said to be semi-discrete. The spatial dependence has then to be approximated. The spatial discretization process for a system of partial differential equations consists in determining values of the flow variables at some points of the domain (called *nodes*), rather than their analytical expressions. Two basic distinctions have to be made in order to give a rough classification of discretization methods. The first one is geometrical: we can try to solve our problem just once for all on the whole domain, over which we place our nodes; or we can decompose it into smaller parts called *elements* and apply our numerical methods to each of them. The latter technique has been named *domain decomposition.*

Once we have decided how to treat our geometry, then we need to choose what to do with the equations. In the second distinction, this time numerical: one can take the differential (*strong*) formulation of the problem and directly replace the functions and derivatives involved by approximate values at the nodes; this is the approach usually used to deal with time derivatives. A second approach is instead to transform the differential problem to its weak formulation (*variational form*) and evaluate the integrals appearing using some quadrature rule on a certain grid.

Spectral Element Methods are *domain decomposition* methods and approximate the *variational form* of the continuous problem. When applied to a system already semi-discretized in time, they give rise to a linear system at

each time step which can be inverted to yield the solution at that time.

3.2 Mathematical formulation

The first step in the application of spectral element methods to the solution of a system of partial differential equations is the transformation of the problem from its strong, differential form into the weak formulation. We will present a general description of the application of the method to the Stokes problem. There are some theoretical results that are available for the Stokes problem and these will be presented here.

3.2.1 Continuous Stokes problem: compatible spaces and compatibility conditions

There are two primitive variable formulations, the 2-fields and 3-fields formulations, respectively, of the equations governing Stokes flow, the particular case of a steady flow without convection. Let Ω be a bounded and connected subset of $\mathbb{R}^2$ with a Lipschitz continuous boundary $\partial\Omega$. Let $\vec{F} \in [H^{-1}(\Omega)]^2$ and $\vec{u}_\Gamma \in [H^{-1/2}(\Omega)]^2$ such that

$$\int_{\partial\Omega} \vec{u}_\Gamma \cdot \vec{n}\, ds = 0, \tag{3.1}$$

where $\vec{n}$ is the unit outward normal to $\partial\Omega$.

- 2 fields formulation of the Stokes problem: the unknowns are velocity and pressure

$$\begin{aligned} -\eta\nabla^2\vec{u} + \nabla p &= \vec{F}, \qquad in\ \Omega && (3.2)\\ \nabla \cdot \vec{u} &= 0, \qquad in\ \Omega && (3.3)\\ \vec{u} &= \vec{u}_\Gamma, \qquad on\ \partial\Omega. && (3.4) \end{aligned}$$

- 3 fields formulation of the Stokes problem: the unknowns are velocity, pressure and stress

$$\begin{aligned} \nabla p - \nabla \cdot \boldsymbol{T} &= \vec{F}, \qquad in\ \Omega & (3.5)\\ \nabla \cdot \vec{u} &= 0, \qquad in\ \Omega & (3.6)\\ \boldsymbol{T} &= 2\eta \boldsymbol{d} \qquad in\ \Omega & (3.7)\\ \vec{u} &= \vec{u}_\Gamma, \qquad on\ \partial\Omega. & (3.8) \end{aligned}$$

Note that in three dimensions the first is a problem in terms of four scalar unknowns, as opposed to the ten scalar unknowns for the second problem. Obviously, the equations have to be supplemented by the corresponding boundary conditions for the particular flow. The last equation in both cases is a boundary condition on the velocity. Finally $\boldsymbol{d} = \frac{1}{2}[\nabla\vec{u} + \nabla\vec{u}^T]$ is the rate of deformation (strain) tensor.

The two formulations above are strong formulations of the Stokes problem. They involve the existence of the derivatives of the unknown functions pointwise up to a certain order. Since spectral element methods are based on a Galerkin approach, the following weak formulation will be analyzed. Let

$$[H^1_D(\Omega)]^2 = \{\vec{u} \in [H^1(\Omega)]^2 \ : \ \vec{u} = \vec{u}_\Gamma\ on\ \partial\Omega\}. \tag{3.9}$$

In this notation, superscripts indicate the weak regularity of functions in the space while subscripts, where present, the value of the functions on the boundary. So for example, the space defined in 3.9, comprises the functions which are weakly differentiable up to the first order, and attain a certain, specified value on the boundary. Also, let $\vec{w} \in [H^1_0(\Omega)]^2$, $q \in L^2_0(\Omega)$ and $\boldsymbol{T} \in [L^2(\Omega)]^4_s$ (subscript s means that T is in the space of symmetric tensors), be test functions for the velocity, pressure and stress in the corresponding spaces. So we multiply (3.5), (3.6), (3.7), respectively, by these test functions, and integrate over Ω. We can now state the weak formulation of the 3-fields Stokes problem:

find $(p, \vec{u}, \boldsymbol{T}) \in [L^2_0(\Omega)] \times [H^1_D(\Omega)]^2 \times [L^2(\Omega)]^4_s$ such that, for all $(q, \vec{w}, \boldsymbol{z}) \in [L^2_0(\Omega)] \times [H^1_0(\Omega)]^2 \times [L^2(\Omega)]^4$, the following equations are satisfied:

$$b(p,\vec{w}) + d(\boldsymbol{T},\vec{w}) = l(\vec{w}), \tag{3.10}$$

$$b(q,\vec{u}) = 0, \tag{3.11}$$

$$c(\boldsymbol{T},\boldsymbol{z}) = d(\boldsymbol{z},\vec{u}), \tag{3.12}$$

where b, c, d and l are, respectively, three bilinear forms and a linear functional defined as follows:

$$b : L_0^2(\Omega) \times [H^1(\Omega)]^2,\ b(r,\vec{v}) = \int_\Omega (\nabla \cdot \vec{v})\ r\ d\Omega; \tag{3.13}$$

$$c : [L^2(\Omega)]_s^4 \times [L^2(\Omega)]_s^4\ , c(\boldsymbol{S},\boldsymbol{T}) = \int_\Omega \boldsymbol{S} : \boldsymbol{T}\ d\Omega; \tag{3.14}$$

$$d : [L^2(\Omega)]_s^4 \times [H^1(\Omega)]^2\ , d(\boldsymbol{S},\vec{u}) = \int_\Omega \tilde{S} : \nabla\vec{u}\ d\Omega; \tag{3.15}$$

$$l : [H^1(\Omega)]^2\ , l(\vec{u}) = \int_\Omega \vec{F}\cdot\vec{u}\ d\Omega. \tag{3.16}$$

While (3.11) and (3.12) are just derived by integration by parts, (3.10) requires the use of the following differential relations:

$$\boldsymbol{S} : \nabla\vec{w} = \nabla\cdot(\boldsymbol{T}\vec{w}) - \vec{w}\cdot(\nabla\cdot\boldsymbol{T})$$

$$\nabla\cdot(\vec{w}p) = p(\nabla\cdot\vec{w}) + \vec{w}\cdot\nabla p.$$

The divergence theorem is then used exploiting the fact that the velocity test function $\vec{w}$ vanishes on the boundary.

Now that the problems have been set and a weak formulation is available, we turn our attention to well-posedness issues. If we have a look at either (3.2)-(3.4) or (3.5)-(3.8), we realize they are both mixed problems, namely, their solutions belong to different spaces. There are two different spaces in the two fields case, and three for (3.5)-(3.8). Some conditions relating the different spaces are then required. We will first analyze the two fields problem, whose detailed analysis is given, for example, by Brenner and Scott [16] (chapter 12) or Schwab [113] (chapter 5).

The weak form of (3.2)-(3.4), which is derived in exactly the same way as (3.5)-(3.8) by multiplying (3.2) and (3.3) by test functions $\vec{w}$ and q, respectively, reads: find $\vec{u} \in [H_D^1(\Omega)]^2$ and $p \in L_0^2(\Omega)$ such that

$$\begin{aligned} \eta \int_\Omega \nabla \vec{u} : \nabla \vec{w} \, d\Omega - \int_\Omega (\nabla \cdot \vec{w}) p \, d\Omega \\ = \int_\Omega \vec{F} \cdot \vec{w} \qquad \forall \vec{w} \in [H_0^1(\Omega)]^2 \end{aligned} \tag{3.17}$$

$$\int_\Omega (\nabla \cdot \vec{u}) q \, d\Omega = 0 \qquad \forall q \in L^2(\Omega). \tag{3.18}$$

We just remark that, in this case, an integration-by-parts has been performed to rewrite the second-order term on the left-hand side of (3.2).

If we now define the space

$$Z = \{\vec{u} \in [H_0^1(\Omega)]^2 \ : \ \int_\Omega (\nabla \cdot \vec{u}) p \, d\Omega = 0\}, \tag{3.19}$$

the problem, in which $\vec{u}$ is determined, is then equivalent to finding $\vec{u} \in Z_D$ such that

$$\eta \int_\Omega \nabla \vec{u} : \nabla \vec{w} \, d\Omega = \int_\Omega \vec{F} \cdot \vec{w} \qquad \forall \vec{w} \in Z, \tag{3.20}$$

where

$$Z_D = \{\vec{w} \in [H_D^1(\Omega)]^2 \ : \ \int_\Omega (\nabla \cdot \vec{w}) p \, d\Omega = 0\}$$

The existence and uniqueness of a velocity field satisfying the problem can be found by applying the Lax-Milgram theorem and the Poincaré-Friederichs inequality to prove the coercivity of the bilinear form

$$a : [H_0^1(\Omega)]^2 \times [H_0^1(\Omega)]^2 \, , a(\vec{u}, \vec{w}) = \int_\Omega \nabla \vec{u} : \nabla \vec{w} \, d\Omega.$$

We now turn our attention to the existence of a solution for the pressure, which clearly has to be coupled with the velocity field. After a velocity field

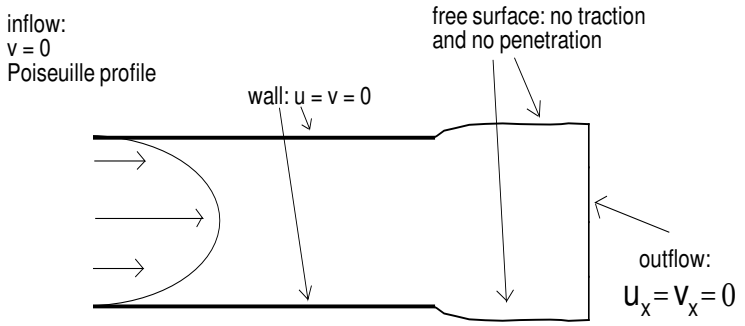

Figure 3.1: Fluid jet from a die.

$\vec{u} \in Z$ has been determined by solving (3.20) , we need now to find $p \in L^2_0(\Omega)$ such that

$$\eta \int_\Omega \nabla \vec{u} : \nabla \vec{w} \; d\Omega - \int_\Omega (\nabla \cdot \vec{w}) p \; d\Omega = \int_\Omega \vec{F} \cdot \vec{w} \qquad \forall \vec{w} \in H^1(\Omega). \tag{3.21}$$

Babuška [2] and Brezzi [17] proved independently that existence and uniqueness for (3.21) is guaranteed provided that the following condition, called the *compatibility condition* or *inf-sup condition*, holds:

$$\sup_{\vec{w} \in [H^1(\Omega)]^2} \frac{\int_\Omega (\nabla \cdot \vec{w}) p \; d\Omega}{\| \vec{u} \|_{[H^1(\Omega)]^2}} \geq \beta \| p \|_{L^2_0(\Omega)} . \tag{3.22}$$

The constant $\beta > 0$ is sometimes called the **inf-sup constant**. The proof comes from the algebra of abstract operators, and details can also be found in Brenner and Scott [16] (chapter 12), in which the Riesz representation theorem is widely used, and Schwab [113] (chapter 5) who solves a saddle problem by mean of the closed range theorem.

In the case of three fields formulation, it is clear that something more is required; intuitively the stress field, which does not appear in the two fields case, should obey some kind of coupling condition. The theory on which such an analysis relies was proposed by Fortin and Fortin [37]. Successively,

based on this approach, Gerritsma and Phillips [40] also derived an extra *inf-sup condition* coupling stress and velocity. To guarantee existence and uniqueness of the problem (3.10)-(3.12), together with the Babuška-Brezzi condition (3.22), the following has to hold:

$$\sup_{\tilde{\sigma}\in[L^2(\Omega)]^4} \frac{\mid d(\tilde{\sigma},\vec{w}) \mid}{\parallel \tilde{\sigma} \parallel_{[L^2(\Omega)]^4}} \geq \beta \parallel \vec{w} \parallel_{[H_0^1]^2}, \forall\, \vec{w} \in [H_0^1(\Omega)]^2. \tag{3.23}$$

A similar compatibility analysis was performed by the rheology group at the University of Swansea [9, 8]. Their work also started from the theory of Fortin and Fortin [37] and was developed to ensure compatible approximation of velocity and stress in the case of an alternative sub-cell discretization scheme.

3.2.2 Incorporating boundary conditions and surface tension effects

The following boundary conditions are satisfied on the free surface. First, we have the kinematic condition that no fluid particles can cross the interface. This means that the normal component of the mesh velocity $\vec{v}$ is that of the interface, i.e.

$$\vec{v} \cdot \vec{n} = \vec{u} \cdot \vec{n}, \tag{3.24}$$

where $\vec{n}$ is the unit outward normal to the free surface. At steady state, the mesh velocity vanishes and the no-penetration condition

$$\vec{u} \cdot \vec{n} = 0, \tag{3.25}$$

is satisfied. Secondly, the force balance due to surface tension

$$\boldsymbol{\tau}\vec{n} = \sigma\kappa\vec{n}, \tag{3.26}$$

where κ represents the curvature of the free surface, which for a plane curve $y = f(x)$ is given by

$$\kappa = \frac{y''}{[1 + (y')^2]^{3/2}},$$

and σ is the dimensionless surface tension parameter. Finally, the zero-traction condition requires that the shear stress, τ_{xy}, has to be zero on the free surface. As shown in Fig. 3.1, the usual Neumann conditions are applied at the outflow.

If surface tension is neglected ($\sigma = 0$), then the right hand side of Eq. (3.26) vanishes. Not all of the conditions on the free surface can be imposed. Later in this section we explain which one we impose, why, and in which way. On the other hand, in the numerical simulations we check that the boundary conditions which are not imposed are satisfied.

We write down the momentum balance in terms of the stress tensor when the external forces are neglected. We follow the idea originally developed by Ruschak [107] and then extended to a spectral framework by Ho and Patera [51] and Ho and Rønquist [52]. We denote $\partial\Omega(t)$ as the boundary of the time-dependent domain $\Omega(t)$. In particular, $\Gamma_D(t)$ and $\Gamma_N(t)$ are the parts of the boundary where Dirichlet and Neumann conditions on the velocity apply, respectively. Moreover, we define

$$[H^1_D(\Omega(t))]^2 = \{\vec{u} \in [H^1(\Omega(t))]^2 \ : \vec{u} = \vec{u}_D \ on \ \Gamma_D(t)\}.$$

Multiplying the semi-discrete equation by a test function (in the space of the velocities) and integrating over the domain Ω we obtain:

$$\int_{\Omega(t)} \Big[Re\Big(\frac{\partial \vec{u}}{\partial t} + (\vec{u}\cdot\nabla)\vec{u}\Big)\Big]\vec{w}\ d\Omega(t) = -\int_{\Omega(t)} (\nabla p)\vec{w}\ d\Omega(t) + \int_{\Omega(t)} (\nabla\cdot\boldsymbol{\tau})\vec{w}\ d\Omega(t) + \int_{\Omega(t)} \vec{F}\vec{w}\ d\Omega(t), \qquad \forall \vec{w} \in W \tag{3.27}$$

The boundary of $\Omega(t)$ is split into $\Gamma_D(t)$, where Dirichlet conditions are applied, and $\Gamma_N(t)$, where homogeneous Neumann conditions hold.

We now transform the two integrals featuring a differential operator on the right-hand side of Eq. (3.27) by applying a vector-scalar and a vector-tensor identity, respectively. The first reads as follows:

$$\int_{\Omega(t)} (\nabla p) \cdot \vec{w}\, d\Omega(t) = \int_{\Omega(t)} \nabla \cdot (p\vec{w})\, d\Omega(t) - \int_{\Omega(t)} p(\nabla \cdot \vec{w})\, d\Omega(t)$$

then, by means of the divergence theorem for the first term on the right-hand side

$$\int_{\Omega(t)} (\nabla p) \cdot \vec{w}\, d\Omega(t) = \int_{\Gamma_N(t)} (p\vec{w} \cdot \vec{n})\, d\Gamma_N(t) - \int_{\Omega(t)} p(\nabla \cdot \vec{w})\, d\Omega(t)$$

Note that the test function vanishes on the Dirichlet part of the boundary.

In the same fashion, we use the tensor-vector relation:

$$\int_{\Omega(t)} (\nabla \cdot \boldsymbol{\tau}) \cdot \vec{w}\, d\Omega(t) = \int_{\Omega(t)} \nabla \cdot (\boldsymbol{\tau}\vec{w})\, d\Omega(t) - \int_{\Omega(t)} (\boldsymbol{\tau} : \nabla\vec{w})\, d\Omega(t)$$

and apply the divergence theorem to the first integral on the right-hand side of Eq. (3.27) to obtain

$$\int_{\Omega(t)} (\nabla \cdot \boldsymbol{\tau}) \cdot \vec{w}\, d\Omega(t) = \int_{\Gamma_N(t)} (\boldsymbol{\tau}\vec{w}) \cdot \vec{n}\, d\Gamma_N(t) - \int_{\Omega(t)} (\boldsymbol{\tau} : \nabla\vec{w})\, d\Omega(t).$$

Thus we can recast Eq. (3.27) in the following form:

$$\begin{aligned} &\int_{\Omega(t)} \Big[Re\Big(\frac{\partial \vec{u}}{\partial t} + (\vec{u} \cdot \nabla)\vec{u}\Big)\Big]\vec{w}\, d\Omega(t) + \int_{\Omega(t)} (\boldsymbol{\tau} : \nabla\vec{w})\, d\Omega(t) \\ &+ \int_{\Omega(t)} p(\nabla \cdot \vec{w})\, d\Omega(t) = \int_{\Gamma_N(t)} (\boldsymbol{\tau}\vec{w}) \cdot \vec{n}\, d\Gamma_N(t) - \int_{\Gamma_N(t)} (p\vec{w} \cdot \vec{n})\, d\Gamma_N(t) \end{aligned} \tag{3.28}$$

The right-hand side incorporates all the Neumann boundary integrals and resembles the weak normal jump in the total stress. This is a natural means for incorporating the boundary condition for the normal stress jump according to Eq. (3.26):

$$\int_{\Gamma_N(t)} (\boldsymbol{\tau}\vec{w}) \cdot \vec{n}\, d\Gamma_N(t) - \int_{\Gamma_N(t)} (p\vec{w} \cdot \vec{n})\, d\Gamma_N(t) = \int_{\Gamma_N(t)} \boldsymbol{T}\vec{w} \cdot \vec{n} = 0. \tag{3.29}$$

When surface tension, say σ, is relevant, this condition is made dimensionless by means of the Weber number defined as $We = \frac{\rho U^2 L}{\sigma}$ and the normal stress jump is balanced as follows:

$$\int_{\Gamma_N(t)} \boldsymbol{T}\vec{w} \cdot \vec{n}\, d\Gamma_N(t) = \left(\frac{Re}{We}\right) \int_{\Gamma_N(t)} \kappa\vec{w} \cdot \vec{n}\, d\Gamma_N(t). \tag{3.30}$$

A similar procedure can be performed starting from the two fields formulation, where an integration by parts of the integral of the Laplacian will give rise to a boundary integral featuring the normal velocity which vanishes on the free surface. Therefore, it is a natural means to include the no-penetration condition (3.25) rather than (3.26). See [15] for further details. Since surface tension is neglected here there is no contribution from the integral in Eq. (3.29), and the two approaches are equivalent.

3.2.3 Discrete Stokes problem: compatibility conditions

We revert our attention again to the weak formulation of the two fields Stokes problem: find $\vec{u} \in [H_0^1(\Omega)]^2$ and $p \in L_0^2(\Omega)$ such that

$$\begin{aligned} \eta \int_\Omega \nabla\vec{u} : \nabla\vec{w}\, d\Omega - \int_\Omega (\nabla \cdot \vec{w}) p\, d\Omega & \\ = \int_\Omega \vec{F} \cdot \vec{w} \qquad \forall \vec{w} \in [H_0^1(\Omega)]^2, & \end{aligned} \tag{3.31}$$

$$\int_\Omega (\nabla \cdot \vec{u}) q\, d\Omega = 0 \qquad \forall q \in L^2(\Omega). \tag{3.32}$$

One approach is the one described in §3.2.1; we solve the problem for the velocity in the space defined in (3.19) and then we analyze the behavior of the pressure. A second approach would be the other way around. The space

$$Z = \{w \in H_0^1(\Omega) \ : \ \int_\Omega (\nabla \cdot \vec{w}) p\, d\Omega = 0\}, \tag{3.33}$$

can be seen as the kernel of the weak divergence operator acting on the velocity. If we consider instead the space

$$S_m = \{q \in L_0^2(\Omega) \ : \ \int_\Omega (\nabla \cdot \vec{u}) q\, d\Omega = 0\}, \tag{3.34}$$

this is the kernel of the operator dual to the weak divergence operator. This is the weak gradient acting on the pressure. The second approach then would be to look for a pressure solution in the space $S_m^{\perp}$, namely the space which is orthogonal to the dual space of Z. This restriction is also equivalent to (3.22) (see Babuška [2] or Brezzi [17], for instance).

Maday et al. [73] used this approach to derive the discrete compatibility condition which ensures that the discrete velocity and pressure fields are coupled correctly, with no presence of so called *spurious modes* for the pressure. These modes, which are physically meaningless, are absent if the polynomials approximating the pressure are two degrees lower than the ones approximating the velocity. This condition has been derived by Maday et al. in [73] and it reads:

the spaces $(P_N \otimes P_N)^2$ and $P_{N-2} \otimes P_{N-2}$, as approximation spaces for the velocity and pressure fields respectively, are compatible with respect to the condition (3.22).

In the aforementioned condition, $\otimes$ is the tensor product. Once this condition has been satisfied, the approximation process can be performed. The velocity and pressure fields have to be approximated, not in the original infinite dimensional spaces $[H^1(\Omega(t))]_D^2$ and $L^2(\Omega(t))$, but in finite dimensional subspaces. The physical domain $\Omega(t)$ is divided into M non-overlapping spectral elements $\Omega_m(t)$, $1 \leq m \leq M$, such that $\cup_{m=1}^{M} \Omega_m(t) = \Omega(t)$. We denote by $\mathbb{P}_N(\Omega_m(t))$ the space of all polynomials on $\Omega_m(t)$ of degree less than or equal to N, and further define $P_N(\Omega(t)) = \{\phi : \phi|_{\Omega_m(t)} \in \mathbb{P}_N(\Omega_m(t))\}$. Each of the spectral elements is mapped onto the parent element $D = [-1,1] \times [-1,1]$, where each point $(\xi, \eta) \in D$ is associated with a point $(x(\xi,\eta), y(\xi,\eta)) \in \Omega_k(t)$. The dependent variables are approximated on D using Lagrangian interpolants of degree N in both spatial directions, based on the Gauss-Lobatto-Legendre points. These interpolants are given explicitly by

$$h_i(\xi) = -\frac{(1-\psi^2)L_N'(\xi)}{N(N+1)L_N(\xi_i)(\xi - \xi_i)} \qquad i = 0, \ldots, N. \tag{3.35}$$

and

$$\tilde{h}_i(\xi) = -\frac{(1-\xi_i^2)L'_N(\psi)}{N(N+1)L_N(\xi_i)(\xi-\xi_i)} \qquad i = 1,\ldots,N-1. \tag{3.36}$$

and satisfy the conditions $h_i(\xi_j) = \delta_{ij},\ i,j = 0,\ldots,N$ and $\tilde{h}_i(\xi_j) = \delta_{ij},\ i,j = 1,\ldots,N-1$. This creates a Gauss-Lobatto-Legendre grid inside the spectral elements. The representations for the velocity, pressure and stress on the parent element are

$$\vec{u}_N(\psi,\zeta) = \sum_{i,j=0}^{N} \vec{v}_N^{i,j} h_i(\psi) h_j(\zeta), \tag{3.37}$$

$$p_N(\psi,\zeta) = \sum_{i,j=1}^{N-1} p_N^{i,j} h_i(\psi) h_j(\zeta), \tag{3.38}$$

$$\boldsymbol{\tau}_N(\psi,\zeta) = \sum_{i,j=0}^{N} \boldsymbol{\tau}_N^{i,j} h_i(\psi) h_j(\zeta). \tag{3.39}$$

The whole discretization process involves two different kinds of errors: the first comes from the approximation of $L_0^2(\Omega)$ by Π_N, $[H_0^1]^2$ by Λ_N and $[L_s^2(\Omega)]^4$ by Σ_N. This is exactly the error incurred by projecting the solution from the infinite dimensional space on to the N-dimensional space. The second is the quadrature error in computing the integrals. The error estimates finally read as follows:

$$\| \vec{u} - \vec{u}_N \|_{[H_0^1(\Omega)]^2} \leq cN^{1-m} \| \vec{u} \|_{[H^m(\Omega)]^2}, \tag{3.40}$$

$$\| p - p_N \|_{L^2(\Omega)} \leq cN^{2-m}(\| \vec{u} \|_{[H^m(\Omega)]^2} + \| p \|_{H^{m-1}(\Omega)}). \tag{3.41}$$

Equations (3.40) and (3.41) clearly require that $p \in H^{m-1}(\Omega)$ and $\vec{u} \in [H^m(\Omega)]^2$.

Details on this error analysis for the Stokes problem can be found, for instance, in Bernardi and Maday [10] or Schwab [113], while the reader interested in a more general treatment of the polynomial approximation and error estimation in Sobolev spaces will again find useful Brenner and Scott [16] (chapter 4).

Compatibility and error analysis for the three fields case has been performed instead by Gerritsma and Phillips in [40], and the authors determined that the following condition has to hold in order for the discrete problem to be well posed:

the space $(P_N \otimes P_N)^4_s$, together with the spaces $(P_N \otimes P_N)^2$ and $(P_{N-2} \otimes P_{N-2})$ are compatible spaces for the approximation of the stress, velocity and pressure fields, respectively.

The corresponding error estimates read

$$\| \boldsymbol{\tau} - \boldsymbol{\tau}_N \|_{[L^2(\Omega)]^4} \leq c[N^{1-m}(\| \boldsymbol{\tau} \|_{[L^2(\Omega)]^4} + \| \vec{u} \|_{[H^1_0(\Omega)]^2})], \tag{3.42}$$

$$\| \vec{u} - \vec{u}_N \|_{[H^1_0(\Omega)]^2} \leq c[N^{1-m}(\| \boldsymbol{\tau} \|_{[L^2(\Omega)]^4} + \| \vec{u} \|_{[H^1_0(\Omega)]^2})], \tag{3.43}$$

$$\| p - p_N \|_{L^2(\Omega)} \leq c[N^{\frac{3}{2}-m}(\| \boldsymbol{\tau} \|_{[L^2(\Omega)]^4} + \| \vec{u} \|_{[H^1_0(\Omega)]^2} + \| p \|_{L^2(\Omega)})]. \tag{3.44}$$

Note that (3.44) is not optimal, but it's sharper by a factor 1/2 compared with (3.41), and the reason behind it is that Bernardi and Maday [10] used the space $(P_{N-2} \otimes P_{N-2})$ to approximate the pressure, while in the practical computation of the error, $(P_N \otimes P_N)$ is the space used by Gerritsma and Phillips in [40].

3.2.4 Stability estimates for the stress tensor

This section is mainly devoted to the derivation of a stability estimate for the extra-stress tensor in the three formulation of the Stokes problem.

Stability estimates measure how the norm of the solution depends on the norm of the data. Stability clearly means that a small perturbation of the data does not affect the solution. For the two fields Stokes problem, stability estimates for the velocity and the pressure read as follows (see, for instance, Bernardi and Maday [10]):

$$\| \vec{u}_N \|_{[H^1(\Omega)]^2} \leq c \| \vec{F} \|_{[H^{-1}(\Omega)]^2}, \tag{3.45}$$

$$\| p_N \|_{L^2(\Omega)} \leq c\beta_N^{-1} \| \vec{F} \|_{[H^{-1}(\Omega)]^2} . \tag{3.46}$$

The difference between these two inequalities is the factor β_N, which depends on N. Therefore, for the pressure, stability depends on the order of the approximating polynomials.

In order to derive an estimate analogous to (3.45)-(3.46), we write down again the compatibility conditions involving velocity and stress derived by Gerritsma and Phillips [40] :

$$\sup_{\tilde{\sigma} \in [L^2(\Omega)]^4} \frac{\int_\Omega \tilde{\sigma} : \nabla \vec{u}}{\| \tilde{\sigma} \|_{[L^2(\Omega)]^4}} \geq \beta \| \vec{w} \|_{[H_0^1(\Omega)]^2}, \forall \vec{w} \in [H_0^1(\Omega)]^2. \tag{3.47}$$

This condition has been derived with an abstract approach, namely, using the **closed range theorem**; if D is the operator arising from the form d defined in the weak formulation as

$$d : [L^2(\Omega)]^4 \times [H^1(\Omega)]^2 , d(\tilde{S}, \vec{u}) = \int_\Omega \tilde{S} : \nabla \vec{u} \, d\Omega, \tag{3.48}$$

and D' is its adjoint, the abstract condition

$$\sup_{\tilde{\sigma} \in \Sigma} \frac{| d(\tilde{\sigma}, \vec{w}) |}{\| \tilde{\sigma} \|_\Sigma} \geq \beta \| \vec{w} \|_{\Xi / Ker D'}, \qquad \forall \vec{w} \in \Xi, \tag{3.49}$$

results in the compatibility condition (3.47), since $Ker\ D' = \{\vec{0}\}$ in $[H_0^1(\Omega)]^2$.

According to the closed range theorem (see, e.g., Schwab [113] for the details) we can swap velocity and stress without changing our constant β, in order to obtain

$$\sup_{\vec{v} \in [H_0^1(\Omega)]^2} \frac{\int_\Omega \tilde{\sigma} : \nabla \vec{v}}{\| \vec{v} \|_{[H^1(\Omega)]^2}} \geq \beta \| \tilde{\sigma} \|_{[L^2(\Omega)]^4}, \forall \tilde{\sigma} \in [L^2(\Omega)]^4. \tag{3.50}$$

This condition still holds when we approximate the problem in the subspace, and it reads as follows:

$$\sup_{\vec{v}_N \in (P_N \otimes P_N)^2} \frac{\int_\Omega \tilde{\sigma}_N : \nabla \vec{v}_N}{\| \vec{v}_N \|_{[H^1(\Omega)]^2}} \geq \beta_1 \| \tilde{\sigma}_N \|_{[L^2(\Omega)]^4}, \forall \tilde{\sigma}_N \in (P_N \otimes P_N)^4_s, \quad (3.51)$$

with $\beta_1 = \beta / C$ and C is the continuity constant for the L^2 orthogonal projector for the stress field.

The momentum equation in the weak 3-fields formulation is

$$\int_\Omega (\nabla \cdot \vec{v}_N) p + \int_\Omega \tilde{\sigma}_N : \nabla \vec{v}_N = \int_\Omega \vec{F} \cdot \vec{v}_N \qquad \forall \vec{v}_N \in (P_N \otimes P_N)^2 \cap [H^1_0(\Omega)]^2 \quad (3.52)$$

so we can write

$$\begin{aligned}
\| \tilde{\sigma}_N \|_{[L^2(\Omega)]^4} &\leq \beta_1^{-1} \sup_{\vec{v}_N \in (P_N \otimes P_N)^2} \frac{-\int_\Omega (\nabla \cdot \vec{v}_N) p + \int_\Omega \vec{F} \cdot \vec{v}_N}{\| \vec{v}_N \|_{[H^1(\Omega)]^2}} && (3.53)\\
&= \beta_1^{-1} \sup_{\vec{v}_N \in (P_N \otimes P_N)^2} \frac{-\eta \int_\Omega \nabla \vec{u}_N : \nabla \vec{v}_N + 2 \int_\Omega \vec{F} \cdot \vec{v}_N}{\| \vec{v}_N \|_{[H^1(\Omega)]^2}} && (3.54)\\
&\leq \beta_1^{-1} (\eta C_{cont} \| \vec{u}_N \|_{[H^1(\Omega)]^2} + 2 \| \vec{F} \|_{[L^2(\Omega)]^2}) && (3.55)\\
&\leq \beta_1^{-1} (\eta C_{cont} C^V_{stab} \| \vec{F} \|_{[L^2(\Omega)]^2} + 2 \| \vec{F} \|_{[L^2(\Omega)]^2}) && (3.56)\\
&\leq [\beta_1^{-1} (\eta C_{cont} C^V_{stab} + 2)] \| \vec{F} \|_{[L^2(\Omega)]^2} \ . && (3.57)
\end{aligned}$$

In the second inequality above we used the continuity of the bilinear form a in the 2-fields weak formulation, namely,

$$a : [H^1_0(\Omega)]^2 \times [H^1_0(\Omega)]^2 \ , a(\vec{u}, \vec{w}) = \int_\Omega \nabla \vec{u} : \nabla \vec{w} \, d\Omega,$$

and C_{cont} is the corresponding continuity constant; while in the last inequality we applied the stability estimate for the approximation of the velocity (basically the inequality (3.45), see Bernardi and Maday [10]), and C^V_{stab} is the stability constant.

So finally we obtain the stability estimate for approximation of the stress field:

$$\| \tilde{\sigma}_N \|_{[L^2(\Omega)]^4} \leq C^S_{stab} \| \vec{F} \|_{[L^2(\Omega)]^2}, \tag{3.58}$$

with $C^S_{stab} = [\beta_1^{-1}(\eta C_{cont} C^V_{stab} + 2)]$. Note that in the stability sense the stress has a behaviour similar to the velocity, namely, its stability constant does not depend on N, while it does for the pressure approximation. This is to be expected since the approximation space for the extra-stress tensor is of the same order as the approximation space for the velocity. On the other hand this behaviour also tells us that, for measuring the stability of the approximated solution at the discrete level, it does not matter that the components of the extra-stress tensor are in the same space as the pressure in the original continuous problem, namely $L^2(\Omega)$.

3.3 Temporal discretization

Material derivatives are present in both the momentum and constitutive equations. In both cases, the semi-discretization in time is accomplished using an operator integration factor splitting (OIFS) method [74] of first or second order, together with the employment of an Arbitrary Langrangian Eulerian (ALE) technique. More precisely, in the case of a first-order approximation, the material derivative is approximated as follows:

$$\frac{DG}{Dt} \approx \frac{G^{n+1} - (\tilde{G})^{n+1}}{\Delta t}, \tag{3.59}$$

where $\tilde{G}$ is the solution at time $t = t^{n+1}$ of the pure advection problem

$$\frac{\partial \tilde{G}}{\partial t} + (G^n - \vec{v}^n) \cdot \nabla \tilde{G} = 0, \tag{3.60}$$

with initial condition $\tilde{G}(t^n) = G^n$.
A second-order approximation (OIFS2) is

$$\frac{DG}{Dt} \approx \frac{3G^{n+1} - 4(\tilde{G}_1)^{n+1} + (\tilde{G}_2)^{n+1}}{2\Delta t}, \tag{3.61}$$

where $\tilde{G}_1$, $\tilde{G}_2$ are solutions of the pure advection problems

$$\frac{\partial \tilde{G}_1}{\partial t} + (G^* - \vec{v}^n) \cdot \nabla \tilde{G}_1 = 0 \tag{3.62}$$

$$\frac{\partial \tilde{G}_2}{\partial t} + (G^* - \vec{v}^n) \cdot \nabla \tilde{G}_2 = 0, \tag{3.63}$$

respectively. In Eq. (3.60), (3.62) an (3.63) $\vec{v}^n$ is the mesh velocity at $t^n = n\Delta t$ used in the ALE formulation. The method of calculating $\vec{v}^n$ is described in §3.4.3. The corresponding initial conditions are given by $\tilde{G}_1(t^n) = G^n$ and $\tilde{G}_2(t^{n-1}) = G^{n-1}$ and G^* is a second-order approximation in time for G given by

$$G^* = \frac{t - t^{n-1}}{\Delta t} G^n + \Big(1 - \frac{t - t^{n-1}}{\Delta t}\Big) G^{n-1}. \tag{3.64}$$

The pure advection problems (3.60), (3.62) and (3.63) are solved numerically using an explicit $4th$ order Runge-Kutta method.

Both schemes are used in the numerical simulations of Newtonian die swell in Chapter 4. A few remarks on the performance of the two schemes are also presented. However, the second-order scheme is preferred in the numerical simulations of extrusion of a viscoelastic fluid, in both the momentum and constitutive equations.

3.3.1 Semi-discretized equations for different models

The application of the OIFS scheme transforms the problem from its continuous form into a form which is semi-discretized in time. In the Newtonian case, we solve the two-fields problem. The semi-discretized system of equations, when OIFS1 or OIFS2 scheme are used, reads, respectively:

$$\frac{Re}{\Delta t}(\vec{u}^{n+1} - \vec{\tilde{u}}^{n+1}) = -\nabla p^{n+1} + \triangle \vec{u}^{n+1}, \tag{3.65}$$

$$\nabla \cdot \vec{u}^{n+1} = 0, \tag{3.66}$$

and

$$\frac{Re}{2\Delta t}(3\vec{u}^{n+1} - 4(\vec{\tilde{u}}_1)^{n+1} + (\vec{\tilde{u}}_2)^{n+1}) = -\nabla p^{n+1} + \triangle \vec{u}^{n+1}, \tag{3.67}$$

$$\nabla \cdot \vec{u}^{n+1} = 0. \tag{3.68}$$

The superscript indicates the time level, with $n+1$ being the current time level. In the case of viscoelastic fluids, the constitutive equation is solved separately and OIFS2 is employed. The corresponding semi-discretized formulation for a generic viscoelastic model can be written as

$$\frac{Re}{2\Delta t}(3\vec{u}^{n+1} - 4(\vec{\tilde{u}}_1)^{n+1} + (\vec{\tilde{u}}_2)^{n+1}) = -\nabla p^{n+1} + \nabla \cdot \boldsymbol{\tau}^n + \beta(\triangle \vec{u}^{n+1}), \tag{3.69}$$

$$\nabla \cdot \vec{u}^{n+1} = 0, \tag{3.70}$$

$$f^{n-1}(\boldsymbol{\tau})\boldsymbol{\tau}^n + \frac{Wi}{2\Delta t}(3\boldsymbol{\tau}^n - 4\tilde{\boldsymbol{\tau}}_1^n + \tilde{\boldsymbol{\tau}}_2^n) = 2(1-\beta)\boldsymbol{D}^n - E^{n-1}(\boldsymbol{\tau}, \vec{u}). \tag{3.71}$$

The Laplacian in Eq. (3.69) comes from the decomposition of the stress into viscous and polymeric contributions, $\boldsymbol{\tau}$ being the polymeric part. In Eq. (3.71)

$$f^{n-1}(\boldsymbol{\tau}) = f(\boldsymbol{\tau}^{n-1})$$

and

$$\begin{aligned} E^{n-1}(\boldsymbol{\tau}, \vec{u}) =& E(\boldsymbol{\tau}^{n-1}, \vec{u}^{n-1}) \\ =& (f^{n-1}(\boldsymbol{\tau}^{n-1}) - 1)\frac{1-\beta}{Wi}\boldsymbol{I} \\ &+ \frac{\alpha Wi}{1-\beta}\boldsymbol{\tau}^{n-1} \cdot \boldsymbol{\tau}^{n-1} - Wi(\nabla \vec{u}^{n-1})\boldsymbol{\tau}^{n-1} \\ &- Wi\ \boldsymbol{\tau}^{n-1}(\nabla \vec{u}^{n-1}). \end{aligned} \tag{3.72}$$

If $f(\boldsymbol{\sigma}) = 1$ and $\alpha = 0$ in Eq. (3.71) and (3.72), then the Oldroyd-B model is obtained. Moreover, if also $\beta = 0$ in Eqs. (3.69) and (3.71), then we recover the UCM model. Finally, when $f(\boldsymbol{\sigma})$ takes the form described in Verbeeten et al. [132], the XPP model is retrieved. The last two terms in the right-hand side of Eq. (3.72) represent the deformation terms in the upper convective derivative, $\overset{\triangledown}{\boldsymbol{\tau}}$. The temporal scheme is uncoupled in

the viscoelastic case, namely, the constitutive equation (3.71) is solved first, therefrom the superscript n. This allows for a free choice of test functions, as we will describe in §3.4.2. The value of the stress at the new time level is inserted into the momentum equation. The latter is solved simultaneously with the continuity equation.

3.4 Spatial discretization

Domain decomposition methods are certainly more flexible than methods which solve a problem globally. This is because they give us the chance to solve our problem more accurately where needed; simply think of singularities, obstacles and anything else which could imply some steep gradient of the quantities involved; the price to pay is in the computational cost of storing the data.

To derive the weak formulation of a problem we need new spaces of functions (*test spaces*), so a theoretical effort is required if we want to make sure that the new problem is well posed. The advantage from a practical point of view is that with the use of these test spaces, which can be more or less arbitrarily chosen, less regularity in the solutions will be required (see §3.2.1).

Pioneered by Patera [96], spectral element methods (SEM) are similar to finite element methods (FEM) because of their common domain decomposition approach and their approximation of the weak formulation of the governing equations. The main difference lies in the choice of basis functions in the approximation space: FEM uses a hierarchical basis, namely a set of polynomials of increasing degree. In spectral element methods, Jacobi polynomials are used on a Gauss-Lobatto-Jacobi grid (see §3.4.1). A comparison between these approaches, as well as several applications, can be found for instance in the monograph of Karniadakis and Sherwin [61]. Literature on the FEM is extensive. Brenner and Scott [16], for example, provide an exhaustive theoretical and numerical treatment of the FEM. In the particular case of elliptic problems, we refer the reader to the classic

book of Ciarlet [25]. Focusing on spectral element methods, the book of Bernardi et al. [10] goes probably the deepest, opening a wide view on the theoretical implications of the issue of compatible spaces and conditions. Finally, a gradual overlapping between the two methods and an abstract approach using operator algebra is described by Schwab [113].

3.4.1 Spectral Element Methods

The spectral element method, introduced by Patera [96], is used to discretize in space the weak formulation of the governing equations. Since the temporal scheme we use decouples the solution of the conservation equations from the constitutive equation, the first of these problems is effectively a two-fields, velocity-pressure problem, with the stress known from the previous time step. Throughout the thesis M and N denote the number of elements and polynomial order, respectively. The weak formulation of the problem semi-discretized in time by means of OIFS2 is: find $\vec{u}^{n+1} \in [H^1(\Omega)]^2_D$ and $p^{n+1} \in L^2_0(\Omega)$ such that

$$\begin{aligned} \frac{3Re}{2\Delta t}\int_\Omega \vec{u}^{n+1}\cdot\vec{w}\,d\Omega + \int_\Omega \boldsymbol{\tau}^n : \nabla\vec{w}\,d\Omega - \int_\Omega (\nabla\cdot\vec{w})p^{n+1}\,d\Omega \\ = \frac{Re}{2\Delta t}\int_\Omega (4\vec{\tilde{u}}_1^{n+1} - \vec{\tilde{u}}_2^{n+1})\cdot\vec{w}, \qquad \forall\vec{w}\in W \end{aligned} \tag{3.73}$$

$$\int_\Omega (\nabla\cdot\vec{u}^{n+1})q\,d\Omega = 0, \qquad \forall q \in L^2_0(\Omega). \tag{3.74}$$

The test functions $\vec{w}$ and q are chosen in $W = \{\vec{w} \in [H^1(\Omega)]^2 \ : \vec{w} = 0 \ on \ \partial\Omega_D\}$ and $L^2_0(\Omega) = \{q \in L^2(\Omega) \ : \int_\Omega q\,d\Omega = 0\}$, respectively. To obtain a linear system, the velocity and pressure fields are approximated as described in §3.2.3. Once this process has been completed, the discretization of (3.73)-(3.74) results in a linear system in which the unknowns are the values of pressure and velocity at the nodal points on the computational grid

$$D_N u_N^{n+1} = 0, \tag{3.75}$$

$$(M_l C_N + \beta E_N)u_N^{n+1} - D_N^T p_N^{n+1} = g_N. \tag{3.76}$$

In this linear system, D_N is the discrete weak divergence operator, D_N^T is its transpose, g_N contains all the discretized nonlinear terms from the material derivative and C_N and E_N are the velocity mass and stiffness matrices, respectively. The coefficient multiplying the velocity mass matrix is given by $M_l = 3Re/(2\Delta t)$. To solve the system the symmetric Helmholtz operator $H = (M_l C_N + \beta E_N)$ has to be inverted, and this is done by means of the conjugate gradient method using the diagonal of the spectral matrix as preconditioner. Then, in order to exploit (3.75), we multiply (3.76) by $D_N H^{-1}$ and arrive at the pressure problem

$$D_N H^{-1} D_N^T p_N^{n+1} = D_N H^{-1} g_N, \tag{3.77}$$

in which the Uzawa operator is $U = D_N H^{-1} D_N^T$. The pressure is found by solving (3.77) and then the velocity is determined from (3.76). The inversion of the Uzawa operator, which is symmetric, is also performed using the conjugate gradient method, but a local finite element based preconditioner is preferred here. The Uzawa operator is in L^2 and, as such, no boundary conditions are applied directly to the pressure - boundary conditions are enforced in the velocity space [36]. A triangular finite element mesh, based on the inner GLL nodes of each spectral element, is constructed. The preconditioner is based on the finite element mass and stiffness matrices on local finite element problems, M_m^{FE} and E_m^{FE}, respectively. It reads

$$P_U^{-1} = F E_U^{-1} = \sum_{m=1}^{M} R_m^T \left(M_m^{FE} + \alpha E_m^{FE} \right)^{-1} R_m. \tag{3.78}$$

The restriction operators R_m maps a global vector to a vector of length equal to the number of inner GLL nodes of element Ω_m. The preconditioner is stored in an LU-decomposition, and inverted when needed. The choice of this preconditioner is based on the comparison of performances of a number of preconditioners carried out by Van Os [127]. The finite element based preconditioner provides an effective reduction in the number of iterations, which in the case of the Uzawa operator results in a saving by a factor of $4-6$ in the number of iterations. The coupling of this finite element based preconditioner for the Uzawa operator with the aforementioned diagonal of the spectral matrix for the Helmholtz operator provided the fastest combi-

nation in terms of CPU time required to complete a time step.

Regarding the semi-discretized constitutive equation (3.71), the solution is sought in the space of symmetric tensors of order two whose components are in $L^2(\Omega)$. We denote such a space $[L^2(\Omega)]^4_{symm}$. The polynomial order is also N, the same as the velocity. As for the momentum and mass equations, Eq. (3.71) is multiplied by a test tensor and integrated over Ω. This leads to the following weak problem: find $\boldsymbol{\tau}^n \in [L^2(\Omega)]^4_{symm}$ such that

$$\begin{aligned}\left(f^{n-1}(\boldsymbol{\tau}) + \frac{3Wi}{2\Delta t}\right) \int_\Omega \boldsymbol{\tau}^n : \boldsymbol{\sigma} - 2(1-\beta) \int_\Omega \boldsymbol{D}^n : \boldsymbol{\sigma} \\ = \frac{Wi}{2\Delta t} \int_\Omega (4\tilde{\boldsymbol{\tau}}_1 - \tilde{\boldsymbol{\tau}}_2) : \boldsymbol{\sigma} \\ - \int_\Omega E^{n-1}(\boldsymbol{\tau}, \vec{u}) : \boldsymbol{\sigma}, \qquad \forall \boldsymbol{\sigma} \in [L^2(\Omega)]^4_{symm}.\end{aligned} \tag{3.79}$$

After discretization, the resulting linear system is

$$S_N \boldsymbol{\tau}_N^n = (1-\beta) B_N^T \mathbf{u}_N^{n+1} + \mathbf{h}_N^n, \tag{3.80}$$

in which S_N is the non-symmetric discrete operator that contains all the terms on the left-hand side of the weak form of the constitutive equation and $\mathbf{h}_N^n$ is the discrete form of the right-hand side, respectively. This system is solved by means of the stabilized bi-conjugate gradient method.

3.4.2 Local Upwinding Spectral Technique

The spectral element methods are based on a Galerkin-type formulation of the differential problem; a weak form is obtained by multiplying the differential equations by test functions, and then integrating. The choice of the spaces for these function has been already discussed.

In the case of an uncoupled scheme although a free choice is available for the equation solved independently from the others. In our case this is the constitutive equation, so the test function for the stress can be freely chosen. An upwinding scheme is then used. The upwinding technique takes into account the effect of the convection not only in the the functional space

of the solutions, but also in the test space. The stress test function is then in the form

$$\boldsymbol{\sigma} - h\vec{u} \cdot \nabla \boldsymbol{\sigma}, \tag{3.81}$$

and different choices of h, the *shift factor*, lead to different upwinding methods.

A popular choice is the so called Streamline Upwind Petrov Galerkin (SUPG), which sets $h = \frac{1}{N^2}$, N being the degree of the polynomial basis. The Locally-Upwinded Spectral Technique (LUST), proposed by Owens et al. in 2002 [93], is different because calculates the shift factors h_i locally, at the element level. Within each spectral element, the GLL grid defines smaller rectangles with vertices formed by the GLL nodes x_{ij}. A generic coordinate inside the mini-element can be then identified by

$$z_{ij} = x_{ij} - h\vec{u}(x_{ij}).$$

The Lagrange interpolant

$$P_{N+1}(x) = (1-\eta^2)L'_N(\eta)(1-\xi^2)L'_N(\xi)$$

then has a zero streamline derivative inside the mini-element, and the following equality is thus satisfied:

$$P_{N+1}(z_{ij}) + Wi(\vec{u} \cdot \nabla)P_{N+1}(z_{ij}) = 0. \tag{3.82}$$

Expanding $P_{N+1}(z_{ij})$ about the corner x_{ij}, it can be found (see [93]) that for the internal nodes the shifting factor is the positive root of the quadratic equation

$$2Wi\frac{N(N+1)}{3}(\frac{u_{ij}^2}{1-\xi^2} + \frac{v_{ij}^2}{1-\eta^2})h_{ij}^2 + h_{ij} - Wi = 0. \tag{3.83}$$

We refer to [93] for the derivation of the shift factors on the edge nodes.

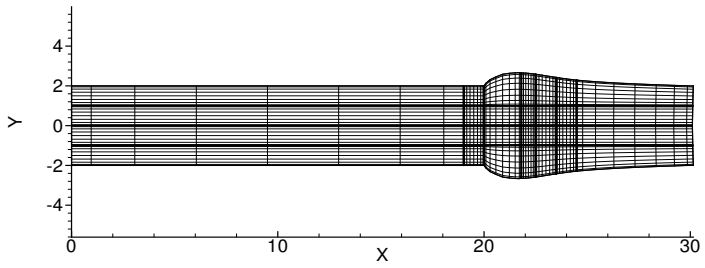

Figure 3.2: Spectral element mesh for the extrudate swell problem with $M = 28$ and $N = 8$.

3.4.3 Update of the position of the free surface

Since the Legendre polynomials are defined on the parent interval $(-1, 1)$, each physical element needs to be mapped onto the parent element $(-1, 1)^2$ and vice versa. This is also required in the fixed domain case, where the map is built for each element once and for all at the start of the computation. For moving boundary problems, the map clearly needs to be reconstructed at each time step for elements with an edge on the free surface to take into account the update of the location of the boundary. The velocity on the free surface is obtained as part of the solution process and so the test functions are chosen not to vanish there, which is similar to the treatment of fixed domain boundaries on which Neumann boundary conditions are specified. This velocity is used to move the nodal points on the free surface.

The transfinite mapping technique, introduced by Gordon and Hall [42], is a powerful method when an interior system of co-ordinates needs to be generated in a quadrilateral domain from a knowledge of a geometric description of the edges. This is perfectly suited to the spectral element method. In our case, a bilinear transfinite mapping is used:

$$\begin{aligned}\vec{F}(\xi,\eta) =& \vec{\gamma}_1(\xi)\phi_1(\eta) + \vec{\gamma}_2(\xi)\phi_2(\eta) \\ &+ \vec{\gamma}_3(\xi)\phi_2(\eta) + \vec{\gamma}_4(\xi)\phi_1(\eta) - \vec{x}_1\phi_1(\xi)\phi_2(\eta) \\ &- \vec{x}_2\phi_2(\xi)\phi_2(\eta) - \vec{x}_3\phi_2(\eta)\phi_1(\xi) - \vec{x}_4\phi_1(\xi)\phi_1(\eta).\end{aligned} \tag{3.84}$$

The vectors $\vec{x}_i,\ i = 1, \ldots, 4$, are the coordinates of the vertices, while the functions $\vec{\gamma}_i,\ i = 1, \ldots, 4$ map each edge $(x(s), y(s))$ $(-1 \leq s \leq 1)$, of the

physical element onto an edge of the parent element. In our case the components of $\vec{\gamma}_i$, which represent the transformation in the x and y directions, will be linear. Also the basis functions ϕ_i, $i = 1, 2$, are linear. The linear blending functions ϕ_i, $i = 1, 2$ are given by

$$\phi_1(\xi) = \frac{1-\xi}{2}, \quad \phi_2(\xi) = \frac{1+\xi}{2}. \tag{3.85}$$

Once the solution is found at a certain time step n, then the nodes on the edges of those elements that lie on the free surface are moved. The free surface is tracked according to three numerical schemes. A first-order scheme, a simple forward Euler formula can be used, namely,

$$\vec{X}^{n+1} - \vec{X}^n = \vec{u}^n \Delta t. \tag{3.86}$$

To achieve high order accuracy in time, two different Adams-Bashforth schemes have also been implemented. More precisely, the second and third order schemes, which read, respectively,

$$\vec{X}^{n+1} - \vec{X}^n = \frac{\Delta t}{2}\left(-3\vec{u}^n + \vec{u}^{n-1}\right) \tag{3.87}$$

and

$$\vec{X}^{n+1} - \vec{X}^n = \frac{\Delta t}{12}\left(23\vec{u}^n - 16\vec{u}^{n-1} + 5\vec{u}^{n-2}\right). \tag{3.88}$$

Remarks on the performance of these three schemes in tracking the free surface will be discussed in Section 4.4.2 for the Newtonian die swell. In the case of viscoelastic fluids, the third-order scheme is employed.

Once the position of the nodes on the free surface has been updated in a Lagrangian manner, edges of elements that lie on the free surface are reconstructed using spectral interpolation. A sample mesh at an intermediate time is shown in Fig. 3.2. The elements in the die are fixed, while elements exterior to the die and adjacent to the free surface are free to move. After the nodes on the free surface are moved, the transfinite mapping for those element adjacent to the free surface are reconstructed. As a result, the GLL nodes in these elements are also displaced. The transfinite mapping enables the mesh velocity, $\vec{v}^n$, to be computed. More precisely, if $\vec{X}_{int}^{n+1}$ and $\vec{X}_{int}^{n}$ are the vectors of the coordinates of the internal nodes constructed by means of

the transfinite mapping at the current and previous time level, respectively, then the arbitrary mesh velocity for the $i-th$ internal node is calculated as

$$\vec{v}_i^{n+1} = (\vec{X}_{int,i}^{n+1} - \vec{X}_{int,i}^{n})/\Delta t.$$

Chapter 4

Die Swell of a Newtonian Fluid: Novel Physical Interpretation and Numerical Simulations

In the introduction of this thesis we have described the importance of free and moving surface flows in real life: from testing biomaterials to the flow of biofluids, from food factories to chemical industries. There are many applications of flows with a non fixed domain, or a priori unknown domain.

The rest of this thesis is fully devoted to one of these problem which despite its harmless appearance, remains one of the most challenging in the realm of fluid dynamics. Such phenomenon is better known to the researchers as "die swell" or "extrudate swell" problem.

4.1 Introduction

Moving and free surface flows are pervasive in both nature and industry: flows in the human body, and problems in oceanography, dam problems, chemical industry, food processing industry are only a few examples of ap-

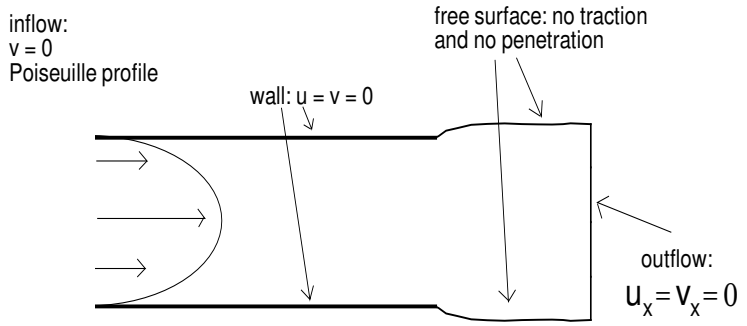

Figure 4.1: Fluid jet from a die.

plications requiring good numerical predictions. The so-called die swell phenomenon is particularly common in industries where fluids are extruded from dies. Bread dough, concrete, molten polymers, ink are some of these fluids. The most important and relevant swelling phenomena in real life, such as the ones mentioned above, are related to viscoelastic fluids, which we will analyze in the next chapter.

When a fluid leaves a die a relaxation process due to the absence of rigid walls occurs. As a consequence of this process the fluid swells. The ratio between the diameter of the fluid downstream when relaxation is complete and the diameter of the die is called the swelling ratio. This quantity, together with the normal stress jump at the exit of the die and the tracking of the free surface outside the die are the key points to understand and to analyze in this problem. A sketch of the die swell phenomenon is depicted in Fig. 4.1.

The literature on the Newtonian die swell problem is not extensive, and mainly focuses on the axisymmetric case. The general trend in the development of numerical methods for this problem has been to test the method on the Newtonian case and then to move forward to the viscoelastic problem.

The latter is certainly of higher interest for industrial purposes, and, perhaps for this reason, the Newtonian die swell has not been fully understood. As we have mentioned already, the main causes of viscoelastic swelling are the normal stresses and the normal stress differences, together with the pressure drop at the exit. It is widely accepted that the swelling ratio is proportional to these quantities, and a few empirical equations have been proposed (see, for instance, the data interpretation from Liang [68] and references therein). From the analysis of Huang and Lu [54], the relaxation properties of the fluid also appear to be quite relevant. In the Newtonian case, the normal stresses and the first normal stress difference increase with Reynolds number; but at the same time by increasing inertia the swelling decreases, causing the extrudate to eventually contract for Reynolds numbers that are sufficiently high. The first experimental evidence of die swell for a Newtonian fluid is attributed to Middleman and Gavis [84], who reported decreased swelling with increasing Reynolds numbers up to $Re = 16$. At higher Reynolds numbers the extrudate contracted after exiting the die. This tells us that the mechanism behind the Newtonian die swell is unrelated to the viscoelastic analogue. Therefore, a deep analysis of the extrusion of a Newtonian fluid is needed in its own right and can provide an important insight into the underlying physics. The aim of the first part of this chapter is to give a complete and detailed physical description of the die swell problem for a Newtonian fluid, aided by high order numerical simulations in the planar case. In the case of Newtonian fluids, the cause of the swelling is only the reorganization of the velocity field from the fully developed Poiseuille profile within the die to a completely relaxed plug flow far enough downstream from the exit. This has been mentioned for instance by Jay et al. [59] in their simulations of extrusion with slip conditions, with reference to the work of Tanner [118], but the ideas presented in [118], as pointed out by Tanner himself, only predict changes from the Newtonian case. In fact, the equation Tanner derives and uses to describe the swelling of second order and Maxwell fluids predicts no swelling in the Newtonian case.

Between thirty and forty years ago, considerable effort was devoted to studying the die-swell phenomenon. As powerful computers became readily avail-

able, numerical simulations were performed, which then called for a deeper physical interpretation. In the early sixties, Metzner et al. [82] used experimental measurements of the swelling ratio to calculate the first normal stress difference in a Poiseuille flow. In order to determine the normal stresses, they derived a formula from the balance of momentum in the portion of fluid between the exit and the downstream relaxation region, where the fluid profile has a constant diameter. They assumed that the flow downstream has no effect on the profile in the die. Although acceptable, this is not totally correct, as we observe in our simulations. In fact, even when inertia is discarded, a change in the velocity field still takes place just before the exit, as was predicted by Horsfall [53], who solved a creeping flow problem by approximating the equations for the stream function with a finite difference scheme.

An early comparison between Newtonian and viscoelastic die swell was performed by Batchelor et al. [7], who found that, for the natural rubber Lorival R25, the swelling ratio increased significantly with increasing shear rate, while for the Newtonian Paralac 385 it did not. This observation has been confirmed widely, highlighting the distinction between the viscous and elastic effects on the die swell phenomenon.

Early finite element simulations were performed by Nickell et al. [86] to confirm the 13.5% swelling in the axisymmetric geometry. They drew attention to a change in the axial normal stress at the exit plane from tensile close to the wall to compressive near the centre line. Although they understood the relevance of this transition, they did not investigate it further. In the same paper, the evidence of swelling in creeping flow is also supported in contrast to Richardson [105], who argued that die swell is a phenomenon strictly linked to inertia. Unaware of simulations or experiments for Reynolds numbers below the value of 2, Richardson reasonably argued that, by increasing inertia, the fluid tends not to depart from its motion, this being the reason for less swelling; the lower the inertia, the higher the tendency of the fluid to fill all the possible space by swelling. He extrapolated this argument to suggest that it is not possible for creeping flow to swell at all, an hypothesis which proved to be incorrect. Ho and Patera [50] obtained agreement with

the result from Nickell et al. [86], predicting a 13.26% increase for the same geometry and an 18.4% increase for the planar case. Their simulations, as far as we are aware are the only ones that have been performed for the plane Newtonian die swell problem using spectral elements so far.

As part of a viscoelastic die swell analysis, Chang et al. [23] compared collocation and Galerkin finite element methods and reported quite similar performances for the Newtonian axysimmetric problem, while the collocation approach appeared to be superior in the case of a Maxwell fluid. This difference has not been reported in other work that considered the same configuration, such as Reddy and Tanner [102]. The latter authors used second order fluids though, which led Chang et al. [23] to believe that the problem was in the choice of the model rather than in the choice of numerical scheme.

Mitsoulis [85] simulated a three dimensional jet by finite elements reporting a maximum 19% swelling in the $2-D$ central section of his domain, which would be the closest approximation to the planar, two-dimensional limit. Swelling was then reduced to 4% at the corners of the square cross-section.

A systematic numerical study of the Newtonian die swell has been performed by Omodei, both in the axisymmetric [91] and planar [92] cases. The effects of inertia and surface tension have been carefully analyzed, the shapes of different free surfaces have been investigated and checks on the satisfaction of boundary conditions have been performed. Omodei used a Galerkin finite element method to solve the governing equations and cubic splines to interpolate the free surface. Georgiou and Boudouvis [38] analyzed both planar and axisymmetric problems comparing standard and singular finite element methods. The effects of inertia and surface tension are investigated, and the authors find standard FEM performing better than singular FEM when the Reynolds number increases and capillary numbers decreases. Therefore the authors suggest that the flow is less affected by the stress singularity at the exit for increasing inertia and surface tension. However, in their simulations the fluid starts contracting for $Re \simeq 7$ (see Fig. 4 in [38]), which is less then half the value reported by Middleman and Gavis [84]. Russo and Phillips

[111] also focused on the validation of their numerical scheme based on the spectral element method in a recent paper. The simulations reported in that paper are accurate and in good agreement with previous work [92, 119].

In conclusion, it seems that the numerical simulation of the die-swell phenomenon has focused so far on the performance of the numerical schemes, without providing a convincing explanation of the decreasing swelling ratios with increasing inertia. Tanner [119, 118] highlights the different region of tensile and compressive stress, but there is no evidence of how such regions, and the correlated stresses, change with inertia. In fact, for the isothermal Newtonian case, the idea of Tanner simply does not apply, because no change in viscosity occurs between the compressive and tensile stress regions. Moreover, neither has a full explanation been given to the contraction process at large Reynolds number reported by Middleman and Gavis [84], nor has an attempt been made to investigate the critical swelling Reynolds number based on the stress balance. These are the gaps we try to fill in Section 4.3, also investigating the role of the surface tension. The encouraging numerical results in Russo and Phillips [111], which are the main subject of Section 4.4, support the physical interpretation of the die swell phenomenon presented in the present chapter, which starts with an overview of the role of the stress singularity at the exit in the die-swell problem. A detailed analysis of such an issue is outside the scope of this thesis. However we believe it is too important to be left out.

4.2 Stress singularity at the exit in die-swell: an overview

The stress singularity at the exit of the die in the die-swell problem is a particular type flow near a sharp corner. It is one of the cases where the corner points into the flow, this being the reason behind the singularity.

In general, the assumption is made that the stream function for the problem

can be expressed as

$$\psi = r^m f_m(\theta). \tag{4.1}$$

In the case of Stokes flow, the stream function satisfies the bi-harmonic equation $\nabla^4\psi = 0$. Therefore, a general solution is

$$f_m(\theta) = A_1 \cos m\theta + A_2 \sin m\theta + A_3 \cos(m-2)\theta + A_4 \sin(m-2)\theta. \tag{4.2}$$

The angle α of separation in this case is also an unknown quantity. The contrast between the theoretical prediction of Michael [83], who report separation at $\alpha = \pi$, and the experiments suggests further research is needed. In the case of $\alpha = \pi$, the exponent is real and has a minimum value of $m = 3/2$. As a consequence, the stresses behave like $r^{-1/2}$ near the separation point.

In the case of power-law fluids, the stress behaves approximately like $r^{-n/(n+1)}$, while the second-order model shows a non-integrable behaviour for the stress, namely r^{-1}.

For viscoelastic fluids, the Oldroyd-B case was analyzed by Hinch [49] for $\alpha = 3\pi/4$. He proved the assumption that the convective derivatives of stress and rate of strain in the constitutive equation dominate to be wrong. Therefore, it does not seem plausible to associate the Oldroyd-B fluid behavior to a Newtonian fluid with an effective viscosity of $\beta\eta$, where β and η are the viscosity ratio and solvent viscosity, respectively. Hinch [49] considered instead a core region where the alternative limit case, namely a vanishing upper convective derivative, occurs. The consequent result is that the stress behaves like

$$\sigma_{ij} \sim r^{-2(1-\pi/\alpha)}. \tag{4.3}$$

From Eq. (4.3) one realizes that the limiting cases are $\alpha = \pi$, with a corresponding regular solution, and $\alpha = 2\pi$ with a corresponding non-integrable solution. For $\pi \leq \alpha \leq 2\pi$ the stress is singular and integrable. These results

have been confirmed by Renardy [104], who matched upstream and corner flows for $\alpha = 3\pi/4$.

As far as numerical results near singular points are concerned, Richardson [106] pioneered the investigation on the Newtonian stick-slip problem more than twenty years earlier than the study of Tanner and Huang [121], which would have shown the exact form and strength of the singularity. The numerical results from Richardson underestimated the strength of the singularity, while better agreement with theory was obtained by Salamon et al. [112], who used FEM based on extremely fine meshes.

The viscoelastic stick-slip problem is much more difficult. No results are provided by either Hinch [49] or Renardy [104] for the slip-stick case in the case of an UCM fluid. Therefore, for the sake of comparison, Tanner [119] reports on computations with $\alpha = 3\pi/4$. A reasonable agreement with the results in Renardy [104] is found with the stress behaving like $r^{-2/3}$, and velocity like ($\sim r^{2/3}$). Moreover, in the case of an affine PTT fluid there seems to be a very small, roughly Newtonian region [119] near the stick-slip point.

4.3 Physical interpretation of die swell

Throughout the whole chapter, we adopt the following choice of the parameters:

$$L = 1.0\ m; \qquad d = 0.4\ m; \qquad \rho = 1.0 kg/m^3; \qquad U = 1.0 m/s.$$

The Reynolds number scales as the inverse of the viscosity and the Weber number as the inverse of the surface tension parameter σ. In fact, for the above choice of parameters, $Re = \frac{1}{\mu}$ and $We = \frac{1}{\sigma}$. As we have already remarked, most of the previous work on the Newtonian die swell problem simply treated the problem as a stepping stone to reach the corresponding viscoelastic problem. A complete physical explanation of the phenomenon has yet to be provided.

In the viscoelastic case, it is accepted that the swelling ratio is proportional to the normal stresses and normal stress differences [117]. A few equations have been proposed (see for instance the data interpretation from Liang [68] and the references therein) relating these quantities. In Table 4.1, we simply highlight that this explanation is not valid in the Newtonian case. Although the computed axial normal stress at the exit increases with increasing Re, there is not a corresponding increase in the swelling ratio. In fact, the opposite trend is observed, and the swelling ratio decreases. Moreover, the first normal stress difference for a Newtonian fluid is zero.

For a Newtonian fluid, the swelling beyond the exit of the die must be attributable to the transition from Poiseuille flow in the die to a uniform or plug flow far enough downstream. We define a **region of transition** to be the region between the die exit and the downstream cross-section at which a plug flow and an extrudate of constant diameter is formed. Such a transition is caused physically purely by the sudden jump in the shear stress. This attains its maximum value, in modulus, at the wall in the die, because it has to stick the particles to the rigid surface where no slip is applied, whereas on the free surface it is zero. Immediately, after the exit, the particles close to the wall are then, in some way, finally free to move when the fluid leaves the die, resulting in an almost instantaneous acceleration.

The horizontal velocity profiles at different cross sections are shown in Fig. 4.2. The exit plane corresponds to $x = 10$. The difference between the first two curves confirms that the flow just before the exit is influenced by the whole flow field, as was noticed by Horsfall [53].

4.3.1 Conservation of energy and downstream velocity prediction

It can also be seen in Fig. 4.2 that, in the core of the fluid, the fluid particles decelerate and the axial and radial normal stresses change sign. This is illustrated in Figs. 4.3 and 4.4. We define the **outer layer** to be the region where the particles accelerate in the axial direction and $\tau_{xx} > 0$[1].

[1] In this chapter, we denote with the tensor $\boldsymbol{\tau}$, whose components are τ_{xx}, τ_{xy} and τ_{yy}, the extra-stress tensor introduced in Chapter 2, Eq. (2.22). In fact it is equivalent to $\boldsymbol{T}$.

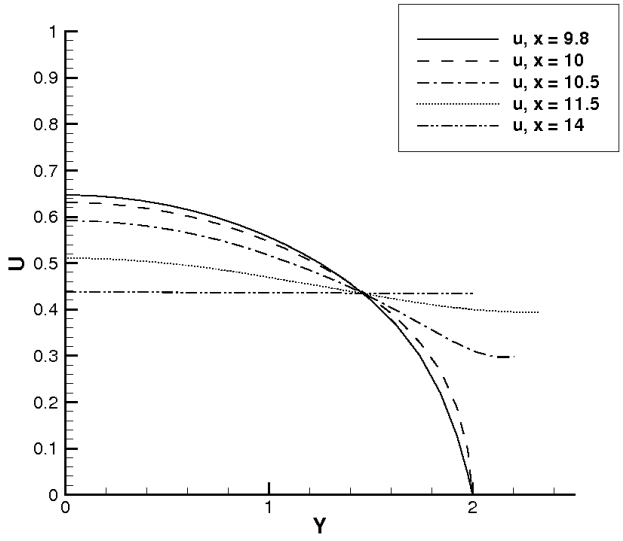

Figure 4.2: Horizontal velocity profiles at different locations inside and outside the die. The solid curve is just before the exit.

Conversely, we define the **core layer** to be the region where the axial velocity of the particles decrease.

One could argue that, as a consequence of the acceleration of particles in the outer layer, the plug flow profile should be uniform with the velocity assuming its value at the centreline; namely, the maximum velocity u_{max}. This is clearly not what is observed, and the reason for this can be explained by the conservation of energy. In the region of transition there is no gain or loss of energy since gravity is neglected, there is no friction on rigid boundaries and there are no other external forces. This means that the total flow rate at any cross-section in the die has to be the same as at any cross-section of the plug flow.

For viscoelastic fluids instead, namely throughout the rest of the thesis, $\boldsymbol{\tau}$ represents the polymeric extra-stress tensor, so that $\boldsymbol{T} = 2\eta_s \boldsymbol{d} + \boldsymbol{\tau}$.

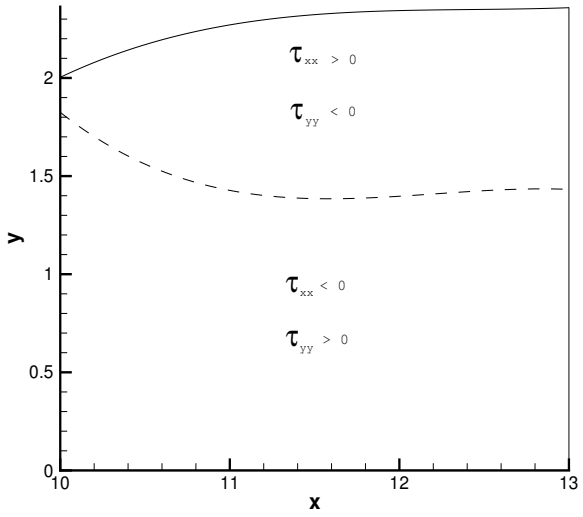

Figure 4.3: The core and the outer stress regions downstream of the exit of the die. The exit is at the origin of the axis, $x = 10$.

The flow rate at any cross-section in the die is

$$Q_{die} = \int_{-h}^{h} u(y)\, dy = \int_{-h}^{h} \frac{h^2}{2\mu}\Big(- \frac{\triangle p}{\triangle x}\Big)\Big[1 - \Big(\frac{y}{h}\Big)^2\Big], \tag{4.4}$$

where h is the die radius and $(-\frac{\triangle p}{\triangle x})$ is the pressure gradient driving the flow. In the same fashion, taking into account that the plug velocity u_{plug} is constant, we can express the flow rate downstream as

$$Q_{plug} = 2h_{plug}u_{plug}, \tag{4.5}$$

where h_{plug} is the radius of the plug. If $u_{plug} = u_{max}$ it is trivial to show using (4.4) and (4.5) that $Q_{plug} > Q_{die}$, which is not allowed. On the other hand $u_{plug} > 0$, so this explains why the velocity downstream achieves a value $0 < u_{plug} < u_{max}$. This implies that the particles in the core region of the fluid do decelerate in the region of transition.

If the final diameter h_{plug} is known, equations (4.4) and (4.5) provide a

means of predicting the downstream plug velocity. It is simply calculated as

$$u_{plug} = \frac{Q_{die}}{2h_{plug}}. \tag{4.6}$$

A comparison of the plug velocities predicted by this formula and the ones obtained by numerical simulations is given in Table 4.2 for different flow parameters. The column u_{plug}^{pred} has the values predicted by the flow rate balance (4.6) and the values u_{plug}^{sim} are the results from the simulations. It is clear, from this table, that the approximation improves with the approximation order of polynomial and is more accurate at lower Reynolds numbers. In this table, SR is the swelling ratio used to determine the final diameter h_{plug}.

The formula we used to compute Q_{die} - and hence u_{plug}^{pred} in (4.6) - is actually written in terms of the maximum velocity on the centreline of the die:

$$Q_{die} = \frac{2}{3} u_{max}(2h). \tag{4.7}$$

The reason is that, even though in reality the pressure gradient drives the flow, initial conditions are required for the velocity rather than the pressure in the numerical simulations. This means that the value of the pressure gradient $-\frac{\triangle p}{\triangle x}$ is computed at the end of the simulation. Thus, if we want to apply (4.4), we would be using a quantity that is already affected by some numerical error. On the other hand, the inlet boundary condition is exact at the inflow boundary, and so is the maximum velocity which appears in (4.7). The outer and the core layers are then identified by the regions with accelerating and decelerating flow, respectively, in the axial direction, or, in other words, by the tensile and compressive stresses, respectively. The situation is depicted in Fig. 4.3: the acceleration of the particles close to the wall in the $x-$direction results in $\tau_{xx} > 0$; therefore, a negative τ_{yy} is a consequence of (2.20). We remark that, for Newtonian fluids, the continuity equation is equivalent to the condition $tr(\boldsymbol{\tau}) = 0$. As just pointed out, the normal stresses change sign in the core region. There are no other forces involved. We therefore believe that it is the resultant of these competing stresses that is the only cause of the swelling or shrinking of the fluid out-

Re	Computed normal stress at the exit	Computed swelling ratio
1	13.048	1.1998
3	15.636	1.1710
6	22.339	1.1503
8	28.889	1.1182
10	40.001	1.0844

Table 4.1: Dependence of axial normal stress at exit and swelling ratio on Reynolds number.

u_{max}	Re	SR	u_{plug}^{pred}	u_{plug}^{sim}(% err) $N = 8$	u_{plug}^{sim}(% err) $N = 12$	u_{plug}^{sim}(% err) $N = 16$
0.75	1	1.9998	0.4201	0.4338 (3.19%)	0.4203 (0.03%)	0.4204 (0.03%)
2.25	3	1.1347	1.3219	1.3008 (1.59%)	1.3133 (0.65%)	1.3173 (0.35%)
4.5	6	1.1131	2.6915	2.6016 (3.46%)	2.6891 (0.35%)	2.6927 (0.04%)
6.0	8	1.1006	3.6343	3.4688 (4.55%)	3.6171 (0.74%)	3.6245 (0.27%)
7.5	10	1.0844	4.6108	4.3336 (6.01%)	4.5544 (1.22%)	4.5727 (0.83%)

Table 4.2: Comparison of the predicted and approximated values of the plug velocities.

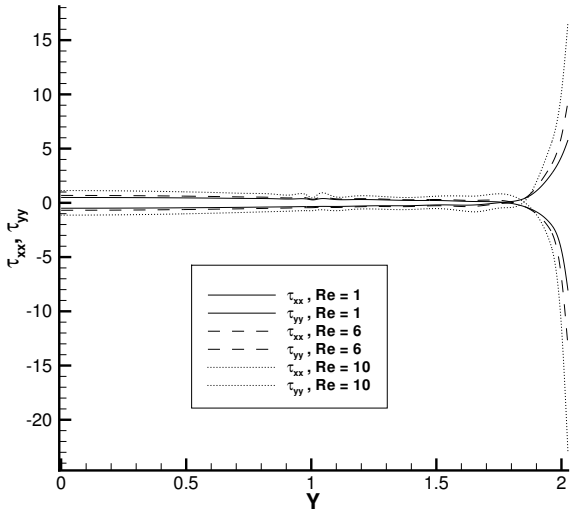

Figure 4.4: Dependence of the normal stress profiles at the exit on the Reynolds number.

side the die. The outer layer tries to push down the core and vice-versa. Swelling takes place as long as the total force from the core is larger than the force exerted by the outer layer; otherwise the fluid shrinks. In Section 4.4, numerical simulations are presented that confirm this hypothesis.

4.3.2 Variations in inertia and surface tension

It is well known that increasing inertia reduces swelling. There is also a fair amount of evidence to support this statement. For instance, the work of Russo and Phillips [111] confirmed predictions of Omodei [92] obtained in the late seventies for a range of Reynolds numbers.

Again, the physical reason behind this is the balance of stresses between the core and the outer layer. The fluid exhibits swelling up to a certain value of the Reynolds number, which we call the **critical swelling Reynolds number** and denote $Re_{cr,sw}$. This value, according to the first experiments of Middleman and Gavis [84], is around 16, whereas Omodei [92] predicted a value around 18.

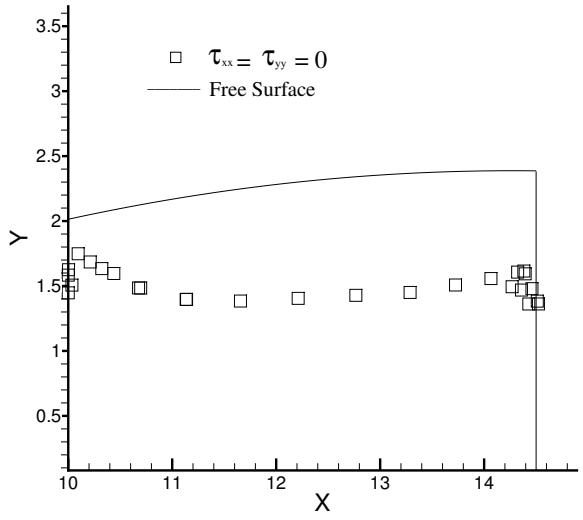

Figure 4.5: The curve along which $\tau_{xx} = \tau_{yy} = 0$.

The curves highlighting the different regions of tensile and compressive stress are shown in Fig. 4.4 for different values of Re. The first component of the normal stress, τ_{xx}, is negative along a large part of cross-section at the exit and it becomes positive around $y = 1.75$. The second component, according to the continuity equation, is simply $-\tau_{xx}$. This change of sign in the normal stress components marks a switch from compressive to tensile stress. We also show in Fig. 4.5 a snapshot, for $Re = 1$, of the region of transition. Here the line along which the normal stresses change sign has been computed numerically, and it is represented by the square symbols. In this picture it is also clear that the continuity equation is not violated since both τ_{xx} and τ_{yy} change sign at the same point. It is clear from both Fig. 4.4 and Fig. 4.5 that the core layer is broader than the outer layer. Actually, in Table 4.3 it can be seen that the core layer accounts for about twice the area of the outer region, almost independently of the Reynolds number.

What is also clear is that the difference between the values of the stress is much greater in the outer layer than in the core, due to the presence of

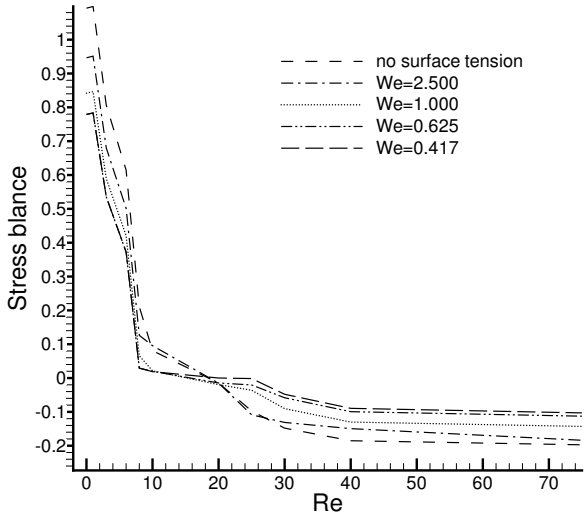

Figure 4.6: Dependence of the difference between the forces in the core and outer regions on Re for different values of Weber number.

the singularity at the exit. Therefore, the force pushing the fluid to swell is smaller but acting on a larger portion of fluid, namely the core layer whereas the force attempting to shrink the fluid is much higher but acting on a smaller portion of fluid. When inertia increases, the stress acting on the outer layer increases much more than its counterpart in the core; from $Re = 1$ to $Re = 10$ the stress on the centreline barely rises above 1, while the tensile stress jumps from roughly 5 to about 15. Furthermore, as we report in Table 4.3, the size of the core layer stays the same. Thus, by increasing inertia the tensile region gradually closes the gap and eventually dominates, forcing the fluid to contract.

In order to have a quantitative idea of this balance, we performed some simulations for a range of values of Re and We and numerically integrated the values of the stress over the surface. The outcome is shown in Fig. 4.6. Although such a calculation is not aimed to exactly quantify the critical swelling Reynolds number, and being conscious of the errors in the numerical approximation, this graph is still significant. The resultant of these forces

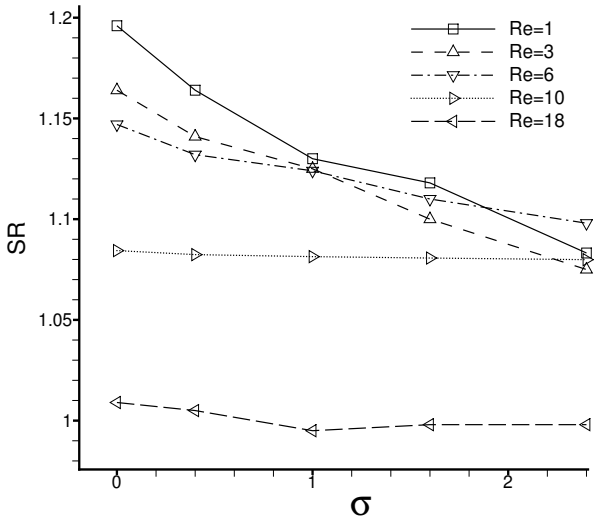

Figure 4.7: Influence of surface tension on the swelling ratio for different values of Re.

decreases with increasing Reynolds number. A positive resultant, according to our interpretation, means that the fluid expands beyond the die. This is because the force in the outer layer, F_O, is less than the force in core layer, F_C. The opposite happens when the resultant is negative. Moreover, the presence of surface tension aids the force in the outer layer for $Re < Rr_{cr,sw}$, whereas the contrary happens for $Re < Rr_{cr,sw}$. In this perspective, we notice how this increase in F_O decreases with increasing We. In fact, as shown in Fig. 4.7, and as also reported by Omodei (see Table 1 in [92]) , the values of the swelling ratios are effectively independent on We when $Re \sim Rr_{cr,sw}$. This happens because, if surface tension is assumed at the liquid/air interface, there will be an active driving force which tries to minimize the curvature of the free surface and which acts in the same direction as F_O. Since such a curvature decreases with increasing Reynolds number, the driving force will decrease as well, altering F_O less and less until F_O will not be affected anymore for $Re \sim Rr_{cr,sw}$. This idea finds full confirmation in the formula for predicting the swelling ratio reported by Omodei (see Eq.

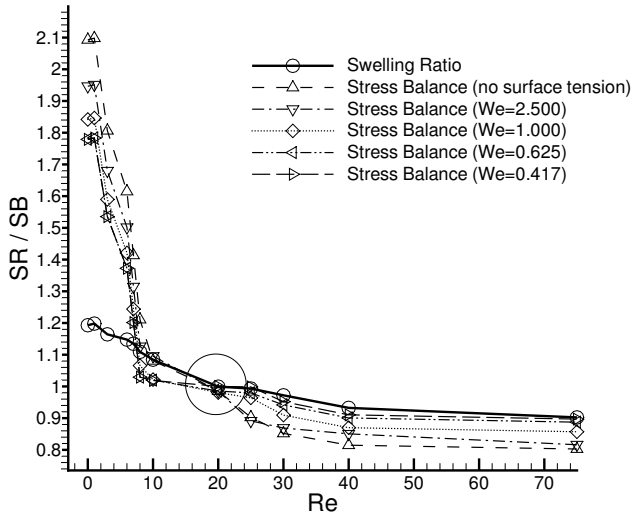

Figure 4.8: Swelling ratio and resultant of forces plotted against Re for different We..

5.2 in [92]). In such a formula, the surface tension parameter is scaled by a factor which decreases with decreasing curvature. In fact, such a factor vanishes for zero curvature, resulting in a null contribution from the surface tension, even if the latter is assumed in the problem at the liquid/air interface.

An attempt at quantitative prediction is shown in Fig. 4.8, for mere reasons of visualization, the curve representing the resultant of forces has been shifted vertically one unit. The graph suggests that the swelling ratio drops below 1 roughly when the resultant force falls below 0. This tells us that for $Re \simeq 20$ the direction of the resultant is reversed due to a sufficiently high normal stress in the tensile region, which causes the fluid to contract after the die exit.

Another relevant effect which occurs on increasing inertia is the vertical velocity overshoot just before the exit. In Fig. 4.2 we showed the profiles of the horizontal component of velocity at different cross sections, with the exit

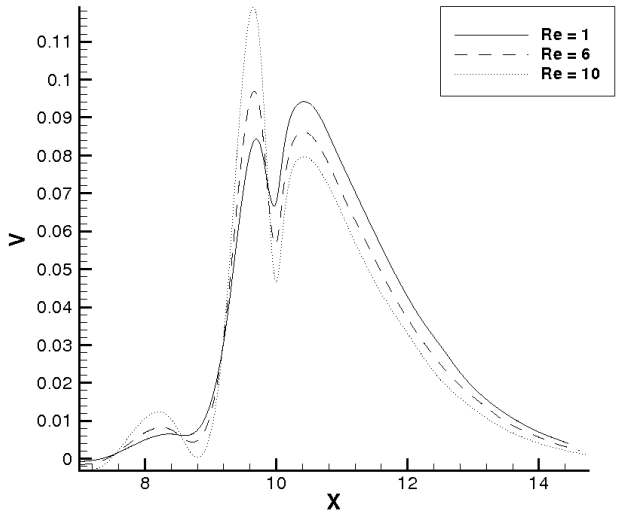

Figure 4.9: Vertical velocity overshoots along the line $y = 1.6$. The die exit is at $x = 10$.

located at $x = 10$. Thus the difference between $x = 9.8$ and $x = 10$ means that the flow at the end of the die is affected by the flow in the transition region. This was observed by Horsfall [53] in his simulations. We investigate this further, and in Fig. 4.9 the overshoots in the vertical component of velocity around the exit are shown. This plot is along the line $y = 1.6$, which is the point in the cross-section at the exit where the vertical velocity component is maximum. As inertia increases, so does the peak in the vertical velocity component just before the exit.

Once again this can be explained by the sudden change in the horizontal velocity of particles in the different layers. The particles in the core and outer layers decelerate and accelerate in the axial direction, respectively. The outer layer is then a region of high extensional flow. An extreme but significant comparison is an entry flow. The cross section at the entry includes a vertical wall, which clearly causes the particles to decelerate. In the die swell configuration, the counterpart is the core region in the cross-section

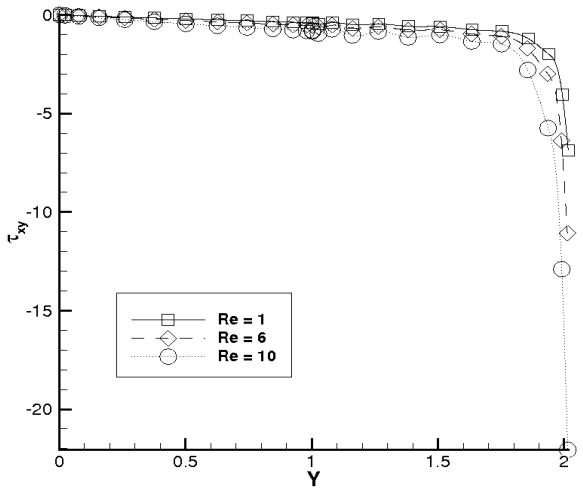

Figure 4.10: Shear stress along the cross section at the die exit for different values of Re .

at the exit. On the other hand, in the entry part of the cross-section in a contraction geometry, namely, where the smaller channel begins, the particles accelerate, experiencing an extensional flow. In the die swell problem, the region where the flow is extensional can be represented by the outer layer of fluid beyond the exit.

In the die swell problem, increasing inertia results in a larger jump in the shear stress τ_{xy} at the exit as shown in Fig. 4.10. This causes an increase in the acceleration of the particles in the outer layer in the axial direction and hence larger overshoots in τ_{xx}, as shown in Fig. 4.4. In this way the extensional effect in the outer layer increases. Similarly, to increase the extensional nature of the flow at the entry region in a contraction problem, where the width of the channel suddenly decreases, a higher contraction ratio is required. The vertical velocity overshoots are then shown in Fig. 4.11 for two different contraction geometries. Fig. 4.11 can be also compared with Fig. 4.9, where the peaks in the value of the vertical velocity increase with increasing inertia. This is obviously a purely qualitative comparison. The point we wish to make here is that, in the transition region of the ex-

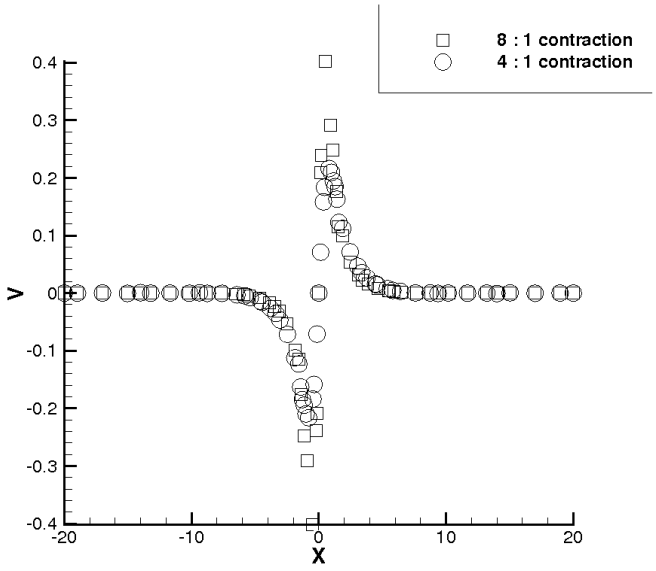

Figure 4.11: Vertical velocity overshoots on the centreline around the contraction region.

trusion flow, the outer layer of fluid suddenly goes into extension, while the core tends to decelerate. This can definitely be compared to an entry flow in terms of the physical nature of flow regions; and indeed the two phenomena show the same features with respect to the vertical velocity overshoots.

Therefore, we believe that, by means of our interpretation, the region of transition in the extrusion flow can be compared with an entry flow. This would explain why, in the die swell problem, the overshoots in vertical velocity just before the exit increase with inertia; and for the same reason, why in the entry flow problem the peaks in the vertical velocity increase just before the contraction region at higher contraction ratios in the entry flow.

Re	Core layer region (%)
1	64.7783
3	64.8243
6	64.8333
8	64.9476
10	65.0127

Table 4.3: Dependence of the percentage of fluid in the core region on the Reynolds number.

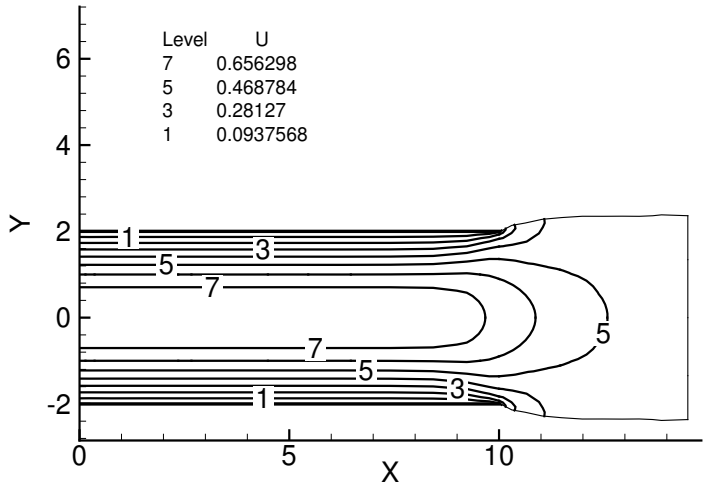

Figure 4.12: Horizontal velocity contours for $Re = 1$, $M = 4$, $N = 12$, with surface tension neglected.

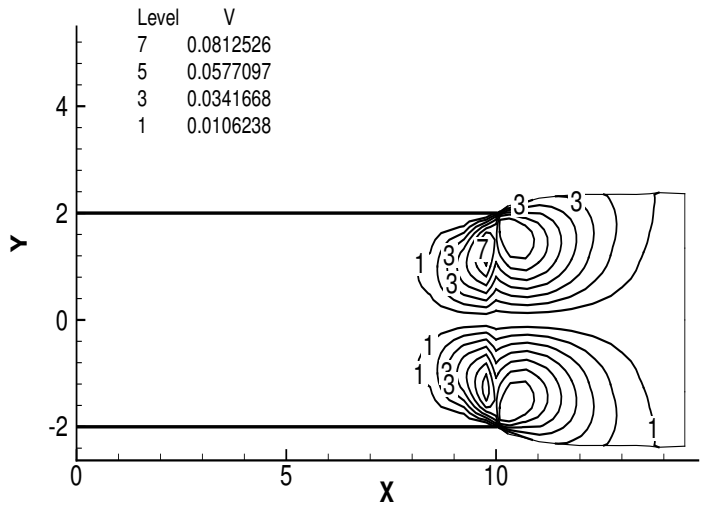

Figure 4.13: Vertical velocity contours for $Re = 1$, $M = 4$, $N = 12$, with surface tension neglected.

4.4 Numerical simulations

In this section, the numerical algorithm described in Chapter 3 is used to perform accurate simulations of the plane die swell of a Newtonian fluid. In particular, all the characteristic features of this problem are reproduced. These features are a consequence of the stress balance effect fully explained in this chapter.

To verify the general features of the die swell problem, the velocity and stress contours for $Re = 1$ are shown in Figs. 4.12-4.15. It can be seen that the horizontal component of velocity approaches a constant value downstream and that the vertical component increases instantaneously just after the exit before relaxing downstream. Streamlines shown in the next section help to clarify the picture. The shear stress contours shown in Fig. 4.14 are in very good agreement with those reported by Tanner [119]. The stress has a singularity at the point $x = L$, $y = R$, where for the problem considered $L = 10$ and $R = 2$.

The shear flow in the die and the plug flow downstream mean that the

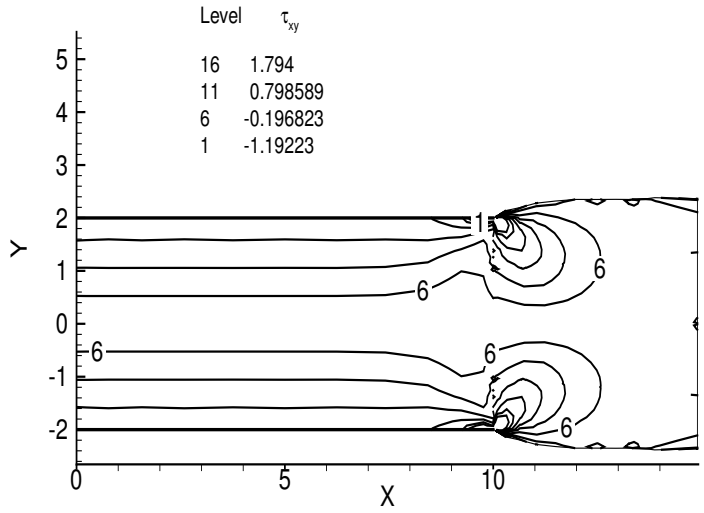

Figure 4.14: Shear stress contours for $Re = 1$, $M = 4$, $N = 12$.

normal stresses τ_{xx} and τ_{yy} are zero everywhere apart from around the exit. The discontinuity in stress at the die exit is physical, and it seems to be quite well reproduced. We have followed the idea of Gerritsma and Phillips [39] and allowed the stress approximation to be discontinuous across elements. On the other hand, the velocity components are enforced to be continuous across elements.

4.4.1 Boundary conditions

In this section we check that the boundary conditions which are not imposed a priori are satisfied in our simulations. On the free surface all the stress components have to vanish. The axial normal stress is shown in Fig. 4.16 for $Re = 1$ and $N = 12$. Here surface tension was neglected. For $0 < x < 10$ it is also zero on the wall; then the discontinuity is evident at the exit, where a discontinuous approximation proposed by Gerritsma and Phillips [39] is used across elements.

Similar behaviour is shown by the shear stress in Fig. 4.17, with the difference that on the wall its value is the constant given by the Poiseuille flow in

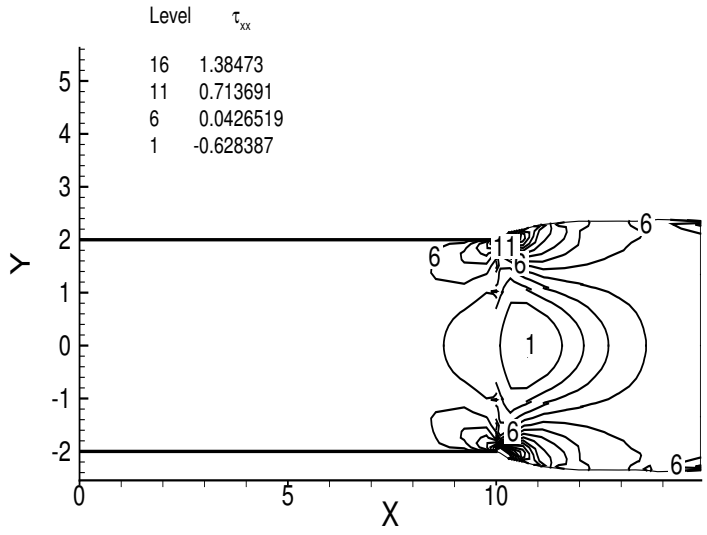

Figure 4.15: Axial normal stress contours for $Re = 1$, $M = 4$, $N = 12$.

the die. Finally, when steady state is achieved, the normal velocity has to be zero on the free surface for the no penetration condition to be satisfied. The L^2-norm of velocity is plotted in Fig. 4.18 against time. This figure shows that this condition is satisfied when steady state is attained.

4.4.2 Analysis of convergence

In this section we discuss the spatial and temporal convergence properties of the numerical scheme presented in this thesis. Concerning the spatial convergence, we focus on the convergence of the location of the free surface and the horizontal velocity profiles at various cross-sections in the interior of the flow domain. First, a mesh convergence study of the location of the free surface as a function of the polynomial order is performed. This is shown in Fig. 4.19. The location of the free surface clearly converges as the order of the polynomial approximation is increased. A spectral approximation with $N = 10$ is sufficient to provide a converged position of the free surface independent of the temporal scheme used.

The velocity profiles are then plotted at different channel cross-sections. The die exit in our simulations is located at $x = 10$. In Fig. 4.20, the

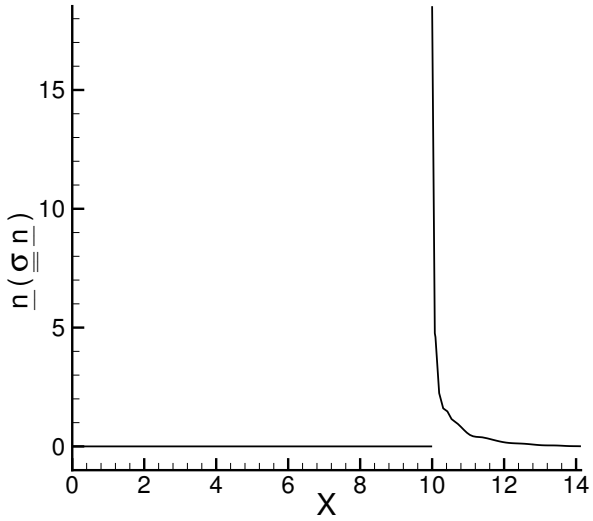

Figure 4.16: Axial normal stress profile on the free surface.

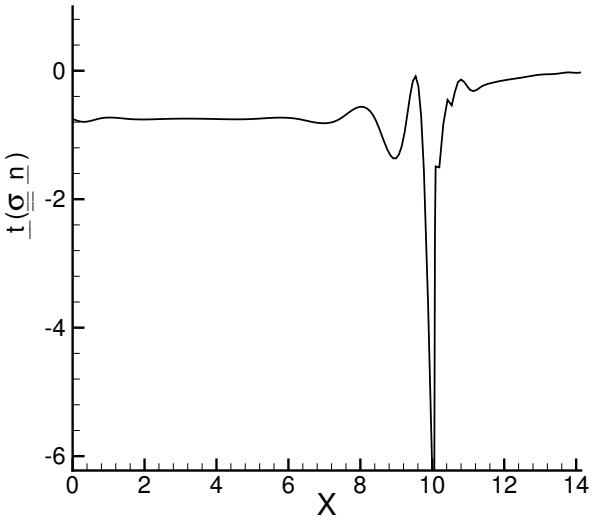

Figure 4.17: Shear stress profile on the free surface.

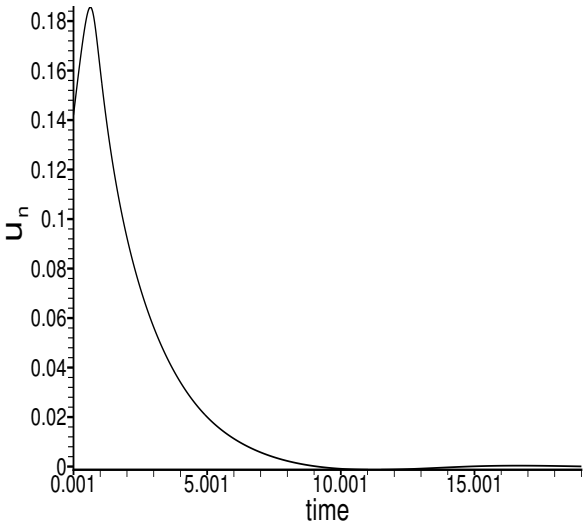

Figure 4.18: L^2-norm of the normal velocity on the free surface against time.

profiles at $x = 8$ and $x = 10.2$ are plotted as a function of polynomial order. The profiles for $N = 10$ and $N = 12$ are in close agreement for both cross-section locations. Further downstream, the profiles tend towards a profile characteristic of plug flow. This is shown in Fig. 4.21, where the convergence with respect to the number of elements is investigated at $x = 12.6$ and $x = 14$. For this particular problem, a small number of spectral elements, $M = 4$, coupled with a polynomial approximation of order $N = 12$, is sufficient to obtain a converged approximation to the solution of this flow problem.

The OIFS scheme, which was described in §3.3, has been used for the temporal approximation of the momentum equation. Both the first and second order variants of this scheme have been employed in the simulations. The position of the free surface is tracked using the Adams-Bashforth methods of order k, for $k = 1, 2, 3$. The first-order Adams-Bashforth method is just the forward Euler method. The Adams-Bashforth method of order three is conditionally stable. The time-dependance of the relative errors in the extra-stress and velocity approximations are shown in Fig. 4.22 for

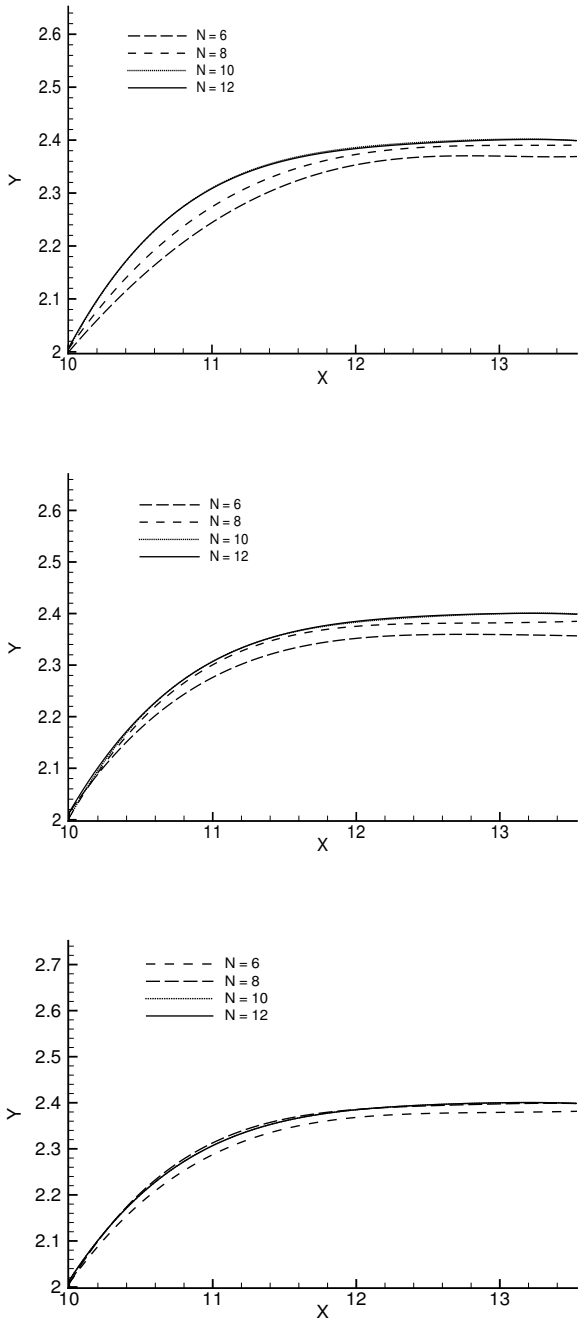

Figure 4.19: Location of the free surface for different values of N using different temporal schemes for the update of the location of the free surface. Forward Euler (top), AB2 (middle), AB3 (bottom). $\Delta t = 10^{-3}$, $M = 4$.

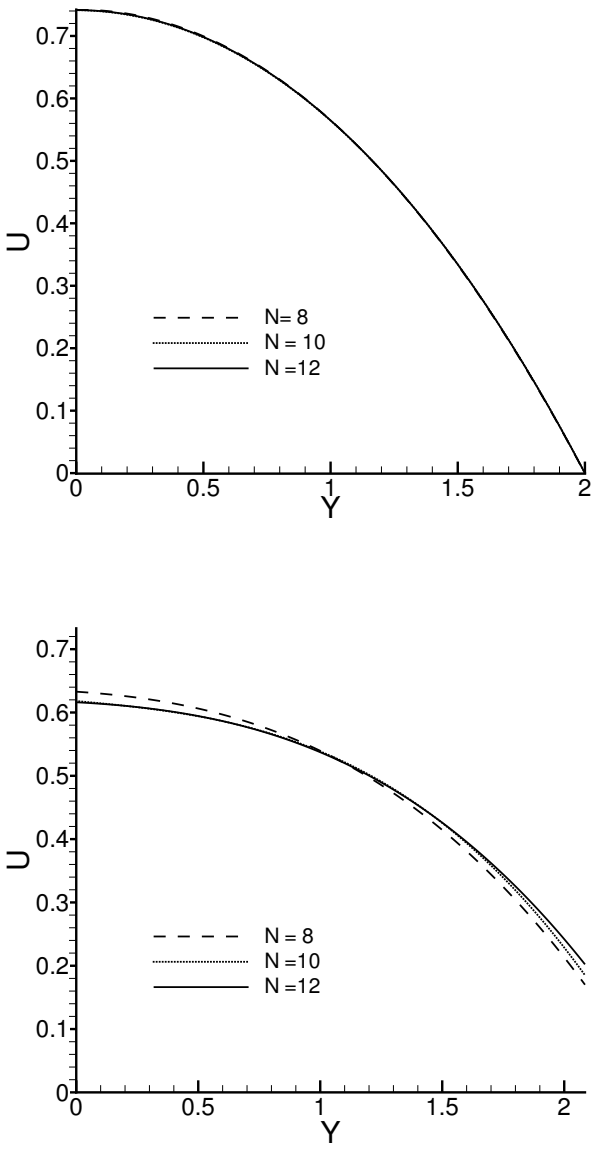

Figure 4.20: Horizontal velocity profiles at $x = 8$ (top) and $x = 10.2$ (bottom) with $M = 4$, $Re = 1$.

different combinations of the two temporal approximations. The combination that provides the most accurate approximation in time is OIFS2/AB3. The increased computational overhead of using a high-order rather than a low-order scheme to track the free surface is negligible compared to the overall cost of the simulation. The use of OIFS2 instead of OIFS1 for the discretization of the material derivative in the momentum equation results in an increase of around 25% in computational time to compute the source term in the momentum equation at each time step.

The influence of the time step on the location of the free surface is now investigated for each of the three Adams-Bashforth schemes. This is shown in Fig. 4.23 for time steps in the range $[10^{-4}, 10^{-1}]$. A time step of 10^{-1} is clearly inadequate in all cases to obtain a converged location of the free surface. Furthermore, there are signs of instability when the forward Euler method is used, which is not unexpected. For all three schemes a time step of $\Delta t = 10^{-3}$ is required to obtain a converged solution in terms of the free surface location. One can observe the superior convergence properties of AB3 in the lower graph in Fig. 4.23 in that the free surface profile obtained with $\Delta t = 10^{-2}$ is very close to the temporally converged profile. Furthermore, in conjunction with an increase in the spatial order of convergence, as shown in Fig. 4.19, AB3 performs extremely well. The free surface profile in the case of AB3 has almost converged for $N = 8$. However, the obvious gain from this decrease in the polynomial order has to be traded off against convergence of the velocity profiles shown in Fig. 4.20. It is clear that the Poiseuille profile upstream (top picture) is insensitive to changes in the polynomial order, at least for sufficiently high large values of N. The situation is different just after the exit (bottom picture). Here the approximation obtained using $N = 8$ has not converged, the reason being the proximity of the singularity at the exit of the die. In most practical applications, especially with viscoelastic fluids, the main issue during extrusion is an accurate prediction of the swelling of the extrudate rather than a fully detailed description of the flow inside the domain. From this point of view, the gain in using a polynomial approximation with $N = 8$ would be quite significant. In this respect, AB3 provides an accurate as well as a stable approximation.

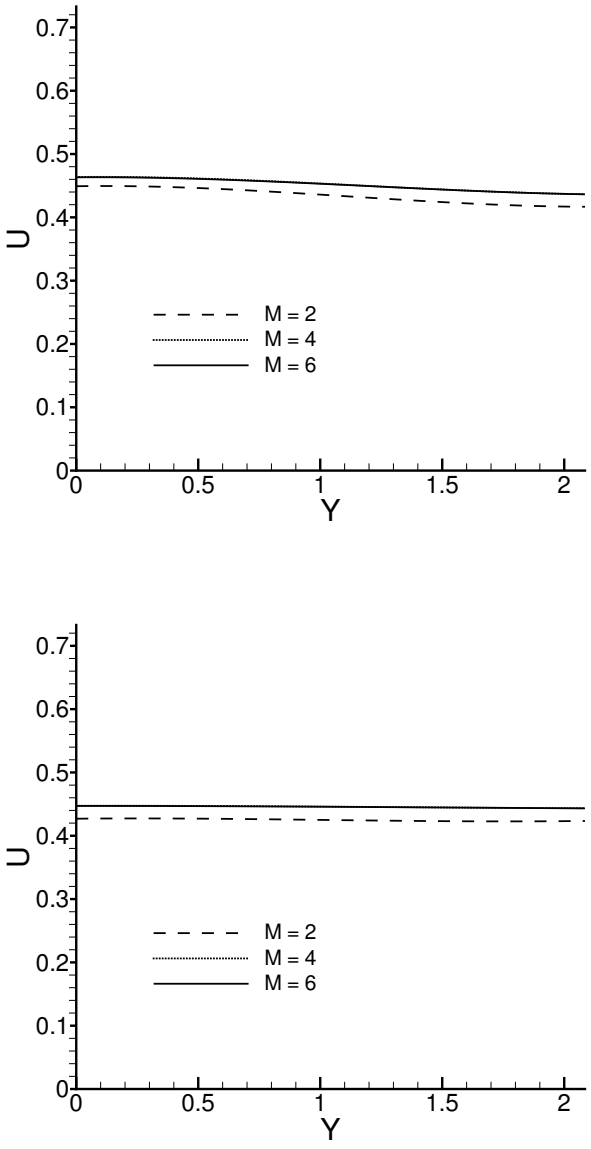

Figure 4.21: Horizontal velocity at $x = 12.8$ (top) and $x = 14$ (bottom) with $N = 12$, $Re = 1$.

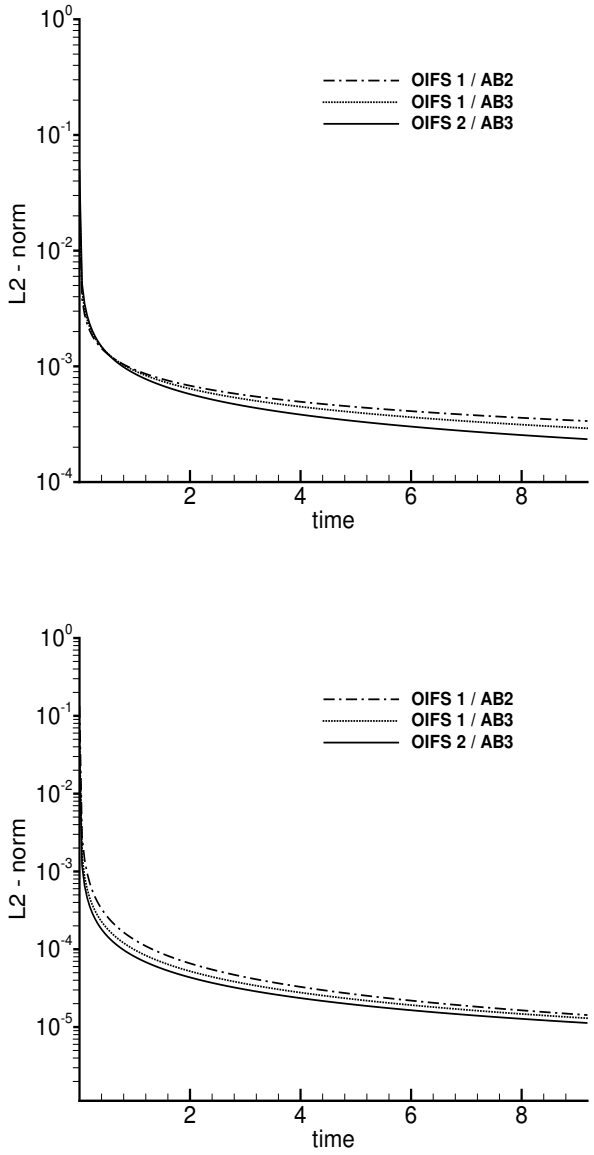

Figure 4.22: Dependence of relative error for the extra-stress tensor (top) and the velocity (bottom) on the different temporal approximations used.

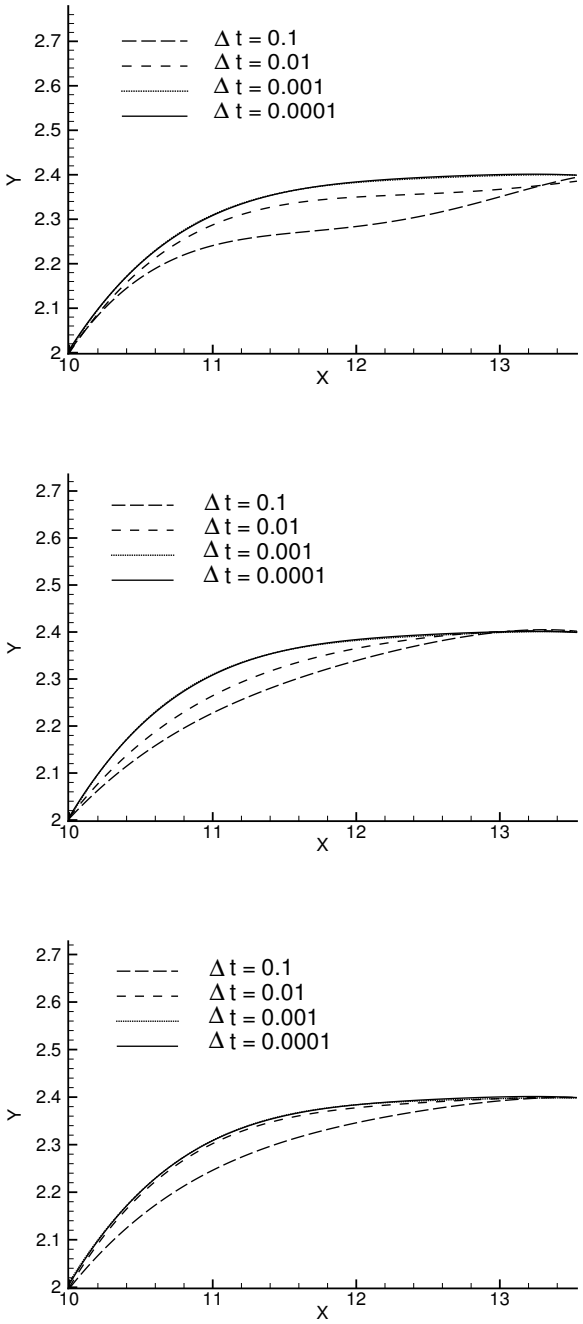

Figure 4.23: Location of the free surface for different values of Δt for the forward Euler scheme (AB1) (top), AB2 (middle), AB3 (bottom) for $N = 12$ and $M = 4$.

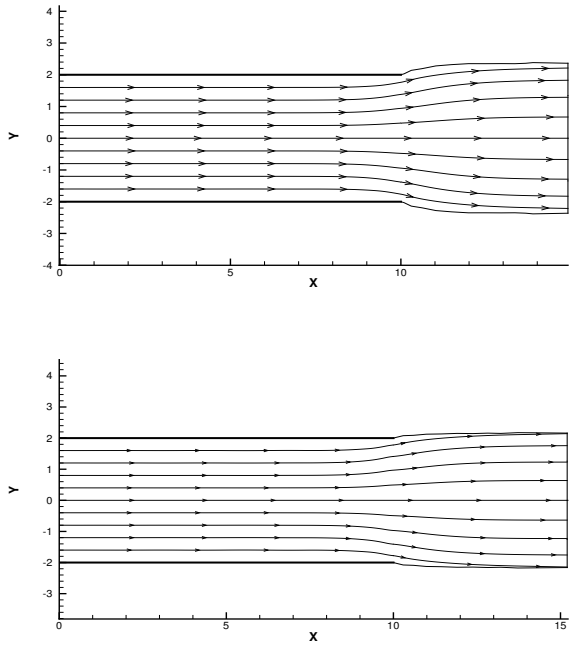

Figure 4.24: Streamlines for $Re = 1$ (top) and $Re = 10$ (bottom). Here $M = 4$, $N = 12$.

4.4.3 Effect of inertia

The effect of increasing Reynolds number is to inhibit swelling. As explained in Russo and Phillips [109], this is caused by two regions of the fluid exhibiting contrasting forces. Just as an example, the streamlines at steady state for $Re = 1$ and $Re = 10$ are shown in Fig. 4.24, respectively. The free surface profiles are shown in Fig. 4.25 for different values of Reynolds number. These profiles clearly demonstrate that swelling is inhibited as the Reynolds number is increased.

The dependence of the swelling ratio on Reynolds number is shown in Fig. 4.26 and the predictions obtained using the scheme described in this paper are compared with results reported in the literature. Surface tension is neglected in these simulations. The effect of inertia is clear; here $R/L = 0.2$. The different schemes give almost the same prediction, when inertia is discarded, with the spectral simulations from Ho and Rønquist [52] just

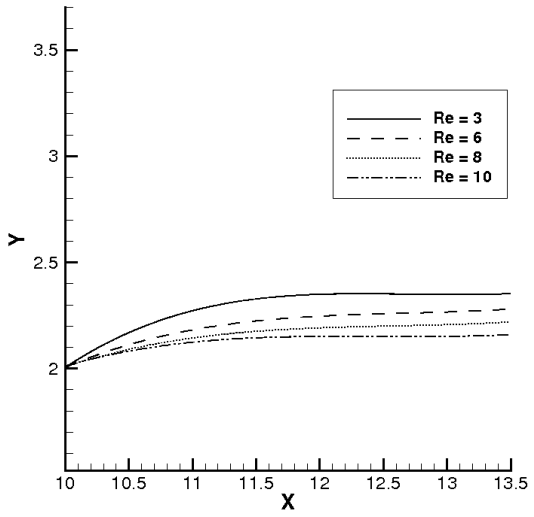

Figure 4.25: Influence of inertia on the free surface profiles. $M = 4$, $N = 12$.

underestimating the value of $SR = 1.198$. A clear pattern is present as the Reynolds number increases, and there is a very good agreement with the swelling ratios obtained by Omodei [92], particularly for $Re = 1$ and $Re = 10$.

The exact values of the swelling ratios from different sources are reported in Table 4.4 and 4.5. Moreover, the effect of mesh refinement is also considered in Tables 4.6 and 4.7. It is worth noticing how the mesh refinement becomes more evident with increasing Re. In fact, for $Re \geq 7$, a polynomial order $N = 14$ is required to ensure the same accuracy of convergence that, for lower Reynolds number, is obtained already at $N = 10$.

Another consequence of increasing inertia is an increase in the normal stress jumps, due to a higher acceleration required for the fluid particles to achieve a plug flow configuration. Detailed values of these jumps are given in Table 4.8. We remark that, although the values of τ_{xx} and τ_{yy} on the centreline, are approximately equal and opposite, since the continuity equation requires mass to be conserved in a Newtonian fluid, we cannot expect the same close to the wall, where the solution exhibits singular behaviour. This

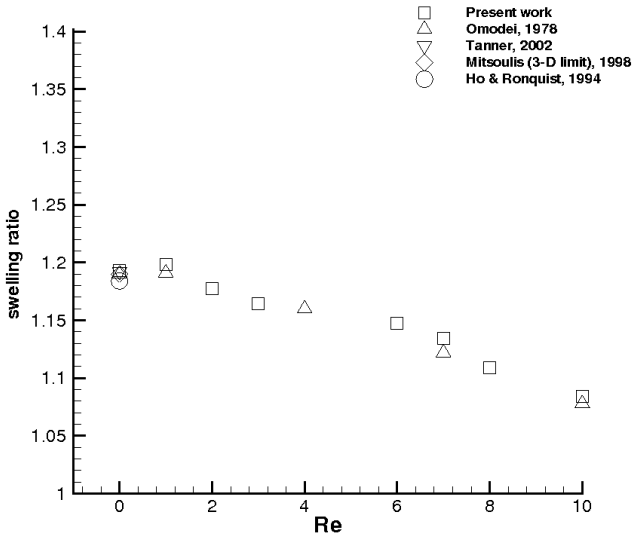

Figure 4.26: Comparison of influence of Re on swelling ratios with results in the literature. Our results have been obtained with $M = 4$, $N = 12$.

Re \ Source	Present work	Omodei, 1979
0	1.193	1.191
1	1.198	1.191
2	1.177	NA
3	1.164	NA
4	1.158	1.160
6	1.147	NA
7	1.134	1.122
8	1.109	NA
10	1.0844	1.078

Table 4.4: Dependence of swelling ratio on inertia without surface tension. Comparison with Omodei [92].

Present work	1.193
Omodei [92]	1.191
Tanner [119]	1.192
Mitsoulis (3-D limit) [85]	1.190
Ho and Rønquist [52]	1.184
Georgiou and Boudouvis [38]	1.186

Table 4.5: Dependence of swelling ratio on inertia without surface tension in the case of creeping flow ($Re = 0$). Comparison with previous results.

N \ Re	0	1	2	3	4	6	7	8	10
6	1.189	1.190	1.167	1.156	1.148	1.132	1.120	1.089	1.064
8	1.192	1.197	1.172	1.163	1.156	1.139	1.129	1.098	1.072
10	1.193	1.198	1.177	1.164	1.157	1.146	1.131	1.104	1.079
12	1.193	1.198	1.177	1.164	1.158	1.147	1.134	1.109	1.084
14	1.193	1.198	1.177	1.164	1.158	1.147	1.135	1.110	1.083
16	1.193	1.198	1.177	1.164	1.158	1.147	1.135	1.110	1.083

Table 4.6: Influence of mesh refinement (polynomial order) on the calculated swelling ratios for different values of Re .

M \ Re	0	1	2	3	4	6	7	8	10
2	1.192	1.197	1.175	1.162	1.152	1.141	1.130	1.103	1.075
4	1.193	1.198	1.176	1.164	1.156	1.146	1.132	1.108	1.084
6	1.193	1.198	1.177	1.164	1.158	1.147	1.134	1.109	1.085

Table 4.7: Influence of mesh refinement (number of elements) on the calculated swelling ratios for different values of Re. .

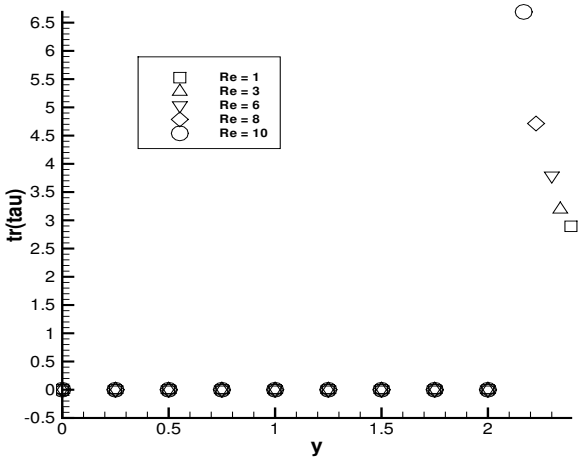

Figure 4.27: Trace of the stress tensor along the exit cross-section ($x = 10$), for different Reynolds numbers. The values are calculated using the approximations in the downstream element. $M = 4$, $N = 12$.

is even clearer in Fig. 4.27. Here the trace of the stress tensor is plotted against y at the exit of the die. It is zero everywhere, as it should be for a Newtonian fluid, except in the proximity of the singularity. In Fig. 4.28 we show how this singularity is better captured with higher order polynomials. The figure shows the values of T_{xx} at $x = 10$, $y = 2$ as a function of Re. The distance downstream at which relaxation of the extrudate is accomplished is shown in Fig. 4.29. As expected, the extrudate takes longer to relax to a downstream plug flow as Re increases. Eventually, it settles down after around 2.5 multiples of the radius of the die. This value is in the range reported in the simulations of Tanner [119]. Again the predictions with $N = 10$ and $N = 12$ are close. It is not a principal aim to investigate the maximum Reynolds number attainable before numerical breakdown occurs. Nevertheless, we run a few simulations for higher values of Re to check that contraction occurs when inertia is large enough and also to support the findings reported in Russo and Phillips [109] regarding the physical reason behind the Newtonian die-swell. In particular, we report on predictions obtained for $Re = 100$, $We = 0$ and $N = 12$.

Re	τ_{xx} (FS)	τ_{yy} (FS)	τ_{xx} (CL)	τ_{yy} (CL)
1	5.027	-8.021	-0.43282	0.43193
3	6.275	-9.361	-0.497581	0.497521
6	9.279	-13.16	-0.685647	0.685665
8	12.041	-16.848	-0.855826	0.855317
10	17.121	-23.88	-1.13528	1.13625

Table 4.8: Dependence of normal stress jumps at the exit at the free surface (FS) and the centreline (CL) on Re.

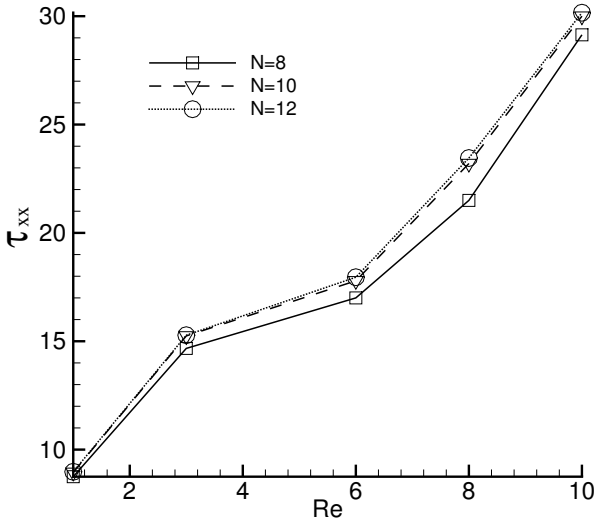

Figure 4.28: Axial normal stress at the exit ($x = 10$, $y = 2$). $M = 4$

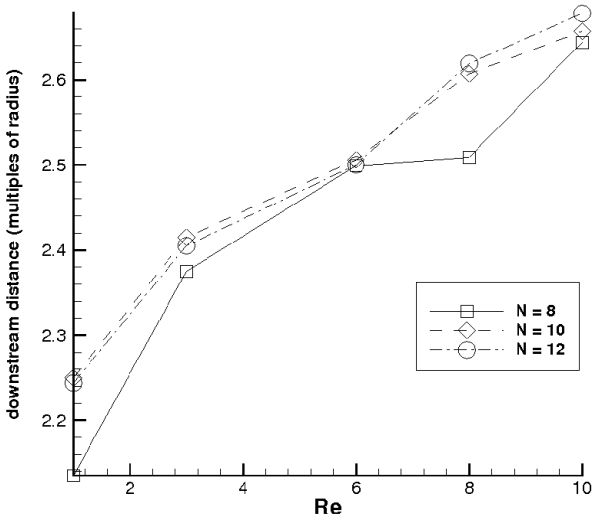

Figure 4.29: Influence of inertia on downstream relaxation distance. $M = 4$.

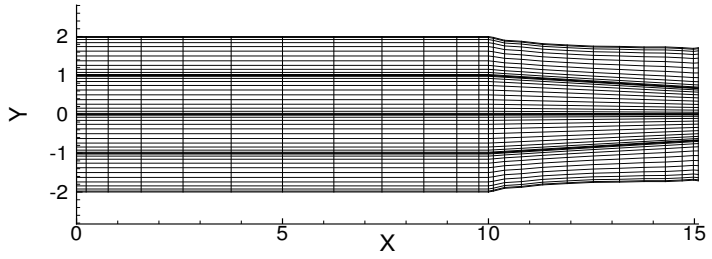

Figure 4.30: Mesh at steady state for $Re = 100$. $M = 4$, $N = 12$.

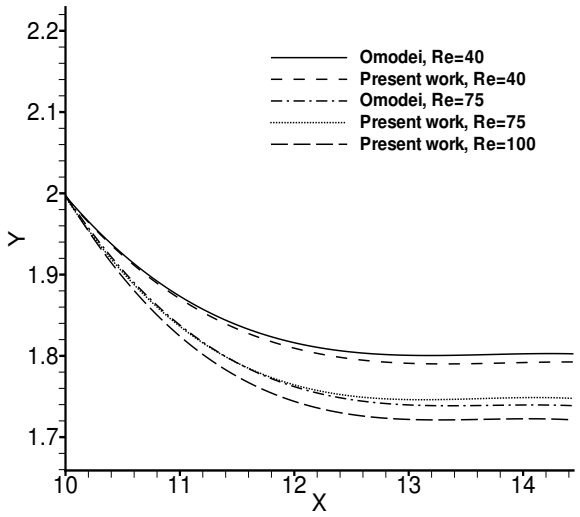

Figure 4.31: Comparison of the free surface locations. Surface tension is neglected. In the present simulations $M = 4$, $N = 12$.

The mesh is shown in Fig. 4.30, and the profile of the free surface is shown in Fig. 4.31 and compared with the results from Omodei [92]. We can conclude that the numerical scheme can produce satisfactory results over a significant range of Reynolds numbers.

4.4.4 Effect of surface tension

In the previous simulations, surface tension was neglected. If it is included in the mathematical model through (3.29), the result is a decrease in swelling, as expected. In Fig. 4.32, the convergence of the location of the free surface with respect to the polynomial order is shown. Once again, the stable, third order Adams-Bashforth scheme seems the most reliable. Convergence with respect to the time step is shown in Fig. 4.33.

The effect of surface tension on the free surface profiles is shown in Fig. 4.34 for $Re = 1$ for different values of We. In Fig. 4.35, the swelling ratios predicted by the method described in this paper and the method

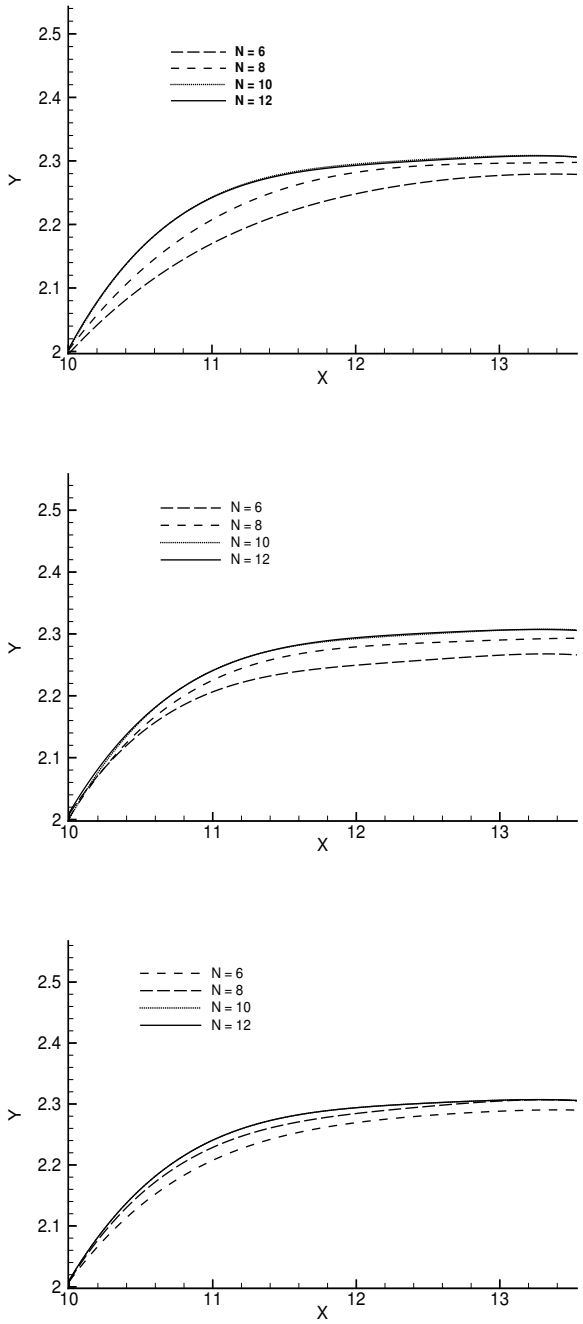

Figure 4.32: Location of the free surface for different values of N using different temporal schemes for the discretization of the temporal derivative. Forward Euler (top), AB2 (middle), AB3 (bottom). $\Delta t = 10^{-3}$, $M = 4$. Surface tension is included, $We = 2.5$.

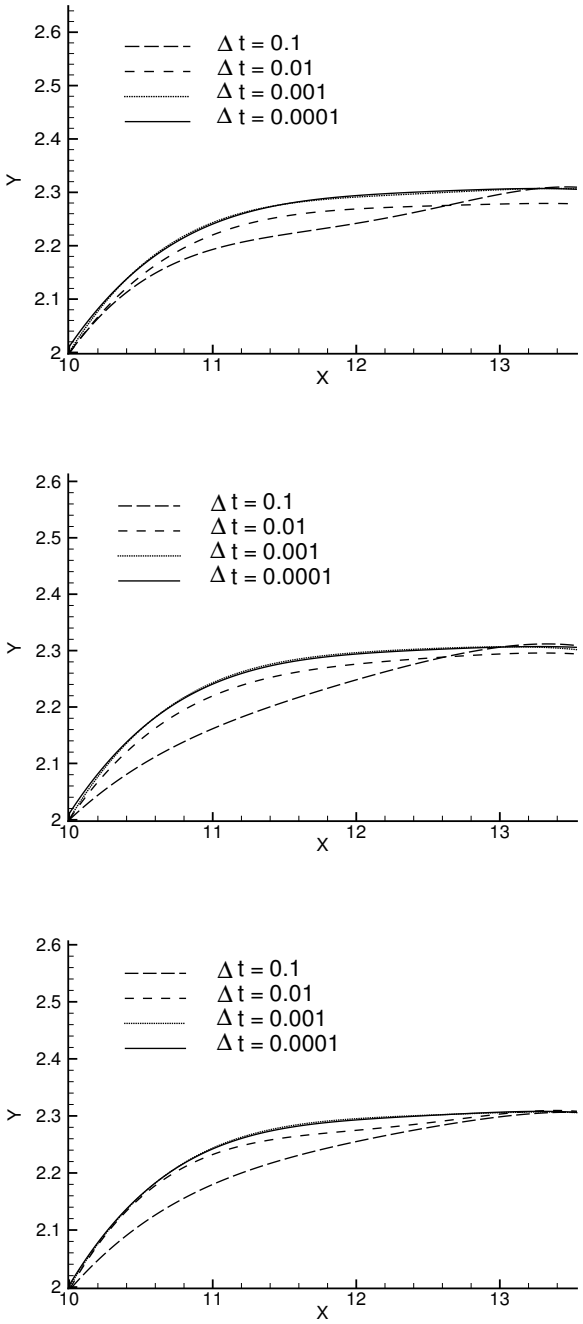

Figure 4.33: Location of the free surface for different values of Δt using different temporal schemes for the discretization of the temporal derivative. Forward Euler (top), AB2 (middle), AB3 (bottom). $N = 12$, $M = 4$. Surface tension is included, $We = 2.5$.

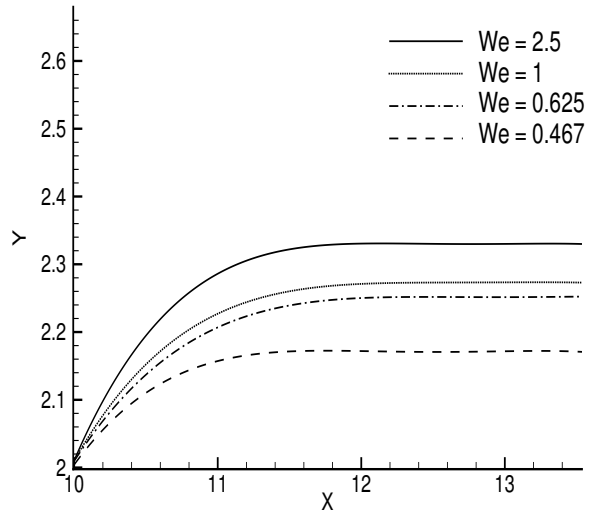

Figure 4.34: Free surface profiles for different values of surface tension for $Re = 1$ and $N = 12$.

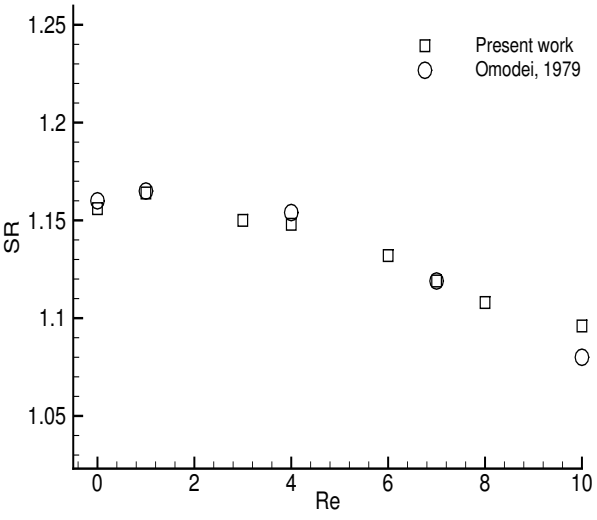

Figure 4.35: Swelling ratio vs inertia: surface tension included with $We = 2.5$.

Re \ We	∞	2.500	1.000	0.625	0.467
1	1.196	1.164	1.130	1.118	1.083
3	1.164	1.141	1.125	1.100	1.075
10	1.084	1.082	1.081	1.080	1.079

Table 4.9: Dependence of swelling ratio on inertia and surface tension.

described in Omodei [92] are compared. In the simulations of Omodei [92], in the same fashion as Goren and Wronski [43], a parameter is used which is not simply an indicator of the surface tension, but of the surface tension versus inertia. In our formulation of the problem the usual definition of the Weber number, $We = \frac{\rho U^2 L}{\sigma}$, is used and, with our choice of the parameters, effectively $We = 1/\sigma$. More precisely, the surface tension parameter in [92] is defined as

$$S = \frac{\sigma \rho h_0}{\mu^2}.$$

Since in [92] $\mu = 1$ and $h_0 = 1$, then

$$S = \frac{\sigma Re}{2}. \tag{4.8}$$

This means that, when the Reynolds number is fixed, a corresponding value of S is recovered from each value of σ and such values of σ change with Re. The reason behind the choice of increasing S with Re is the attempt to highlight the effect of the surface tension also for $Re \simeq Rr_{cr,sw}$, when effectively the surface tension becomes negligible (see §4.3.2). However, the ratio $\sigma = 2S/Re$ changes very little with Re and σ. Therefore we decided to use $\sigma \in [0.4, 2.4]$ for our calculations, which corresponds to $Re = 1$ in Table 1 in [92]. For comparison purposes, if the corresponding exact value of S does not appear in Table 1 in [92], namely, if the corresponding swelling ratio is not reported, then an extrapolation is performed. For example, for $Re = 10$ we have $S = 5$ from (4.8), while simulations in [92] have been performed for $S = 0, 6, 12$. Corresponding to $S = 5$ we then extrapolated the value for the swelling ratio $SR = 1.08$. A quantitative summary of the

effect of surface tension on the changes of inertia is highlighted in Table 4.9. As previously pointed out, the effect of the surface tension decreases with increasing inertia. In fact, the opposite effect is also true; the effect of inertia decreases with increasing surface tension. This is not a surprise, because, when inertia acts in support of the normal stress balance, i.e., when $Re \simeq Rr_{cr,sw}$, the curvature of the free surface tends to flatten. Therefore the driving force which tries to minimize the curvature of the free surface produces a less evident effect.

Simulations at higher Re including surface tension have been performed by Omodei in [92], and they show that above the value of the Reynolds number at which the fluid starts shrinking, the effect of surface tension is to increase the final diameter. This is confirmation that, in the attempt to minimize the curvature of the free surface, the presence of surface tension counteracts both tendencies of the fluid to expand or contract (depending on whether the Reynolds number is below or above the threshold value).

Chapter 5

Extrusion of Viscoelastic Fluids: Numerical Simulations

5.1 Introduction

The extrusion of viscoelastic fluids is common in a range industrial processes such as blow moulding and injection moulding. In the case of viscoelastic fluid, the phenomenon can be explained by an elastic recoil process, which results in much larger swelling ratios than the Newtonian case. In fact, the elastic energy stored in the fluid in the die is responsible, for values of the swelling ratio even up to twice the radius of the die once the fluid exits the die. As the polymer melt is sheared through the die, the molecules become extended with the greatest orientation near the wall. The elastic energy stored in the stretched molecules in the die is relaxed once the fluid leaves the confines of the die causing the molecules to coil up. Thus the molecules contract in the flow direction and expand in the lateral direction. In the die, there is a tension along the streamlines associated with the normal stresses. When the fluid exits the die, the tension along the streamlines will relax by contracting in the longitudinal direction. For an incompressible fluid, this gives rise to a lateral expansion of the fluid.

An early physical interpretation of elastic and inelastic die swell was proposed by Tanner [117, 118]. In the inelastic case, Tanner [117] divided the flow into two regions: an inner core region and and an outer layer. Russo and Phillips [109] followed this approach to provide an explanation of the Newtonian die-swell mechanism. Inelastic non-Newtonian fluids are characterized by a viscosity that is dependent on the shear-rate. Tanner [117] derived an expression for the swelling ratio that is dependent on the ratio of the viscosity of the fluid in the outer layer to the viscosity of the fluid in the core region. Swelling of the extrudate is predicted by this theory when the ratio is greater than unity, i.e. for shear-thinning fluids. The same expression for the swelling ratio is also used by Tanner [117] for a Maxwell fluid, where the viscosities in the two regions are calculated in terms of the relaxation time and the average extensional rate.

In the elastic theory, the swelling ratio is calculated from the so-called *recoverable stress*. This is a measure of the elastic energy stored in the molecules which can be *recovered* once the fluid leaves the die. Mathematically, this can be expressed as the ratio between the first normal stress difference and the shear stress at the wall in the die. Tanner [120] revisited this theory some thirty-five years later and modified it in order to treat more complex constitutive models such as the PTT or XPP models. Both theories, quoting Tanner himself, are clearly simplified versions of the real problem but which, nevertheless, have proved themselves to be very useful predictive tools. They aid an understanding of the die-swell problem and also provide quantitative data which, especially in the past, were lacking from experiments. Recently, more experimental results have become available, and these will be discussed later in Chapter 6.

Crochet and Keunings [28, 29] performed finite element simulations using the UCM and Oldroyd-B models. In the case of the UCM model, they focused on the dependence of the swelling ratio on the Deborah number. For the Oldroyd-B model, they mainly computed swelling ratios against the recoverable shear parameter in order to compare their results with Tanner's theory. The recoverable shear is defined as the ratio of the first normal stress

difference to the shear stress, both calculated at the wall of the die. We define it as $R_s = (N_{1,w}/\tau_{xy})_w$, and represents what can actually be recovered from the extra tension in the direction perpendicular to the streamlines. This is a feature typical of elastic fluids and it is, for instance, highlighted in the tilted trough experiment. In this experiment, a polymeric liquid is confined in the interior of a tetrahedral block with a U-cross section and flows due to gravity when the block is tilted at one end. During the flow, the interface between the polymer and the air is not flat, but is pulled in the direction normal to the flow due to the extra tension mentioned earlier.

In their calculations, Crochet and Keunings [28, 29] report swelling ratios of up to 100% for $R_s = 4$. Their results are in good agreement with Tanner's formula up to $R_s = 2$. However, their numerical predictions are well above the theoretical ones for $R_s > 2$. This does not necessarily mean that the numerical simulations are incorrect, since Tanner's theory is based on a simplified analysis in which certain assumptions have been made. It seems reasonable to argue that Tanner's theory is not completely satisfactory for models with more than one time constant. In fact, the theory was developed from an integral constitutive equation with only one temporal characteristic quantity. The departure of numerical predictions from Tanner's theory reported in Crochet and Keunings [28, 29] and Russo and Phillips [108] is also noted by Tomé et al. [124, 125], who used a finite difference technique in which the convective terms were discretized using a VONOS upwinding scheme. The computation of the polymeric extra-stress tensor on the rigid boundaries uses a change of variables to smooth the stress tensor in the constitutive equation. The free surface is tracked using a marker-and-cell (MAC) method. A maximum swelling of almost 110% is reported for both planar [125] and axisymmetric [124] jets. In the latter case, a remarkable 50% jump in the swelling ratio takes place around $R_s = 2$, which corresponds to $Wi = 0.5625$ in that simulation. In planar extrusion, the growth rate of the swelling ratio suddenly increases around the same value. Clearly, further investigation is needed to better understand this feature, which seems to be typical of an Oldroyd-B fluid.

Tuna and Finlayson [126] focused on the calculations of the exit pressure

loss in the extrudate swell. They used a Galerkin finite element method to solve the extrudate swell problem for an Upper Convected Maxwell fluid. They confirm the increase in the swelling ratio with increasing Weissenberg number. The exit pressure loss is also proportional to the elastic response of the fluid. In the same fashion as Reddy and Tanner [103], they propose a formula to calculate the pressure loss as a function of the R_s, although it is not clear whether this formula calculates the pressure at a point L units upstream from the exit or the effective exit pressure loss. We will discuss this point further in §5.3.3.

On the other hand Reddy and Tanner [103] analyzed the die swell of a second order fluid with the assumption of a creeping flow. Finite elements were the basis of the numerical method. They reported values of swelling ratios very similar to the ones obtained using an Upper Convected Maxwell fluid, and proposed the aforementioned formula for calculating the exit pressure loss which we will describe in §5.3.3.

5.2 Viscometric behaviour of UCM-type and XPP-type models

Among the several, nonlinear constitutive models describing viscoelastic fluids, the ones we chose to analyze in this thesis may be located at the opposite ends of the spectrum in terms of level of refinement, at least as far as nonlinear models are concerned. The Oldroyd-B model [90] can be considered the first nonlinear constitutive equation based on the assumption that the nonlinearity of the rate of change in the deviatoric stress tensor $\boldsymbol{T}$ is required in order to satisfy the objectivity principle. Such a principle states that the scalars, vectors and tensors involved in a constitutive model have to be invariant under the change of reference frame. However, as described in § 2.6.1, the Oldroyd-B model predicts constant shear viscosity, a zero second normal stress difference and unbounded extensional viscosity. Therefore, it is useful only to describe Boger fluids at small shear rates.

On the other hand, the XPP model [132] is rather sophisticated and predicts

several features of polymer melts. In simple shear flow (Fig. 3 in [132]), the dimensionless viscosity is monotonic at small shear rates and shows a maximum at large shear rates. In both cases a plateau is reached asymptotically as $\dot{\gamma} \to \infty$. Moreover, in steady shear flow the model is shear thinning. This behaviour in shear flows is observed in real melts and is due to the effect of the orientation of the molecules.

If we then look at elongation flow (Fig. 3 in [132]), the transient Trouton ratio in response to increasing Hencky strain is also predicted. Moreover, the stretch in the extensional case occurs almost instantaneously and is twice the stretch as in shear flow. The reason for this is that the molecules do not need to orientate before starting to stretch, as they do in shear flows.

The XPP model has in total four independent free constants per mode which can be fitted to experimental data. The Maxwell moduli and relaxation times are linear parameters while the number of arms and orientation-to-stretch ratios are nonlinear parameters. It might be argued that four free constants are too many, but the capability of the XPP model to fit experimental data from different materials is considerable. The quantitative predictions for the branched low density polyethylene Lupolen $1810H$ as well as for the high density polyethylene Statoil $870H$ (Figs. $5-8$ and 10, respectively, in [132]) are to be considered a remarkable achievement.

5.3 Numerical simulations of polymer solutions: UCM and Oldroyd-B models

The aim of this section is to present our numerical simulations of extrusion of polymer solutions. We focus on the typical features of Oldroyd-B and UCM fluids. Despite presenting some unphysical characteristics, these models are non-trivial to be solved. In fact, they are much less stable than more complex models such as PTT or Giesekus [1, 143]. However, they still approximate polymer solutions quite well in the limit of small shear rates.

The mathematical details of these models have been described in Chap-

ter 2. The UCM model is the limit case of the Oldroyd-B for $\beta = 0$. In this case the whole contribution for the viscosity is polymeric. As a result, there is no dissipation related to a solvent viscosity.

5.3.1 A summary of the problem

We recall that swelling in elastic fluids is caused by the elastic recovery of the molecules when the fluid leaves the die. Those molecules undergo swelling in the radial direction as a consequence of stress relaxation. The relaxation process takes place as a result of the remove of the shear load outside the die. It can be seen as an effect of the memory of the fluid, as underlined by Huang and Lu [54] in their comparison of K-BKZ fluids. Tanner [117] also used a K-BKZ constitutive equation to derive his classical equation relating swelling ratio, SR, to the recoverable shear parameter $R_s = \frac{N_{1,w}}{\tau_w}$, where $N_{1,w}$ and τ_w are the first normal stress difference and the shear stress, respectively, both calculated at the wall.:

$$SR = 0.2 + \left[1 + \frac{1}{12}\left(\frac{N_{1,w}}{\tau_w}\right)^2\right]^{1/4} = 0.2 + \left[1 + \frac{1}{12}R_S^2\right]^{1/4} \qquad (5.1)$$

This formula was derived for planar extrusion. The constant 0.2 is the viscous swelling ratio, while the second term on the right-hand side represents the departure from the Newtonian swelling due to the elastic recoil mechanism. A slightly modified form was proposed for the axisymmetric geometry.

Many numerical simulations and experiments have been carried out on this problem. Various constitutive models and real melts have been tested, and there is general agreement on the following aspects:

- the swelling ratio increases with the elasticity of the fluid; such elasticity is generally represented by the relaxation time (or times, for multimode fluids);
- consequently, swelling is proportional to the first normal stress difference and the shear stress at the wall in the die;

- the swelling is proportional to the pressure drop at the exit of the die;
- for low Reynolds number, the effect of inertia is negligible compared to the effect of elasticity;
- in experiments performed in capillary rheometers, the flow induced by the contraction has a strong extensional component which relaxes within the die; therefore, only for dies which are long enough, can the flow really be considered parabolic when it reaches the exit. This observation clearly does not apply to numerical simulations if a fully developed Poiseuille profile is assumed inside the die.

The computational domain is as follows: the die is $[0,10]\times[0,d]$ and the downstream region is, at the time $t=0$, is $[10,16]\times[0,d]$ and $[10,20]\times[0,d]$ for $Wi=0.25$ and $Wi=0.50$, respectively. In our simulations the exact parabolic profile is imposed at inlet ($0\le y\le d, d=2$). The profile for an Oldroyd-B fluid is

$$u(y)=\frac{d^2}{2\eta_{tot}\beta}\Big(-\frac{\triangle p}{\triangle x}\Big)\Big[\frac{y}{d}-\Big(\frac{y}{d}\Big)^2\Big],\qquad u(0)=u(d)=0,\qquad v(y)=0, \tag{5.2}$$

$$\tau_{xx}=2\eta_{tot}(\lambda_1-\lambda_2)2\Big(\frac{\partial u}{\partial y}\Big)^2,\qquad \tau_{xy}=\eta_{tot}\Big(\frac{\partial u}{\partial y}\Big),\qquad \tau_{yy}=0. \tag{5.3}$$

Therefore, noticing that $\dot\gamma_w=\mid\frac{\partial u}{\partial y}\mid_{y=d}$, and defining $Wi=\lambda_1\dot\gamma_w$ from Eqs. (5.3) and (2.54) we have

$$R_S=4(\lambda_1-\lambda_2)\dot\gamma_w=4(1-\beta)Wi. \tag{5.4}$$

We remark that the definition above of the Weissenberg number is equivalent to scaling lengths with d and velocities by $4u_{max}$, as can easily be verified by combining (5.2) and (5.3). Here u_{max} is the maximum velocity in the channel along the centreline given by

$$u_{max}=\frac{\triangle p}{\triangle x}\frac{d^2}{8\eta_{tot}\beta}. \tag{5.5}$$

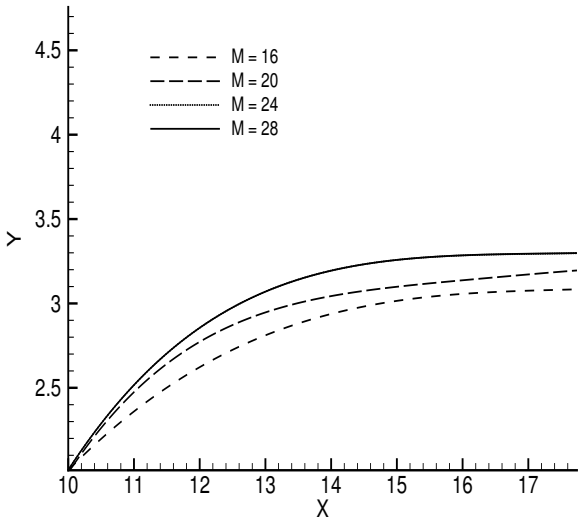

Figure 5.1: Convergence of the location of the free surface with the number of spectral elements M. Here $N = 8$ and $\Delta t = 10^{-4}$. Oldroyd-B model: $Wi = 0.5$, $\beta = 1/9$.

Scaling lengths with d and velocities with $8u_{max}$ leads us to set the modulus of the density as $\rho = \frac{1}{4u_{max}}$ to keep the Reynolds number constant and equal to 0.5.

Unless stated otherwise, all the simulations in § 5.3.2 have been performed for $Re = 0.5$, $Wi = 0.5$ and $\beta = 1/9$. In § 5.3.3, we present results for a range of values of Wi and β. Comparisons with available results in the literature will be presented.

5.3.2 Analysis of convergence and contour plots

In the same fashion as in the Newtonian case [111], we analyze the convergence of the location of the free surface for the Oldroyd-B model in order to find the optimal values for the spatial and temporal discretization parameters. The free surface profiles are shown in Figs. 5.1-5.3.

The numerical scheme used for updating the position of the free surface

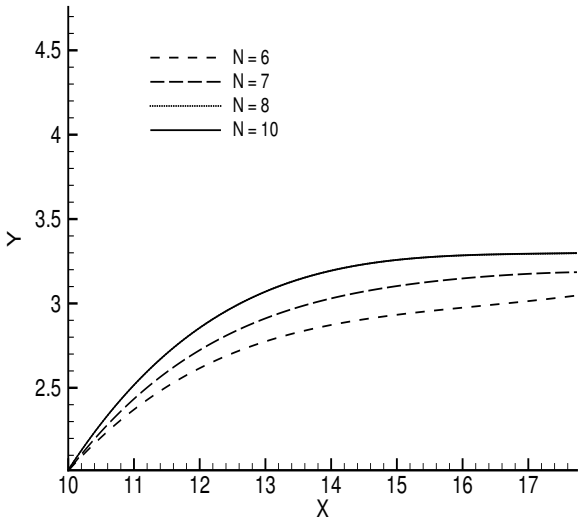

Figure 5.2: Convergence of the location of the free surface with the number of polynomial approximation N. Here $M = 24$ and $\Delta t = 10^{-4}$. Oldroyd-B model: $Wi = 0.5$, $\beta = 1/9$.

is the third-order Adams-Bashforth scheme. A converged profile of the free surface is achieved for the values of $N = 8$, $M = 24$ and $\Delta t = 10^{-4}$. These are the values of the spatial and temporal discretization parameters used in all the calculations for Oldroyd-B and UCM models, although for large values of Wi, convergence of the location of the free surface is checked again.

The contour plots of the horizontal velocity, normal stress and shear stress and shown in Figs. 5.4 and 5.5 for $Wi = 0.25$ and $Wi = 0.5$, respectively. A few remarks can be pointed out from the contour plots.

The increase in elastic response is clear looking at a number of factors, including the values of the swelling ratio and the normal stress. The ratio between the values of the normal and shear stress is roughly $2:1$ for $Wi = 0.25$ and $4:1$ for $Wi = 0.5$. Also, the value of the shear stress at $Wi = 0.50$ is roughly twice as much as its corresponding value at $Wi = 0.25$, whereas the normal stress increases almost quadratically. This is in agreement with the analytical solutions summarized in Eq. (5.2)-(5.3).

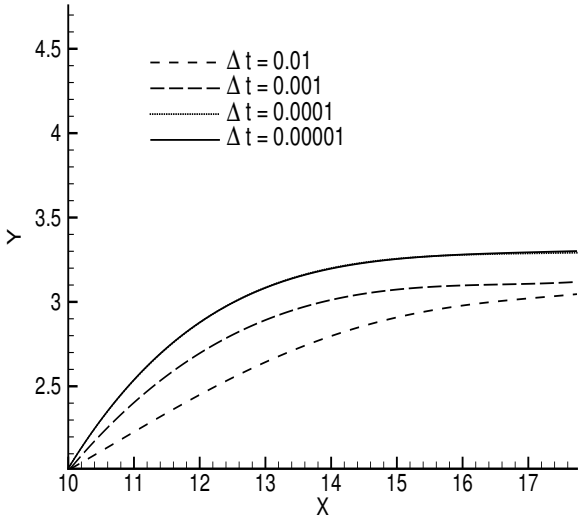

Figure 5.3: Convergence of the location of the free surface with choice of time step Δt. Here $M = 24$ and $N = 8$. Oldroyd-B model: $Wi = 0.5$, $\beta = 1/9$.

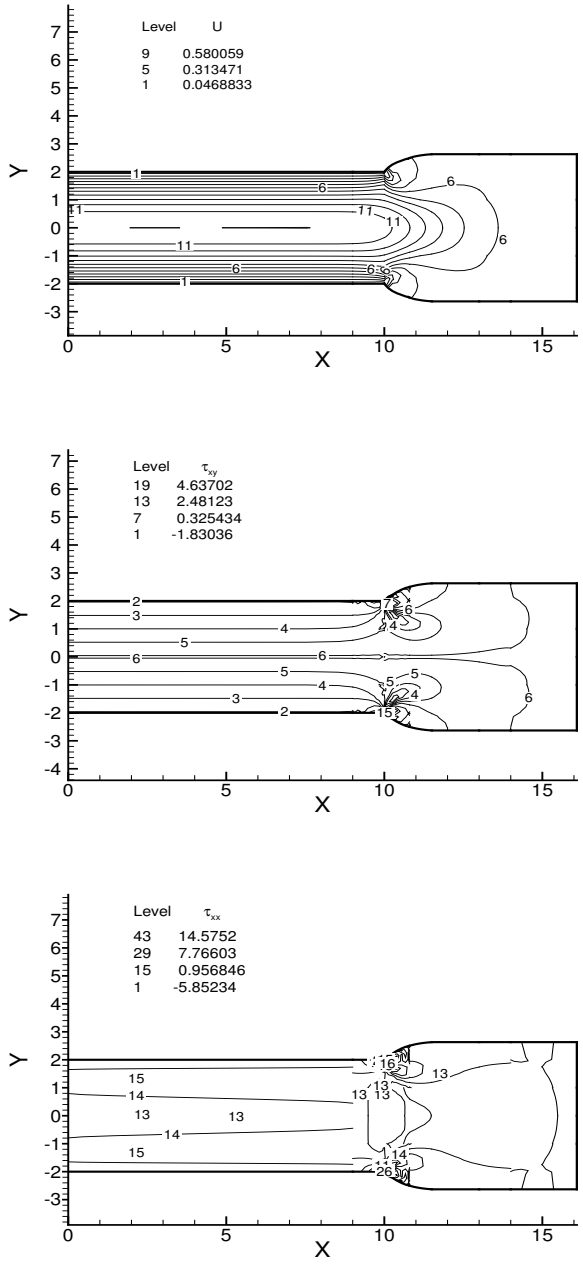

Figure 5.4: Contour plots of the horizontal velocity (top), shear stress (middle) and normal stress (bottom). Oldroyd-B model: $Wi = 0.25$, $\beta = 1/9$.

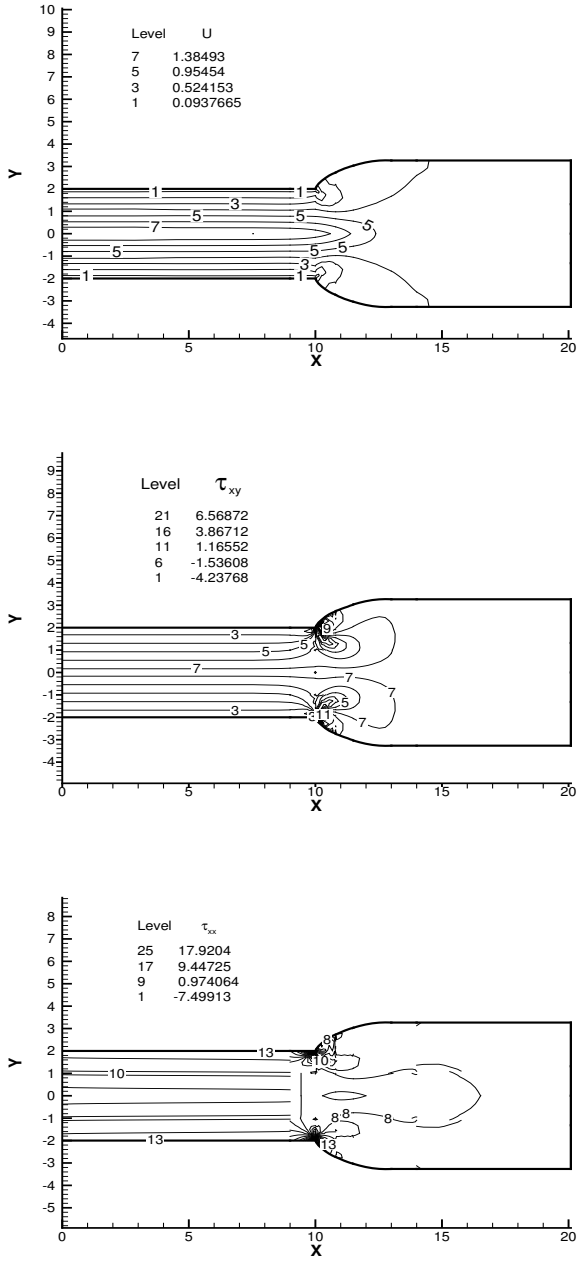

Figure 5.5: Contour plots of the horizontal velocity (top), shear stress (middle) and normal stress (bottom). Oldroyd-B model: $Wi = 0.5$, $\beta = 1/9$.

The contour plots shown in Fig. 5.4 and 5.5 reproduce closely the trend reported in the literature. For example, our results are very similar to the ones in the classical papers of Crochet and Keunings [28, 29] and the monograph of Tanner [119]. In particular, the contour levels become extremely dense near the exit. This is to be expected, since a steep boundary layer occurs because of the presence of the stress singularity. In Tables 5.1-5.2 the comparison between the numerical and analytical results for the Poiseuille flow in the channel is summarized for the sake of completeness.

	U_{max}	N_1	τ_{xy}
Analytical	0.80	1.42	-1.60
Numerical	0.78	1.43	-1.56

Table 5.1: Comparison of the values of the velocity at the centreline and the stress at the wall. Oldroyd-B model: $Wi = 0.25$, $\beta = 1/9$.

	U_{max}	N_1	τ_{xy}
Analytical	1.60	5.68	-3.20
Numerical	1.59	5.67	-3.27

Table 5.2: Comparison of the values of the velocity at the centreline and the stress at the wall. Oldroyd-B model: $Wi = 0.50$, $\beta = 1/9$.

5.3.3 Analysis of the extrusion process

The main purpose of this section is to analyze the most important features that are present in the extrusion process. In the first part we analyze the die swell of an Oldroyd-B fluid. A few results for a UCM fluid are also presented in the last part of the section. We mainly focus on the following aspects of the problem:

- location of the free surface;
- exit pressure loss;
- swelling ratio;

Wi \ β	1/9	1/2	8/9
0.25	0.89	0.50	0.11
0.5	1.77	1.00	0.22
0.66	2.34	1.32	0.29
0.75	2.66	1.5	0.33
1	3.55	2	0.44

Table 5.3: Values of the recoverable shear stress R_S.

- normal stress difference at the exit.

The Weissenberg number varies in the range $(0.25, 1)$ and $\beta = 1/9\ , 1/2\ , 8/9$ are the choices for the viscosity ratios. This allows for comparison with results in literature, such as those reported in the papers of Crochet and Keunings [28, 29] and the monograph of Tanner [119], together with results from Tuna and Finlayson [126] and the finite difference based study of Tomé et al. [125].

The location of the free surface is shown in Fig. 5.6 for different values of Wi and β. Moreover, comparison of computed swelling ratios with available results in literature are shown in Fig. 5.7. The predicted swelling ratios obtained in the different simulations are quite close, although it is important to note that Crochet and Keunings [29], as well as Tanner [119] assumed creeping flow, i.e, $Re = 0$. Tomé et al. [125] assumed $Re = 0.5$. Tomé et al. [125] suggested that this was the likely reason for their results lying closer to Tanner's formula than the ones from Crochet and Keunings [29]. On the one hand this seems reasonable, bearing in mind that the swelling ratio decreases as inertia increases. On the other hand, for low values of Reynolds number, the effect of inertia is considered to be negligible compared with the effect of elasticity and Tanner's formula already includes a Newtonian factor of 0.2 and is independent, at least directly, on the Reynolds number. This is confirmed in Fig. 5.7, which the swelling ratios calculated for creeping flows are almost the same as for the case $Re = 0.5$. However, we have not fully understood the way in which R_S is calculated in Tomé et al.

[125]. The recoverable shear parameter, being defined as the ratio of two stresses, is a non-dimensional quantity. However, Tomé et al. [125] calculate it as $S_R = Wi\frac{\partial u}{\partial y}$, [1] which has the dimensions of shear rate, namely sec^{-1}. We suppose that the equations and the calculations in [125] are non-dimensional. However, it is rather surprising that in the end the value of S_R is independent of β.

Crochet and Keunings [29] adopted a mesh containing 75 elements and 357 nodes, with 1889 unknowns. On the other hand Tomé et al. [125] used a 280×120 structured mesh with uniform cell size of 1/40 of the slit width. Our spectral mesh has 24 elements and the polynomial order used is 8. The smallest element of the mesh is square and placed with the corner at the exit, is 1/4 of the slit width in size and its smallest subcell is 1/80 of the slit width. The total number of nodes is 1617, of which 65 are placed on the known boundary (either wall or inlet). Therefore, the total number of scalar unknowns is 9312.

In our calculations the swelling ratio increases with increasing Weissenberg number. Also, the swelling decreases with increasing β. This is to be expected since, adding solvent viscosity to the solution results in enhanced dissipation and reduced elastic response. Our results are in agreement with predictions of Bush [19] and Clermont and Normandin [27][2], who solved the axisymmetric problem. Of course it is a qualitative agreement due to the different nature of the geometry. Nevertheless, it is worth noting that the trend in the elastic response of the fluid is the same in all three works.

The values of R_S corresponding to different Wi and β are summarized in Table 5.3. As predicted by the formula (5.4), R_S increases linearly with Wi for a fixed value of β. As $\beta \to 1$, it still increases linearly with Wi but its value is much lower. This is to be expected, since in the limit case $\beta = 1$ the Newtonian model is recovered. However, due to the quadratic expression

[1] R_S in this thesis is the same as S_R in [125].

[2] For the sake of clarity, we remark that in [19] and [27] β is defined as $\beta = \frac{\eta_p}{\eta_{tot}}$. In fact, in their tables the swelling ratios increase with increasing β. This way, if we call their parameter β_p and our β_s, then $\beta_p = 1 - \beta_s$.

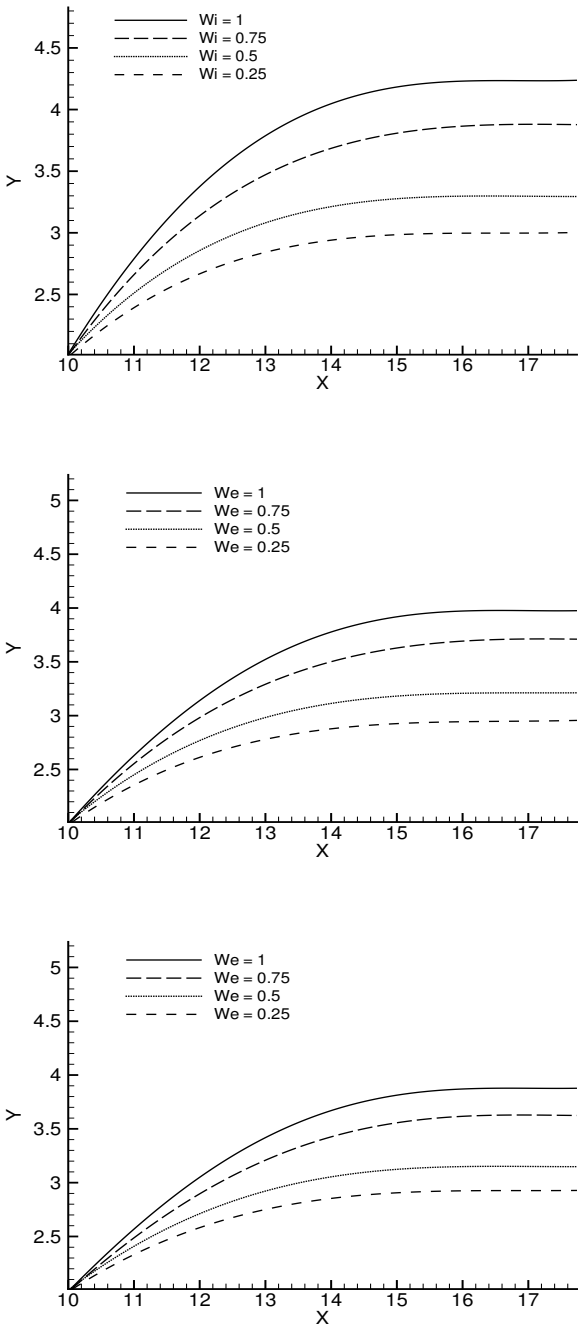

Figure 5.6: Location of the free surface with increasing Wi for an Oldroyd-B fluid for $\beta = 1/9$ (top), $\beta = 1/2$ (middle), $\beta = 8/9$ (bottom) .

in Eq. (5.1), for $\beta = 8/9$ Tanner's formula predicts a swelling ratio that is almost independent of Wi. This does not seem realistic, since polymeric viscosity should have an effect, especially because the larger the value of Wi, the more the swelling ratio is sensitive to changes in the viscosity ratios. In Fig. 5.8 the comparison between our computed swelling ratios and the predictions of Tanner's formula according to the values of R_S in Table 5.3 are shown. The discrepancy is obvious, as also reported by Bush [19]. It has to be remembered that Tanner's formula was derived using a KBK-Z integral constitutive equation with a single, relaxation time constant [117]. Therefore, it is reasonable to expect some departure if a retardation time is introduced in a model such as the Oldroyd-B case. When such a retardation time λ_2 is comparable to the relaxation time λ_1 (as in the case $\beta = 8/9$), the flat curve in Fig. 5.8 suggests that Tanner's formula is not completely suitable for the Oldroyd-B model. The determination of the range of validity of Tanner's formula is outside the scope of this work. Nevertheless it is worth pointing out its intrinsic exemplification, as well as its valuable usefulness, when used for comparison purposes.

In Fig. 5.9, where we define $AR = L/d$, we superimpose the extrudate shape for different values of d, the cross-section diameter of the slit die. For all three cases, we keep $Wi = 0.5$ by adjusting $\dot{\gamma}_w$ accordingly. As expected, since the flow rate has not been altered, the value of the swelling ratio lies between 62% and 63% in all three cases.

Another important feature of the extrusion process is the pressure loss. In experiments, as well as in the capillary rheometer, the flow in the die is induced by pushing the fluid from a reservoir through a contraction. Therefore, the pressure loss is calculated as the sum of the entry loss, due to the contraction, and the exit loss at the exit of the die. In the numerical simulations, when the flow is assumed fully developed in the die, only the exit loss is considered. Moreover, the entry loss for an UCM-type fluid is considered unreliable, due to reported values which are smaller than the equivalent measure for a Newtonian fluid and generate a total pressure loss almost independent of the flow rate [119]. A possible explanation is the in-

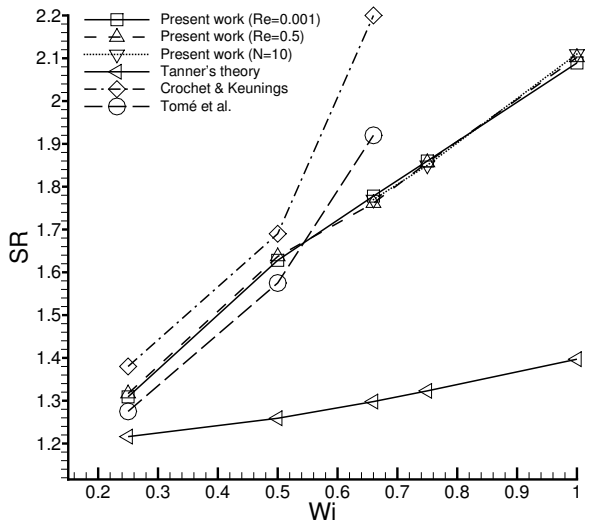

Figure 5.7: Values of the swelling ratio with increasing Wi for an Oldroyd-B fluid for $\beta = 1/9$. (bottom).

adequacy of UCM-like models in reproducing extensional flows beyond very small shear rates. Since extensional flow is predominant in the middle region of the die when the fluid is pushed from the reservoir, it might be argued that the weakness of an UCM-type model is more evident at the entry than at the exit, where the extensional process is not as dominant.

We calculate the effective exit pressure loss using the widely used formula (see Tanner [119] and Crochet and Keunings [28, 29])

$$\frac{\triangle p_{ex}}{2\tau_w} = \frac{p_w(0)}{2\tau_w} - \frac{L}{d}. \tag{5.6}$$

In Eq. (5.6) the value $p_w(0)$ is the value of the pressure at $(0, d)$. In Fig. 5.10 the relationship between the pressure loss and the Weissenberg number is shown. Calculations are close to earlier results for $Wi \leq 0.7$. The dash-dotted curve with circle symbols shows the values of the pressure drops obtained by using the alternative formula that Reddy and Tanner propose

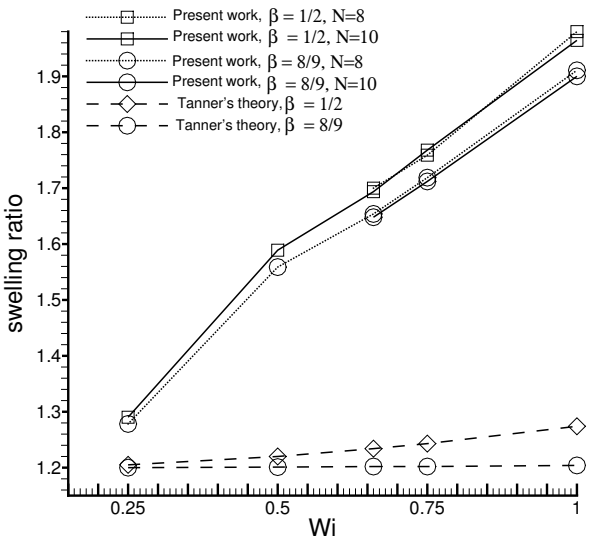

Figure 5.8: Values of the swelling ratio with increasing Wi for an Oldroyd-B fluid for $\beta = 1/2, 8/9$.

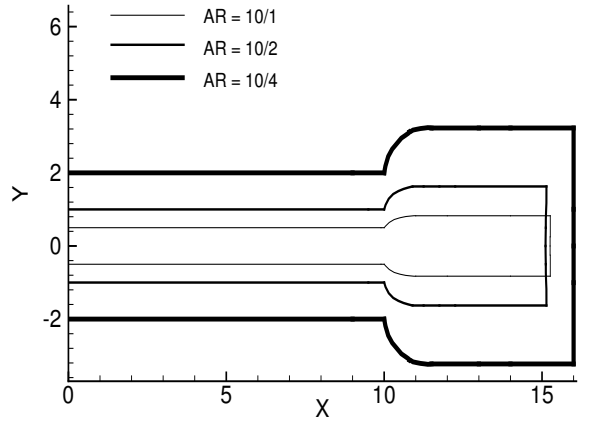

Figure 5.9: Profile of the extrudate of an Oldroyd-B fluid for different values of d, width of the slit die. Here $Wi = 0.5$.

in [103], which reads

$$\triangle p_{ex} = 0.26R_s + 0.31. \tag{5.7}$$

Tuna and Finlayson [126] also used a similar formula, although they define the quantity P_C^* as

$$P_C^* = p(0, L)/2\tau_w = 0.28R_s + 0.30. \tag{5.8}$$

This is a bit confusing, since Eq. (5.8) is equivalent to what Tanner [119] defines as the pressure at a point L units upstream from the exit. Therefore, looking at Eq. (5.6), the term L/d should be subtracted. However, at least in our calculations, this would generate a negative pressure loss for $R_s \leq 7.85$, therefore we would assume that both formulas are intended for the exit pressure loss. The values obtained by this formula are quite close to the numerical results up to $Wi = 0.75$. For values beyond $Wi = 0.75$ a sharp increase can be noticed.

The bottom box in Fig. 5.10 confirms a decreasing elastic response with increasing solvent viscosity. It is worth remarking the asymmetry of the computed pressure losses despite the symmetry of the values of β. The elastic energy is stored in the Oldroyd-B fluid through the springs connecting the dumbbell and the pressure drop is proportional to this energy. The asymmetry aforementioned then suggests that the storage of elastic energy due to increase in polymeric viscosity is larger than the loss due to dissipation when the solvent viscosity is predominant.

A measure that is often used to indicate the elastic response of a viscoelastic fluid is the first normal stress difference $N_1 = \tau_{xx} - \tau_{yy}$. In the UCM and Oldroyd-B models a zero second normal stress is predicted. It is known experimentally that polymer melts also show a non-zero second normal stress difference, but it is generally quantitatively much smaller than N_1, of the order of 10% [119, 117]. However, a non-zero N_2 has the tendency to slightly shift down the swelling ratio, as reported by Huang and Lu [54] for a class of KBK-Z integral models.

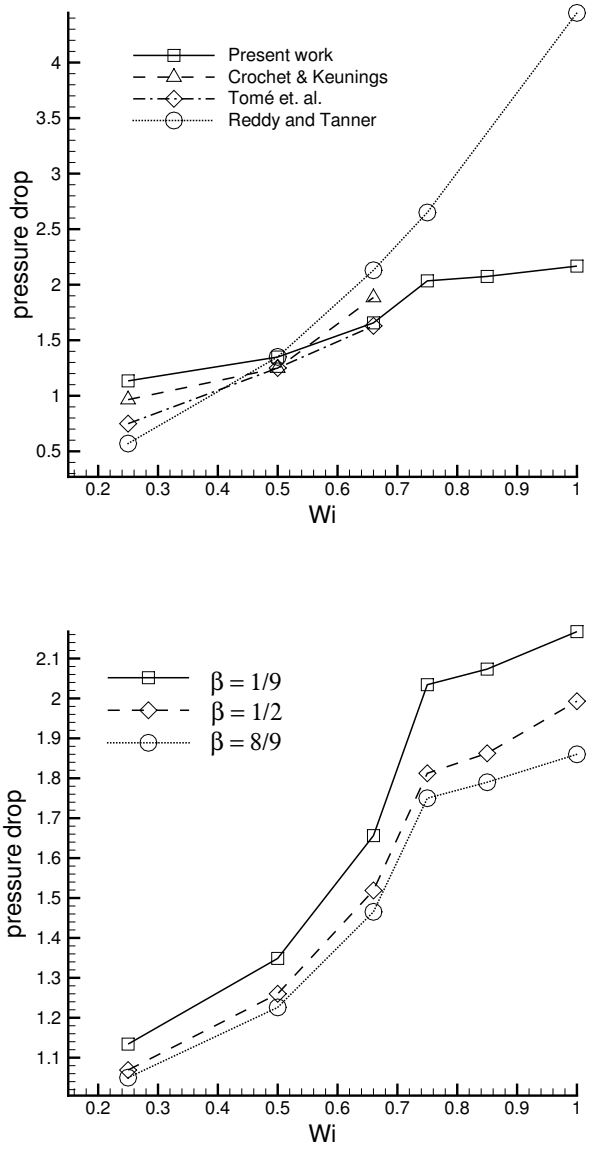

Figure 5.10: Exit pressure loss with increasing Wi for an Oldroyd-B fluid. Comparison for $\beta = 1/9$ from different sources (top) and present results for $\beta = 1/9, 1/2, 8/9$.

The profile of N_1 just after the exit is shown in Fig. 5.11 for different values of Wi and β. At fixed β, N_1 increases as Wi increases. At fixed Wi, N_1 decreases with increasing Newtonian viscosity, again confirming the correlation between the elastic response in the fluid and the viscosity ratio β.

Similar calculations have been performed using the UCM model, where the retardation time λ_2 is set to zero, therefore $\beta = \frac{\lambda_2}{\lambda_1} = 0$. The viscosity in the UCM model is entirely polymeric, therefore there is no diffusion term in the momentum equation (see Eq. (2.52)).

The location of the free surface is shown in Fig. 5.12. Again, the swelling increases with the Weissenberg number. Comparison with available results is presented in Fig. 5.13. We notice that our numerical predictions tend slightly to overestimate the values from Crochet and Keunings [29] and Tuna and Finlayson [126]. On the other hand, the corresponding values for the exit pressure loss shown in Fig. 5.14 are more consistent with the ones reported by Tanner [119].

Source \ Wi	0.15	0.25	0.30	0.50	0.60	0.75	0.90	1.05
Present work, $N = 8$	NA	1.192	NA	1.213	NA	1.248	NA	NA
Present work, $N = 10$	NA	1.192	NA	1.213	NA	1.248	NA	NA
Crochet & Keunings [28]	NA	1.169	NA	1.189	NA	1.236	NA	NA
Tuna & Finlayson [126]	1.170	NA	1.165	1.180	1.190	1.210	1.237	1.264
Bush et al. (BE) [20]	NA	1.175	NA	1.205	NA	1.240	NA	NA
Bush et al. (FE)[20]	NA	1.187	NA	1.200	NA	1.216	NA	NA

Table 5.4: Values of the swelling ratio for different values of Wi for an UCM fluid.

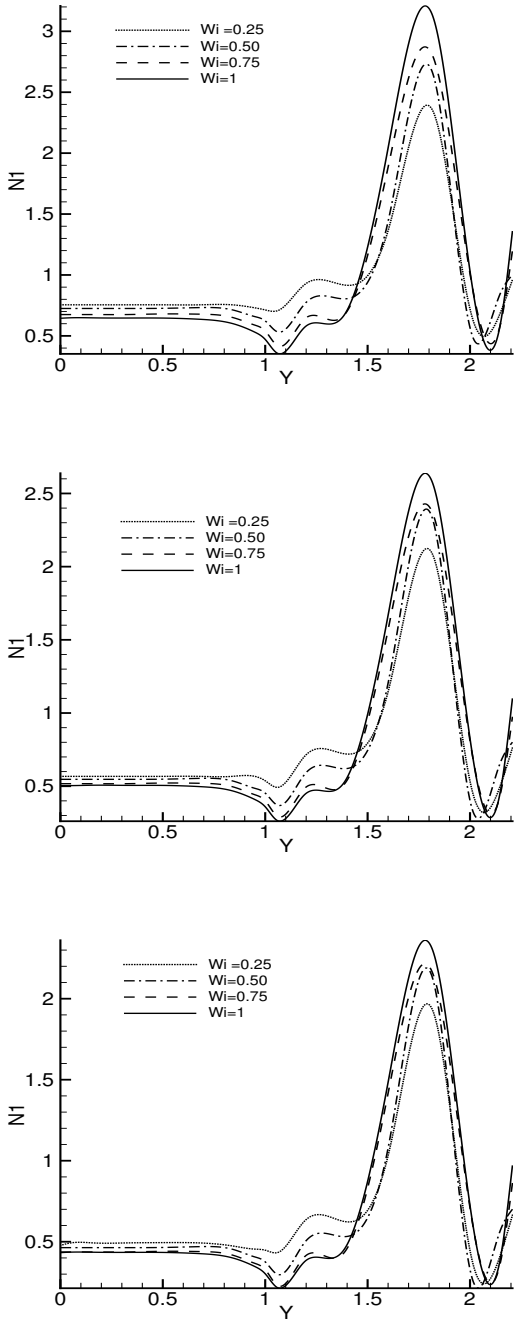

Figure 5.11: First normal stress difference at $x = 10.2$ with increasing Wi for an Oldroyd-B fluid for $\beta = 1/9$ (top), $\beta = 1/2$ (middle) and $\beta = 8/9$ (bottom). The exit is located at $x = 10$.

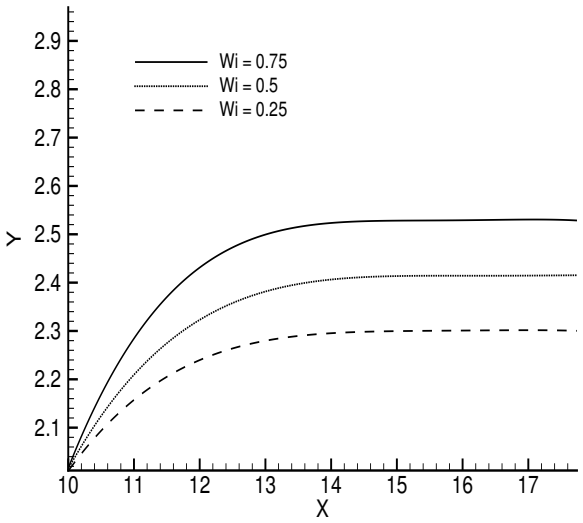

Figure 5.12: Location of the free surface with increasing Wi for an UCM fluid.

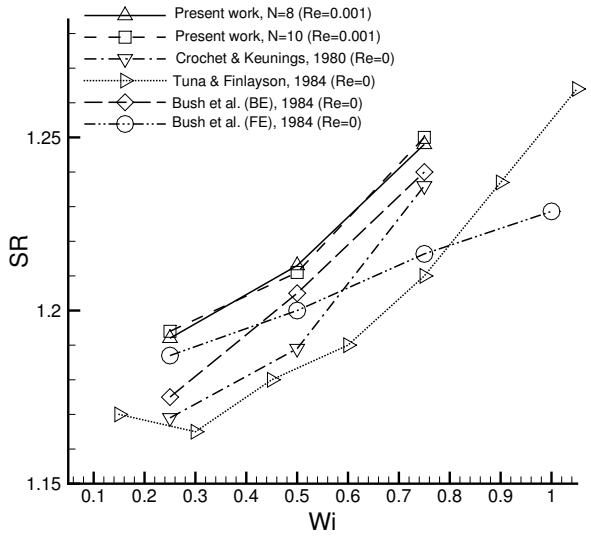

Figure 5.13: Values of the swelling ratio with increasing Wi for an UCM fluid.

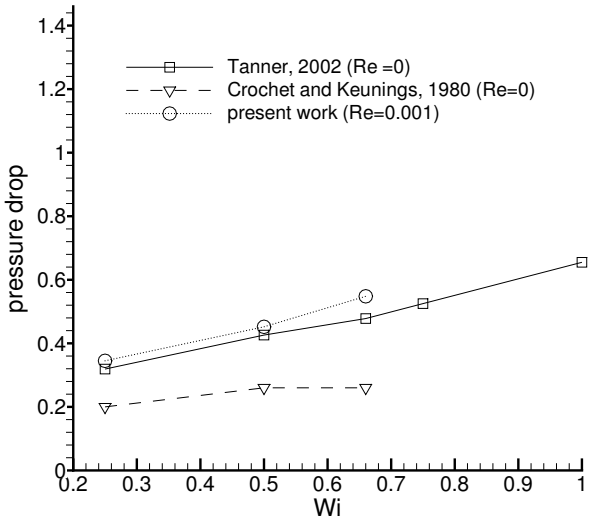

Figure 5.14: Exit pressure loss with increasing Wi for an UCM fluid.

The first normal stress difference just after the exit plane is shown in Fig. 5.15. As expected they are very similar to the Oldroyd-B profiles in Fig. 5.11, although they are smaller in absolute value. To conclude this section, a comparison between a Newtonian, UCM and Oldroyd-B fluid is shown in Fig. 5.16. Looking at these results, together with the earlier calculations, the conclusion can be drawn that the overall elastic response of an UCM fluid in extrusion is weaker than for an Oldroyd-B fluid. This is not as straightforward to understand, because in principle one would expect that, since the viscosity is completely polymeric ($\beta = 0$, so $\eta_{tot} = \eta_p$), the fluid would show a stronger elastic response than the Oldroyd-B case, especially when there seems to be agreement on the fact that, for the Oldroyd-B model, the elastic response indeed increases as β approaches 1 . In fact, a frequent assumption within the Oldroyd-B model (see Yoo and Na [142] or Tomé et al [125] for example) is to consider the effective Weissenberg number as $Wi_{eff} = (1 - \beta)Wi$, the maximum value for which is $\beta = 0$. An idea that could be put forward is that, for creeping flows, when $\beta = 0$ there is a change

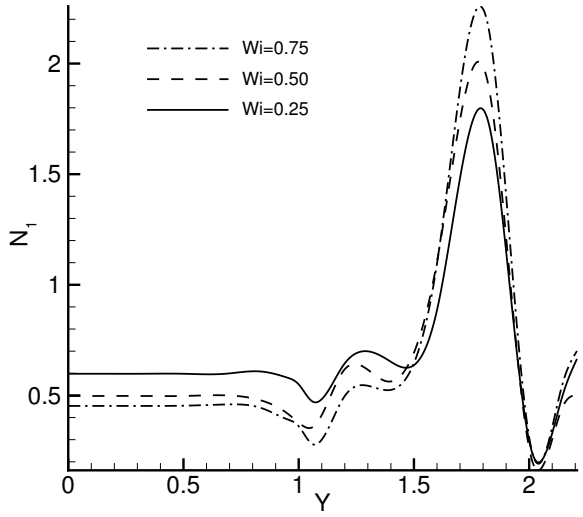

Figure 5.15: First normal stress difference at $x = 10.2$ with increasing Wi for an UCM fluid. The exit is located at $x = 10$.

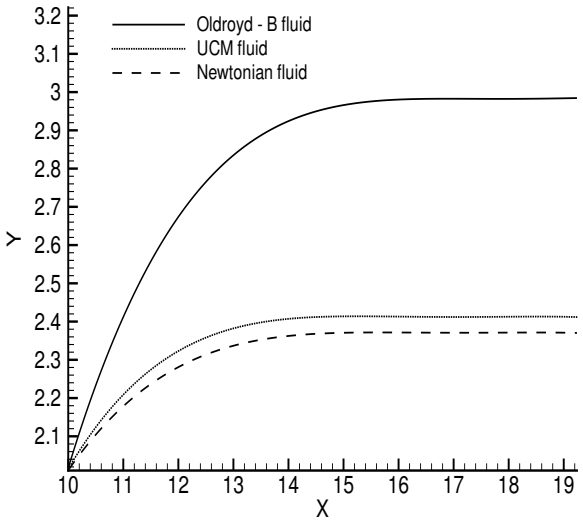

Figure 5.16: Location of the free surface for three different types of fluids. For the non-Newtonian models $Wi = 0.25$ has been used.

of type in the momentum equation, from elliptic to hyperbolic. This seems reasonable also looking at the computed swelling ratio, pressure drop and first normal stress difference shown in Fig. 5.8, 5.10 and 5.11, respectively. Even when the polymeric contribution is very small, the fluid is still far from approaching a Newtonian behaviour. This might be explained by the change in the mathematical nature of the model. A change of type of governing equations is thought to possibly cause particular mechanisms to occur in the dynamics of fluids. In particular, Joseph [60] suggested it as the reason behind delayed die-swell. However, this is outside the scope of this thesis.

5.4 Numerical simulations of polymer melts: XPP model

5.4.1 Single-mode numerical simulations

As was done in the previous section, an analysis of convergence is provided to find the most appropriate choice of M, N and Δt in terms of accuracy. The results in this section have been obtained using the single-mode XPP model with the following values of the non-dimensional parameters:

$$Wi = 1, \quad Re = 0.5, \quad \beta = 1/9, \quad q = 4, \quad r = 1, \quad \alpha = 0.025.$$

The particular value $\alpha = 0.025$ has been chosen as a consequence of the observations about multiple solutions in the viscosity reported by Inkson and Phillips [58]. In particular, the rule of thumb proposed by Verbeeten et al. [132] of setting $\alpha = 0.3/q$ seems to lead to multiple values of the transient extensional viscosity . Here we then adopt $\alpha = 0.1/q$, even if one has the certainty of finding a unique solution only if $\alpha = 0$ [58]. First, a mesh convergence study of the location of the free surface as a function of the time step, number of elements and the polynomial order is performed. This is shown in Fig. 5.17. The location of the free surface clearly converges as the size of the time step is decreased, the number of elements is increased or the order of the polynomial approximation is increased. These results suggest that the choice of discretization parameters $N = 8$, $M = 28$, and $\Delta t = 10^{-4}$ is sufficient to achieve a converged solution for this problem.

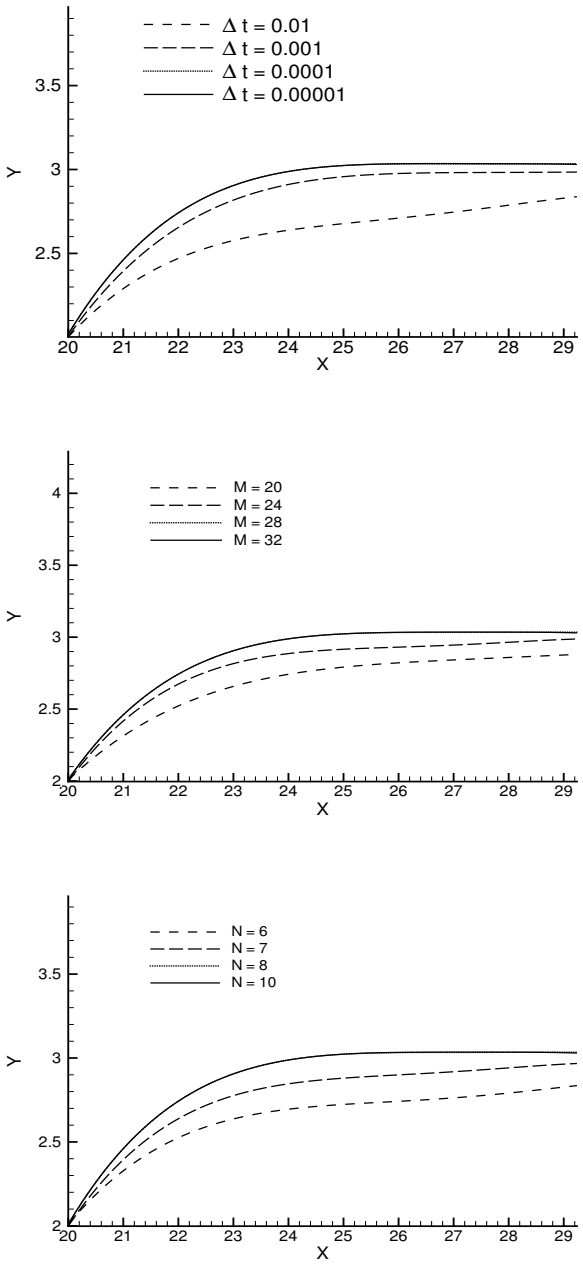

Figure 5.17: Convergence of the location of the free surface with respect to Δt with $N = 8$ and $M = 28$ (top); M with $N = 8$ and $\Delta t = 10^{-4}$ (middle); and N with $M = 28$ and $\Delta t = 10^{-4}$ (bottom).

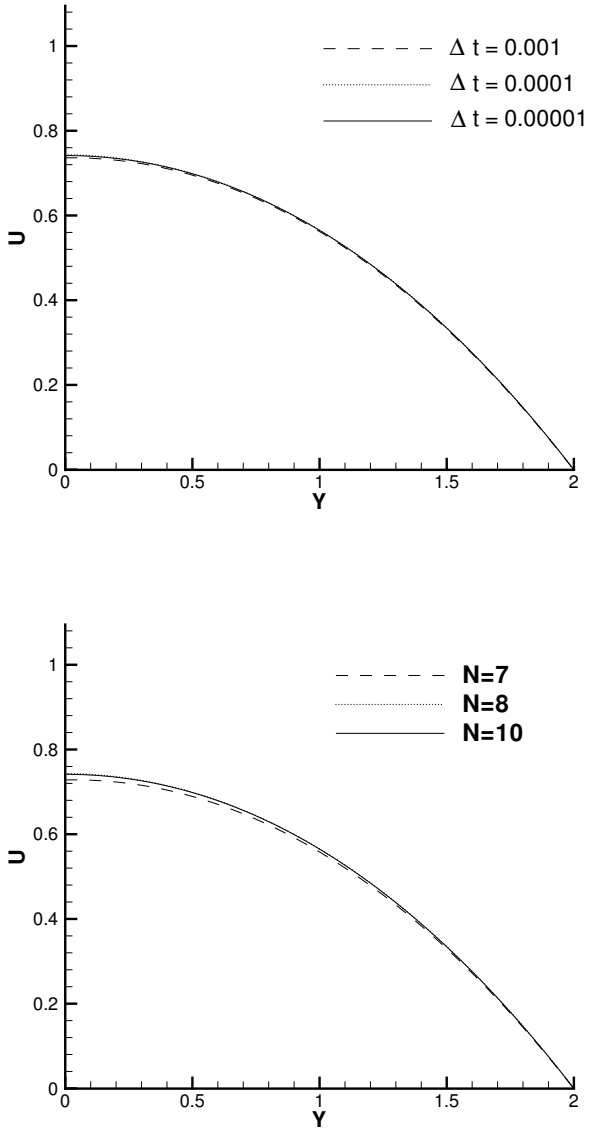

Figure 5.18: Convergence of the horizontal velocity profiles inside the die at $x = 15$ with respect to Δt with $N = 8$ and $M = 28$ (top); and N with $M = 28$ and $\Delta t = 10^{-4}$ (bottom).

Secondly, the convergence of the velocity profiles with respect to the time step and the polynomial order are investigated at different channel cross-sections. The number of elements does not play such an important role as far as the convergence of the velocity profiles are concerned. The fully developed profile in the die was achieved with as few as two elements in that region. However, more elements are required to capture the free surface location. The die exit in our simulations is located at $x = 20$. In Fig. 5.18, the profiles at the upstream location $x = 15$ are plotted for different choices of Δt and N. The profiles for $\Delta t = 10^{-4}$ and $\Delta t = 10^{-5}$ with $M = 28$ and $N = 8$ are in close agreement as are the profiles for $N = 8$ and $N = 10$ with $M = 28$ and $\Delta t = 10^{-4}$. Further downstream, the profiles tend towards a profile characteristic of plug flow. This is shown in Fig. 5.19, where the convergence with respect to Δt, M and N is investigated at $x = 28$. This figure confirms the findings shown in Fig. 5.17 and provides further evidence that converged approximations are obtained with the choice of the spatial and temporal discretization parameters: $N = 8$, $M = 28$, and $\Delta t = 10^{-4}$. All remaining results presented in this section were generated using these values.

Finally, we present contours of the horizontal velocity component, the shear stress and the axial normal stress in Fig. 5.20 for $Wi = 1$. Looking at the stress contours, in both cases very steep gradients are present around the singularity. We have followed the idea of Gerritsma and Phillips [39] and allowed the stress approximation to be discontinuous across elements. On the other hand, the velocity components are enforced to be continuous across elements. When steady state is achieved, the normal velocity has to be zero on the free surface for the no penetration condition to be satisfied. This condition is not satisfied a priori. The time dependance of the L^2-norm of velocity is plotted in Fig. 5.21. This figure demonstrates that the no-penetration condition is satisfied when steady state is attained.

5.4.2 Multi-mode numerical simulations

In the rest of this chapter numerical results derived from the prediction for the multi-mode XPP model are presented.

One of the questions we want to address in this section is whether longer

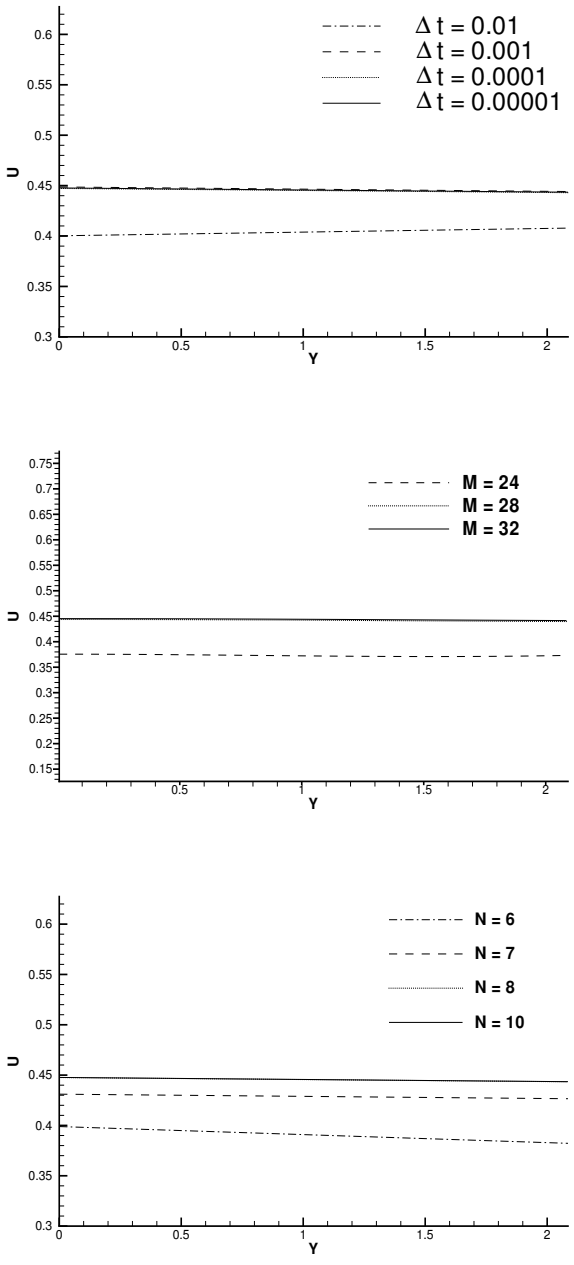

Figure 5.19: Convergence of the horizontal velocity profiles downstream at $x = 28$ with respect to Δt with $N = 8$ and $M = 28$ (top); M with $N = 8$ and $\Delta t = 10^{-4}$ (middle); and N with $M = 28$ and $\Delta t = 10^{-4}$ (bottom).

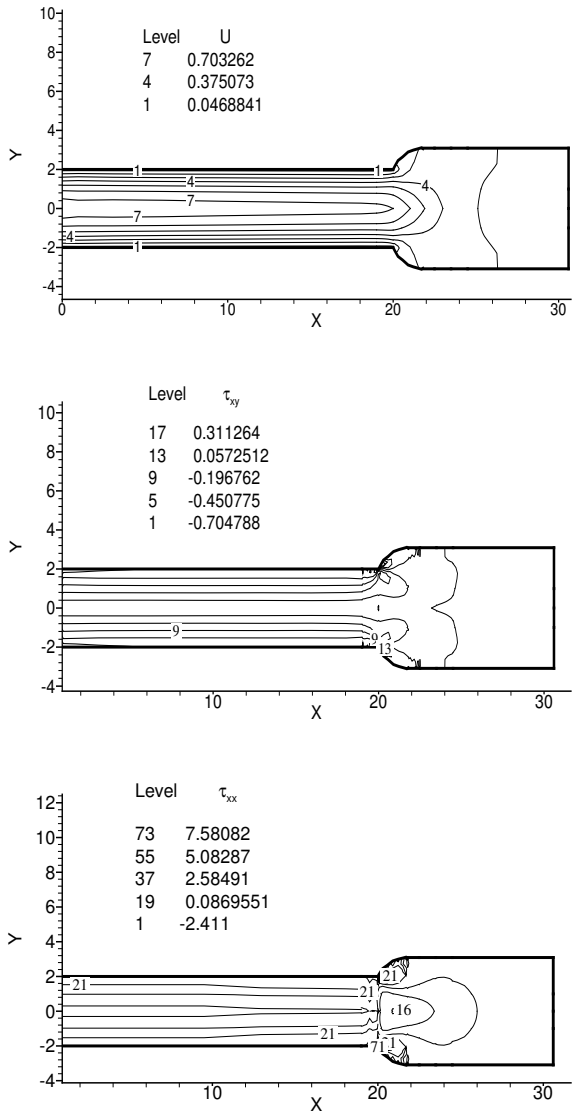

Figure 5.20: Contour plots of the horizontal velocity (top), shear stress (middle), axial stress (bottom) with $N = 8$, $M = 28$, $\Delta t = 10^{-4}$ obtained using the single-mode XPP model with $Wi = 1, \quad Re = 1, \quad \beta = 1/9, \quad q = 4, \quad r = 1, \quad \alpha = 0.025$..

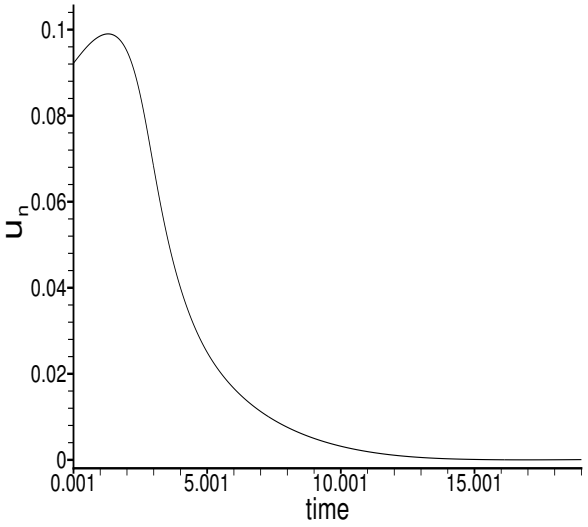

Figure 5.21: L^2-norm of the normal velocity on the free surface against time.

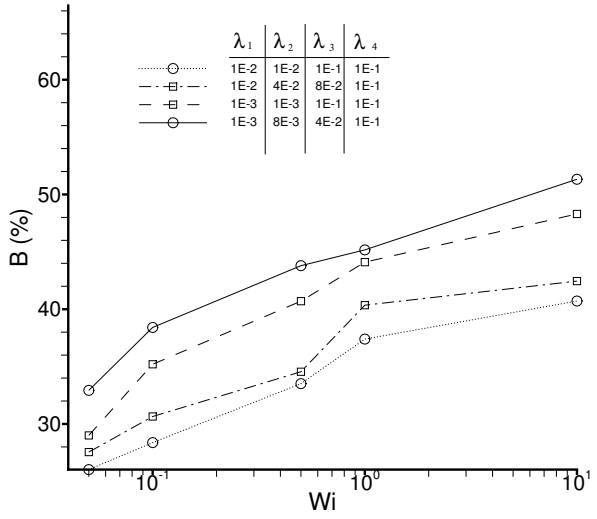

Figure 5.22: Dependence of swelling ratios on the Weissenberg number for different sets of narrow discrete relaxation spectra.

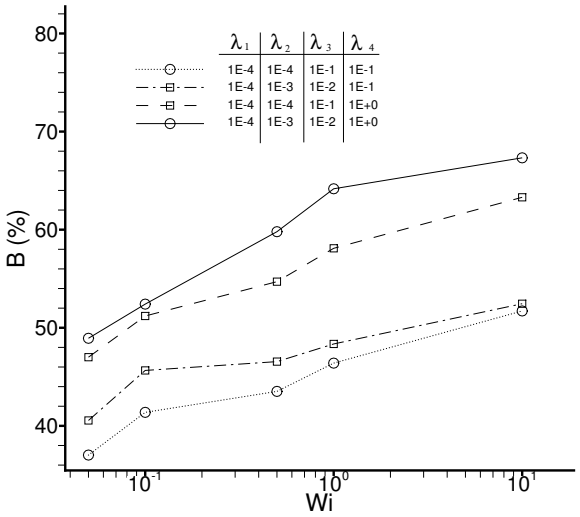

Figure 5.23: Dependence of swelling ratios on the Weissenberg number for different sets of broad discrete relaxation spectra.

relaxation times in the multi-mode XPP model can be associated with polymer melts with a high molecular weight tail. Another related question is whether a broad discrete relaxation spectrum in the multi-mode XPP model can be identified as an indicator of the polydispersity of the melt. In the case of models based on elastic dumbbells, such as Oldroyd B or FENE, this seems more readily linked to the idea of elastic springs connecting the dumbbells. Moreover, in these models the purely elastic behaviour of the material is almost entirely represented by the relaxation times. In more sophisticated models, such as the XPP model, factors like the anisotropy of the chains and the withdrawal of the branches into the tubes are taken into account. It is of great importance to gain a deeper insight into the different characteristics of a material that such parameters might represent from a global perspective and to relate these to swelling behaviour in the extrudate swell problem.

It seems to be generally accepted that for materials of comparable elasticity, those which are more polydisperse tend to generate larger swelling

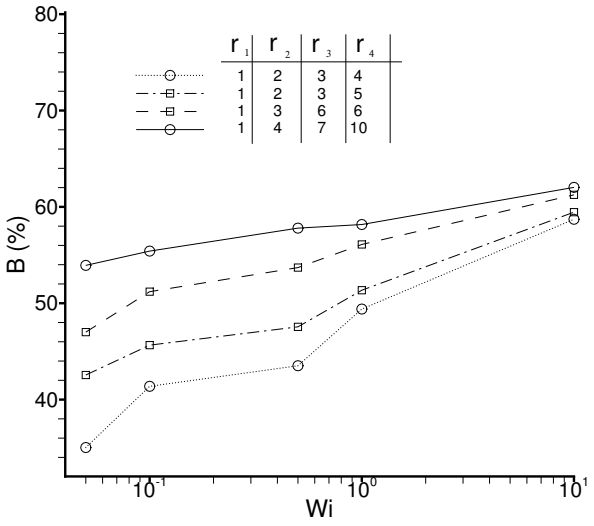

Figure 5.24: Dependence of swelling ratios on Weissenberg number for different sets of values of r_i, $i = 1, \ldots, 4$, with $\lambda_1 = 10^{-3}$, $\lambda_2 = 10^{-2}$, $\lambda_3 = 10^{-1}$, $\lambda_4 = 1$

ratios when extruded. This behaviour has been observed experimentally by Yang et al. [138] for linear LDPEs, for example, and noted by Den Doelder and Kooopmans [32]. However, Den Doelder and Kooopmans [32] argue that standard polydispersity indices, such as M_w/M_n, where M_w and M_n are the weight average and number average molecular weight, respectively, are not appropriate for predicting swelling ratios because they are based on the molecular weight distribution rather than the rheological properties of the material. They proposed an alternative indicator based on higher average molar moments, which is monotonically related to the recoverable compliance via the plateau modulus, that could be used to predict the effect of polydispersity due to elasticity.

All the results shown in this section have been generated using the XPP model with four modes. The dependence of the swelling ratio on the Weissenberg number, based on average relaxation time, is shown in Figs. 5.22 and 5.23 for narrow and broad ranges of discrete relaxation spectra, respec-

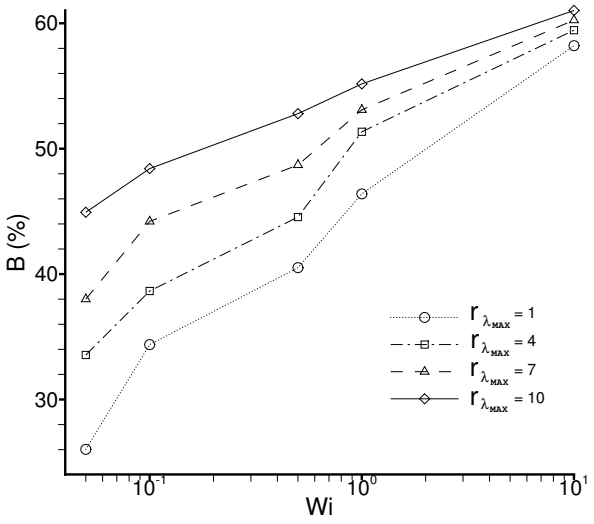

Figure 5.25: Dependence of swelling ratios on Weissenberg number for different values of $r_{\lambda_{max}}$, with $\lambda_1 = \lambda_2 = \lambda_3 = 10^{-3}$, $\lambda_4 = 5 \times 10^{-2}$.

tively. For materials which possess the same longest relaxation time, larger swelling ratios are obtained for those materials whose discrete spectra are broader. The increase in swelling ratio due to a broader relaxation spectrum is much less than the increase due to a larger value of the longest relaxation time. This is to be expected, since the elasticity of a polymer depends on the value of the longest relaxation time much more strongly than on the shorter ones. This explains the jump between the top two and the bottom two curves in Fig. 5.23.

Another interesting outcome is revealed from the numerical simulations on investigation of different ranges of the parameters, r_i, $i = 1, \ldots, 4$, the ratios of the backbone orientation and stretch relaxation times for each of the modes. In Fig. 5.24 the effect of orientation is highlighted. For a fixed value of the Weissenberg number, larger swelling ratios are predicted for larger values of r_i. It seems reasonable to argue that orientation does influence the capacity for elastic recoil in the melt; a longer relaxation time associated with the orientation of the backbone leads to an overall higher elasticity of

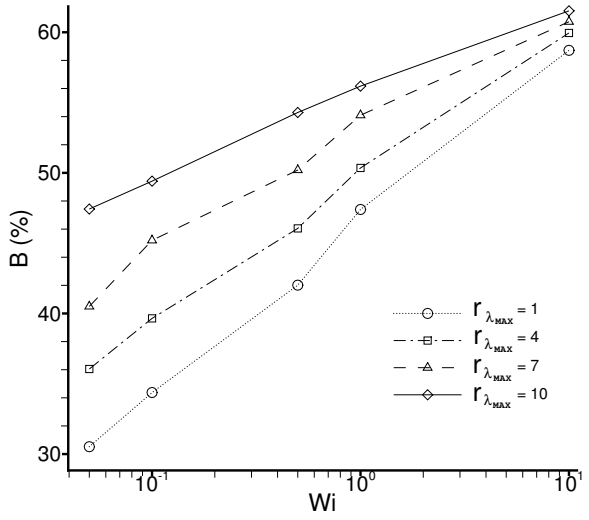

Figure 5.26: Dependence of the swelling ratios on Weissenberg number for different values of $r_{\lambda_{max}}$, with $\lambda_1 = \lambda_2 = \lambda_3 = 10^{-3}$, $\lambda_4 = 10^{-1}$.

the melt. However, as the range of r_i broadens, and the maximum value increases, the effect of increasing swelling ratio with Weissenberg number is reduced. We believe that this effect might be related to the increased anisotropic behaviour of the model.

On the other hand, as the Weissenberg number increases, the effect of the orientation relaxation time on elastic recoil seems to weaken, as can be seen by the convergence of the symbols in Fig. 5.24 as one moves from left to right. This feature may be due to the counteracting effect of an overall larger flow rate. An increase in fluid inertia partially counteracts the effect of larger values of r_i. At higher flow rates, the molecules are literally subject to stronger convective forces which impels them to align with the streamlines, thereby enhancing the anisotropy of the melt. Once the chains have become aligned with the streamlines, they will keep their preferential direction. Hence, the relaxation process related to orientation will be complete, leaving the chains only the possibility of stretch. Therefore, an increase in flow rate seems to amplify the elasticity effects due to stretch and dampens

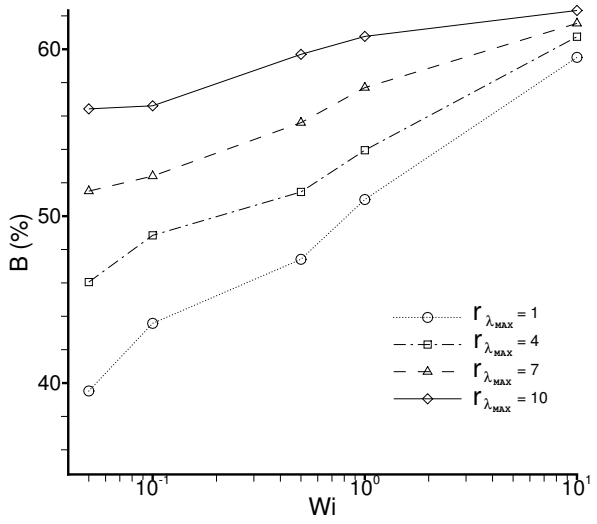

Figure 5.27: Swelling ratios plotted against Wi for different values of $r_{\lambda_{max}}$, with $\lambda_1 = \lambda_2 = \lambda_3 = 10^{-3}$,$\lambda_4 = 1$.

the effects due to orientation. This is in fact what the modelling of the orientation and stretch predicts in the expression for the extra function in Eq. (2.80). The backbone tube orientation dominates the flow process at low rates, while the stretch takes over at higher rates.

In Figs. 5.25-5.27, where a discrete bimodal relaxation spectrum is used, a similar reduced effect of the orientation relaxation time on the swelling ratio is predicted as the Weissenberg number increases. The bimodal spectrum has three modes associated with the shortest relaxation time, and a fourth mode associated with the longest. The two distinct relaxation times are increasingly separated by one, two or three orders of magnitude in Figs. 5.25, 5.26, and 5.27, respectively. The reason for this particular investigation was to study the effect of adding a high molecular weight tail to a much lighter melt. An experimental investigation of this effect has been carried out by Zhu and Wang [144], who monitored the extrusion of 100 K/1.5 M polybutadienes. The swelling ratios have been measured for increasing concentrations of 1.5 M, from 0% to 5%. The results reported in Fig. 5.28

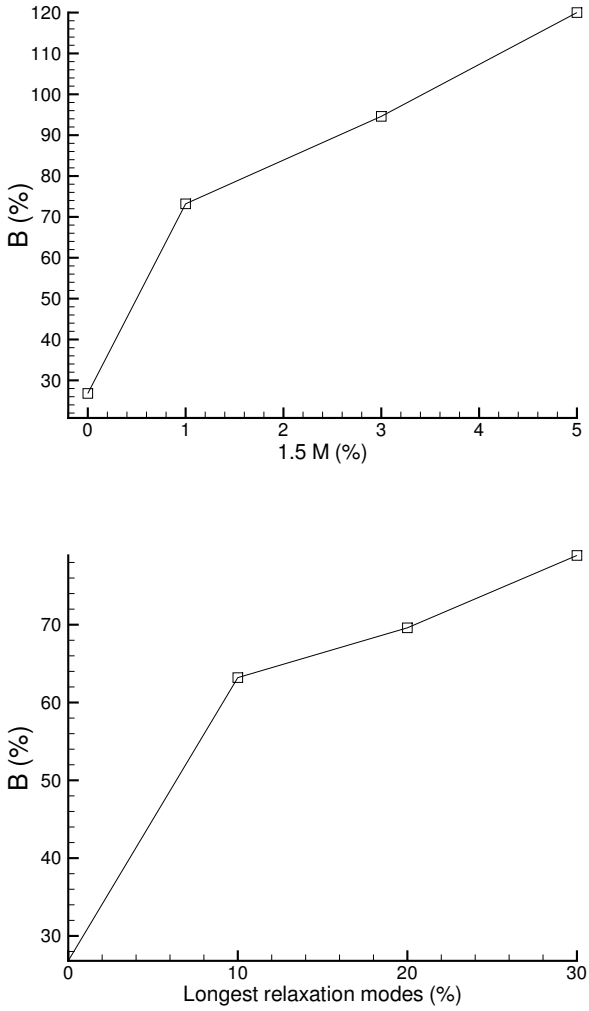

Figure 5.28: Dependence of the swelling ratios on the percentage of high molecular weight melt: experimental (top) and numerical (bottom).

clearly show an increase in the swelling ratios with increasing percentage of the high molecular weight tail. Based on the experimental findings, a sensible approach in the numerical simulations is to increase the number of modes associated with the longest relaxation time. A qualitative comparison between numerical simulations and experiments is shown in Fig. 5.28. The qualitative agreement between the two is very good. However, there were insufficient experimental data available for the blend to fit the parameters in the XPP model in order to perform a quantitative comparison. In the numerical simulations, ten modes have been used. The number of modes associated with a relaxation time $\lambda_{0b,i} = 1$ varies from 0 to 3. The jump in the swelling ratio, as the concentration is increased from 0% to 1% in the experimental results is clearly due to an increase in the longest relaxation time. However, an increase in the swelling ratio is also reported as the concentration is increased further. As the concentration is increased, the longest relaxation time remains the same but an increasing number of modes $(1, 2, 3)$ are associated with it. Clearly further and deeper investigation of this issue is required. We chose not to superpose the experimental and numerical results because this is a qualitative comparison.

For the sake of completeness, we performed systematic simulations over five decades in the shear rate. The results are shown in Table 5.5. They have been generated keeping the relaxation times in the range $10^{-4} \leq \lambda_{b0,i} \leq 10^{-2}$. Consequently, the Weissenberg number varied as $10^{-3} \leq Wi \leq 10$. In the case of prevalence of linear modes, no convergent solutions were achieved for $\dot{\gamma} = 10$. This is a fairly expected outcome, since the value $Wi = 10$ is already reasonably high. Once again we remark how this is still much higher than the corresponding critical Weissenberg number for UCM-tpye models, which is around 1.5. However, it is not entirely clear why, in the case of branched (or mostly branched) modes, a solution was obtained. The only idea we can put forward is that the exponential term in the extra function, $e^{\frac{2}{q}(\lambda-1)}$, tends to be stabilized for higher values of q. If one linear mode is present, it is reasonable to believe that a sort of amplification might occur, causing the numerical code to break down. However, no systematic analysis has been performed at this regard, being the exact value of a critical Weisseneberg number for the numerical calculations outside the scope of this

Modes \ *Shear Rate*	10^{-1}	1	10^{1}	10^{2}	10^{3}
1 mode, L	28.918%	39.550%	50.468%	62.354%	*B.D.*
1 mode, B	32.628%	42.593%	54.899%	65.553%	70.489%
2 modes, LL	28.541%	39.985%	51.547%	64.278%	*B.D.*
2 modes, BB	32.785%	42.193%	55.023%	66.254%	*B.D.*
2 modes, LB	36.244%	45.409%	58.829%	68.486%	*B.D.*
3 modes, LLL	28.126%	40.210%	51.286%	63.457%	*B.D.*
3 modes, BBB	32.012%	42.245%	54.365%	65.553%	71.554%
3 modes, LLB	36.987%	45.745%	59.685%	68.798%	*B.D.*
3 modes, BBL	36.777%	45.875%	58.145%	69.045%	*B.D.*
4 modes, LLLL	28.887%	40.014%	50.869%	64.869%	*B.D.*
4 modes, BBBB	32.111%	43.494%	54.869%	67.024%	71.214%
4 modes, LLBB	36.985%	46.109%	58.045%	68.789%	*B.D.*%
4 modes, LLLB	36.324%	46.198%	58.178%	67.125%	*B.D.*
4 modes, LBBB	37.244%	45.855%	58.689%	68.486%	*B.D.*

Table 5.5: Summary of the values of the swelling ratios for different values of the shear rate.

thesis.

Another observation which can be made looking at the results in Table 5.5 is that, at a fixed shear rate, the largest swelling ratios are obtained when linear and branched mode are allowed in the melt. However, such a difference in the calculated values of the swelling ratio tends to narrow as the shear rate increases. In this regard, it might be useful to briefly analyze the experimental work of Liang [70], who tested an LDPE/LLDPE (Linear LDPE molecule with no branching) melt. The highest swelling ratios are reached when the two components in the melt are present in roughly equal parts. The LLDPE increases the elastic storage mechanism in the blend, and this is the reason why the swelling ratios increase from pure LDPE to a 50% blend of LDPE with LLDPE, then decrease. When the LLDPE is in the continuous phase, its much larger viscosity leads to higher viscous dis-

sipation as a consequence of the large shear at the wall. This explains the decrease in elasticity and the enhanced swelling ratios when the proportion of LLDPE in the blend is more than 50%. However, it is not completely clear why there is an increase in elasticity when LLDPE is added from 0% to 50%. In this range, the elasticity due to the branched LDPE clearly diminishes. Moreover, the viscous dissipation due to the shear deformation, even if not as large as for LLDPE in its continuous phase, still increases with the addition of LLDPE up to 50%. This would explain why the elasticity is generally higher when the LDPE is in its continuous phase, but not at the peak at 50%. On inspection of the curves in Fig. 6 in [70], it can be seen that, in the region where $0\% \leq$ LLDPE (%) $\leq 50\%$, they flatten with increasing shear rate. On the other hand, the slope of the three curves is the same in the region where $50\% \leq$ LLDPE (%) $\leq 100\%$. It is likely that the effect of the LLDPE on the entanglement molecules in the blend is responsible for the increasing swelling ratio in the LDPE continuous phase. A long, linear molecule and a branched one entangle more easily than two branched molecules, but at the same time the latter combination supports more strain than the former. This might explain why the increase in elastic energy provided by these entanglements is more visible at lower shear rates with an increase of linear molecules. When the rate increases, such entanglements are more readily untied by convective constraint release and the increase in elasticity with the percentage of linear molecules is less evident. Eventually, such an increase in the elastic energy is lost when the LLDPE is in its continuous phase. Unfortunately not enough data were found to characterize the blend and therefore no quantitative comparison could be performed.

However, these results are also in general agreement with the numerical simulations of Clemeur et al. [26], who used the double convected version of the pom-pom model (DCPP) to study the flow in a capillary rheometer. They performed finite element computations for four different DCPP models. Each model had four modes. Results showed that the highest swelling ratio by far was achieved using the model with two linear and two branched modes, which resembles a balanced blend of LDPE and LLDPE. Further-

more, the purely linear DCPP had the lowest swelling ratio, which was just below that for the four-mode branched model, as observed by Liang [70, 71] in his experiments.

Chapter 6

Extrusion of Viscoelastic Fluids: Comparison With Experiments

This concluding chapter is an attempt to provide a quantitative analysis of the extrusion of an XPP fluid and put it in the context of experimental research. Several materials are characterized, and the corresponding parameters fitting the XPP model are calculated. Comparison between numerical and experimental results are presented. A discussion on a possible identification of the effects of polydispersity and orientation on extrusion is also proposed.

6.1 Introduction

In an early experimental paper, Batchelor et al. [7] analyzed the extrusion of the depolymerized natural rubber Lorival $R25$. An increase of the swelling ratio with shear rate was evident, varying between 50% and 200%. More experimental work has been carried out in the last decade, mainly focusing on Low and High Density PolyEthylenes (LDPE and HDPE, respectively), and their blends. The macromolecules present in these materials can be synthesized.

A comparison between numerical simulations and experiments has been performed by Huang and Lu [54], in which they focused on the influence of the relaxation properties of LDPE and extrudate swell. The nonlinear K-BKZ integral constitutive model, in which the stress is related to the rate of strain through functions of the invariants of the Cauchy and Finger strain tensors, was used in the simulations. A fading memory function is present in the K-BKZ model, together with a damping function which describes how the memory of the fluid fades. Four different damping functions were analyzed by Huang and Lu [54]. The main outcome was that the model with the single exponential Wagner damping function generally performed better than the others. The explanation for this is that the Wagner damping function captures more accurately the dependence of the memory of the fluid on the strain history. The model possesses a nonzero second normal stress difference, which was confirmed to be responsible for a reduction in the overestimation of the swelling ratios. Decreasing swelling with increasing length of the die was also reported. The results by Huang and Lu [54] are added in this chapter to the ones from Russo and Phillips [110]. Moreover, the results from several works about the relationship between the molecular structure and the linear rheology of different melts (e.g. [129, 128, 130, 131, 21]) have been analyzed. The outcome, explained in Section 6.3.1, strengthens the power of the XPP model to perform quantitative predictions for branched polymers. On the other hand, is less optimistic than the findings in [110] concerning the possibility of recovering information on the molecular structure of the material by simply looking at the parameters fitting the model.

A capillary rheometer is probably the most common tool to extrude polymers. In this instrument, the fluid in a reservoir is forced into a die of much smaller diameter, usually by means of a piston. This entry flow creates a pressure drop between the entrance and the exit of the die. The analysis of flow within and beyond the capillary provides information about the rheological properties of the polymer.

Liang [69] used such a rheometer to test different polymeric materials. He proposed a power law dependence of the shear viscosity on the shear rate

and tested his theory on four different thermoplastics including HDPE and LDPE. His predictions are consistent with the experiments over a relevant range of shear rates ($10s^{-1} < \dot{\gamma} < 10^3 s^{-1}$). The most visible non-Newtonian effects are present in the HDPE melt. This type of polymer melt has also been used by Liang [68] to validate an equation relating swelling ratio to pressure drop. In the analysis, the die is assumed to be sufficiently long, so that the pressure drop at entry can be neglected, and the flow is assumed to be inertialess. The experiments have been performed over the range of shear rates $185s^{-1} < \dot{\gamma} < 685s^{-1}$. The agreement is quite good especially at high shear rates, where the assumption regarding the entry pressure becomes less significant.

As we already mentioned, Liang [70] tested an LDPE/LLDPE (Linear LDPE molecule with no branching) melt. We have already discussed the results in terms of swelling ratios at the end of the previous chapter. We can also add in this regard that clear patterns can be seen in the pressure drop at the exit, especially for low shear rates. This suggests that when viscosity effects become more significant, the shear properties of the different components of the melt produce distinct behaviour. The swelling ratio becomes less dependent on both the entry pressure drop and the shear stress at the wall, as the percentage of LLDPE in the melt increases. There is also a reduced shear-thinning effect when there is a lower percentage of branched molecules present in the melt. The highest swelling ratios are reached when the two components in the melt are present in roughly equal parts.

Further experimental work has been carried out by Liang [71], who also tested two different tyre compounds. The compounds are natural rubbers; one is filled with calcium carbonate, the other with carbon black. The carbon black filled compound generally exhibited a higher response to shear effects, including higher values of shear stress at the wall in the die. The reason is that the carbon black particles undergo radical polymerization forming aggregates which reduce the elastic response and increase the viscous response. For the same reason, swelling ratios are lower than the calcium carbonate filled rubber. The entry flow from the reservoir is a highly extensional flow.

The elastic energy stored from this extension has also been taken into account, and the swelling ratios measured against it. If the die is not long enough, the compounds show a high dependence on the entry strain energy. This indicates that long dies are required if the extensional process in the capillary rheometer is to be fully developed before swelling takes place. In fact, there is general agreement that the swelling ratio decreases as the length of the die increases, until it reaches a plateau. The reason is that the profile at the entry is far from being fully developed, due to the highly extensional effects caused by the contraction in the rheometer. Such effects gradually decrease along the die, and eventually, if the die is long enough, disappear, leaving a genuine fully developed profile, where the elastic stress due to the extension is completely relaxed. At this point, the elasticity of the fluid becomes independent of the length, and so does the corresponding value of the swelling ratio.

The dynamic interaction between the particles and the solvent is clearly at the core of the fluid mechanics of solutions and melts. Experiments frequently demonstrate the important processes taking place at the interface between the particles and the solvent. The free radical behaviour discussed by Liang [71] is a good example. Even more relevant, however, are the experiments that have been performed by Dangtungee et al. [31] in which they investigated isostatic polypropylene (IPP) filled with uncoated and coated calcium carbonate in a capillary extrusion. The melts behave in a similar fashion when the concentration is kept to around 5%. However, when it is increased to 25%, the response to shear is more evident in the uncoated melt. This is not unexpected due to the higher friction at the particle interface. On the other hand, the presence of coated nanoparticles leads to a larger shear-thinning effect since they act as a lubricant in the blend, and subsequently there is less resistance to shear. Swelling and the overall elasticity of the blend is generally reduced by the addition of particles, so long as the shear rate is large enough. When the added particles are coated, the decrease in elasticity is due to the same lubrication effect responsible for the shear-thinning of the fluid. On the other hand, if uncoated particles are added, it may be that elasticity due to the orientation is particularly reduced, be-

cause the anisotropy of the blend would be aided by the calcium molecules. This seems reasonable especially looking at low shear rates, where elasticity increases with the addition of particles. In this case, when convection does not strongly contribute to the orientation of the molecules, they are likely to aggregate. Hence, by increasing the percentage of filler without permitting sufficient dispersion, the aggregation adds elasticity to the blend, and this is more evident for the uncoated filled melt.

Dangtungee et al. [30] also performed experiments on a blend of LDPE and ethylene octene copolymer (EOC). The largest values of the shear and extensional viscosities are obtained for the most concentrated blend (75% LDPE, 25% EOC). It also seems that the amount of swelling the blends experience is very sensitive to the aspect ratio; no clear pattern is observed apart from the longest die for which the aspect ratio is 15. On the other hand, the rheological properties of the melt seem independent on the aspect ratios. This confirms the observation made earlier that, in a capillary rheometer, the swelling ratio is highly dependent on the process of storing the strain energy subsequent to the highly extensional flow in the contraction of the reservoir. One further conclusion can be drawn. For the longest die, the swelling ratio increases with concentration at low shear rates. At high shear rates, the inverse trend is observed. This seems to suggest that when the molecules are allowed to aggregate, there is a gain in the elastic nature of the melt. Conversely, if they are dispersed, the effect is to reduce the elasticity and increase the rigidity and viscosity of the material. We remark that all the polymers analyzed do not form cross-links. If that was the case, aggregation has the opposite effect since cross-links generate permanent memory in the fluid. This would result in an increase in the plasticity of the material, which counteracts the process of elastic stress recovery.

6.2 Characterization of the materials

Five materials have been characterized for comparison with experimental results. Unfortunately, there is a dearth of experimental results on extrusion of polymeric liquids suitable for comparison with numerical simulations. The

materials which are usually extruded are not sufficiently characterized to fit nonlinear models (quite often not even the dynamic moduli $G'(\omega)$ and $G''(\omega)$ are available). On the other hand, for materials which have been extensively characterized, such as the DSM Stamylan LD 2008 XC43 or the BASF Lupolen 1810H (see for example Verbeeten et al. [132, 133]) no experimental results on extrusion have been found.

The parameters in the multi-mode XPP model were determined using Reptate, which is an open source software package for viewing, exchanging and analyzing rheological data. It was developed as a part of the Microscale Polymer Processing (μPP^2) project. Five polymers have been analyzed: two linear LDPEs, LLDPE-H and LLDPE-L, which have been extruded experimentally by Yang et al. [138], and the IUPAC-LDPE samples A, B and C characterized by Meissner [80]. The experimentally measured storage and loss moduli reported in these papers are used to calculate the linear viscoelastic parameters. Then the nonlinear parameters in the XPP model are determined using the stress-strain curves in the case of the linear LDPEs and the transient stress data for the IUPAC samples. The model parameters are reported in Tables 6.1 and 6.2. The linear viscoelastic has also been implemented in a multi-mode version of the Oldroyd-B model with comparison purpose.

6.3 Results

In this final subsection we present some quantitative comparisons with experimental results in the literature.

A few remarks need to be made at this stage. Unfortunately, no polydispersity indices are reported by Meissner [80] for the IUPAC samples. However, the measurements reported by Meissner [80] show that sample A has a molecular weight which is an order of magnitude higher than both samples B and C. Moreover, Meissner [80] describes sample A as being more polydisperse than B and C. These latter samples seem to possess the same degree of polydispersity.

With reference to Table 6.1, we note that, in the case of the IUPAC-LDPE

SAMPLE	Linear parameters			XPP model	
	i	$G_{0,i}(Pa)$	$\lambda_{b0,i}$	q_i	r_i
IUPAC-LDPE sample A from Meissner [80]	1	$2.950 \cdot 10^{0}$	$1.620 \cdot 10^{2}$	22	1.0000
	2	$9.1792 \cdot 10^{2}$	$3.239 \cdot 10^{1}$	2	1.3750
	3	$2.999 \cdot 10^{3}$	$6.478 \cdot 10^{0}$	1	2.5000
	4	$5.0663 \cdot 10^{4}$	$1.295 \cdot 10^{0}$	1	1.8750
	5	$1.1382 \cdot 10^{5}$	$2.590 \cdot 10^{-1}$	1	2.5000
	6	$4.4792 \cdot 10^{5}$	$5.1798 \cdot 10^{-2}$	1	2.5000
	i	$G_{0,i}(Pa)$	$\lambda_{b0,i}$	q_i	r_i
IUPAC-LDPE sample B from Meissner [80]	1	$2.9500 \cdot 10^{2}$	$2.2056 \cdot 10^{1}$	4	1.1385
	2	$1.6410 \cdot 10^{3}$	$8.2552 \cdot 10^{0}$	1	3.0000
	3	$2.1522 \cdot 10^{4}$	$3.0897 \cdot 10^{0}$	1	2.5000
	4	$5.5578 \cdot 10^{4}$	$1.1564 \cdot 10^{0}$	1	3.0000
	5	$1.0787 \cdot 10^{5}$	$4.3281 \cdot 10^{-1}$	1	3.5000
	6	$1.4384 \cdot 10^{5}$	$1.6199 \cdot 10^{-1}$	1	4.0000
	i	$G_{0,i}(Pa)$	$\lambda_{b0,i}$	q_i	r_i
IUPAC-LDPE sample C from Meissner [80]	1	$5.8140 \cdot 10^{2}$	$3.3056 \cdot 10^{1}$	4	3.1385
	2	$1.6410 \cdot 10^{3}$	$6.1278 \cdot 10^{0}$	2	2.0000
	3	$1.6139 \cdot 10^{4}$	$2.4297 \cdot 10^{0}$	1	2.5000
	4	$6.4180 \cdot 10^{4}$	$1.0145 \cdot 10^{0}$	1	3.0000
	5	$1.0787 \cdot 10^{5}$	$6.8312 \cdot 10^{-1}$	1	2.0000
	6	$1.2456 \cdot 10^{5}$	$2.1784 \cdot 10^{-1}$	1	2.0000

Table 6.1: XPP parameters for different polymer melts.

SAMPLE		Linear parameters		XPP model	
	i	$G_{0,i}(Pa)$	$\lambda_{b0,i}$	q_i	r_i
LLDPE-L from Yang et al. [138]	1	$9.0957 \cdot 10^1$	$1.7437 \cdot 10^1$	2	5.1385
	2	$4.8454 \cdot 10^2$	$5.5965 \cdot 10^0$	2	4.0000
	3	$6.7390 \cdot 10^3$	$1.7962 \cdot 10^0$	1	3.5000
	4	$1.5205 \cdot 10^4$	$5.7648 \cdot 10^{-1}$	1	3.0000
	5	$8.6266 \cdot 10^5$	$1.8502 \cdot 10^{-1}$	1	2.0000
	6	$5.2947 \cdot 10^5$	$5.9382 \cdot 10^{-2}$	1	2.0000
	i	$G_{0,i}(Pa)$	$\lambda_{b0,i}$	q_i	r_i
LLDPE-H from Yang et al.[138]	1	$2.8770 \cdot 10^0$	$1.8382 \cdot 10^1$	5	4.3750
	2	$1.0228 \cdot 10^2$	$5.5864 \cdot 10^0$	4	3.5000
	3	$1.7517 \cdot 10^4$	$1.6977 \cdot 10^0$	2	3.5000
	4	$1.4386 \cdot 10^5$	$5.1594 \cdot 10^{-1}$	1	3.0000
	5	$1.5335 \cdot 10^5$	$1.5679 \cdot 10^{-1}$	1	2.5000
	6	$4.8003 \cdot 10^5$	$4.7650 \cdot 10^{-2}$	1	2.0000

Table 6.2: XPP parameters for different polymer melts.

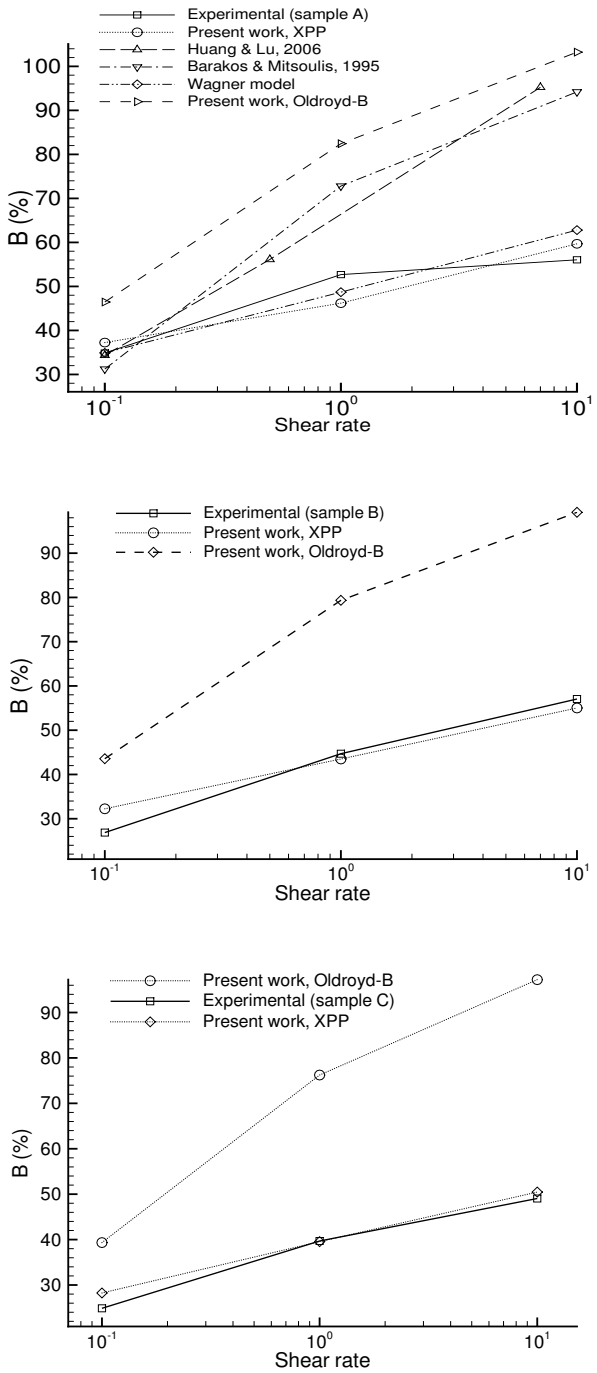

Figure 6.1: Comparison of the calculated swelling ratios with the experimental results from Meissner [80]: IUPAC-LDPE sample A (top), sample B (middle), sample C (bottom).

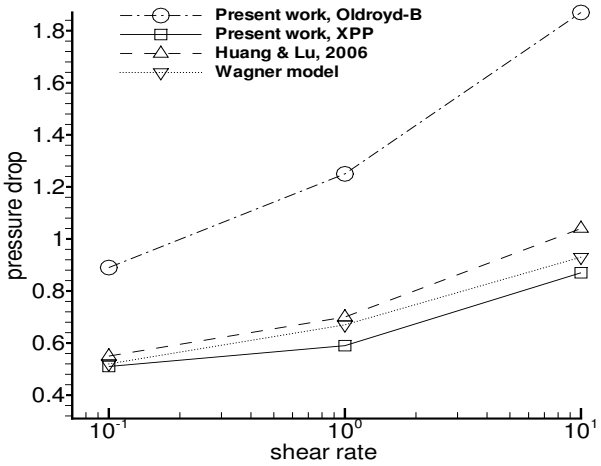

Figure 6.2: Comparison of the calculated exit pressure drops with the experimental results from Meissner [80], sample A, and predictions reported in Huang and Lu [54].

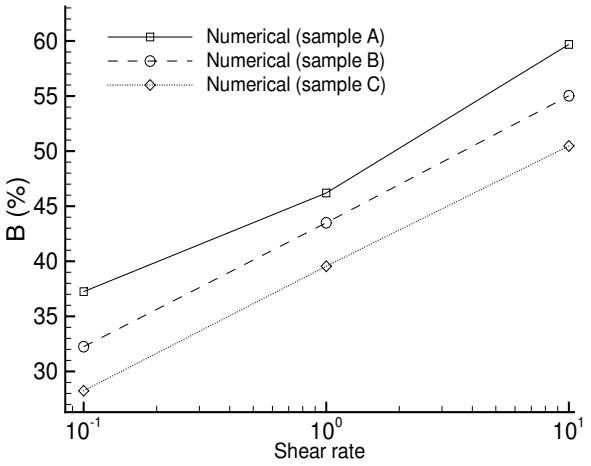

Figure 6.3: Comparison of the calculated swelling ratios for the three IUPAC samples.

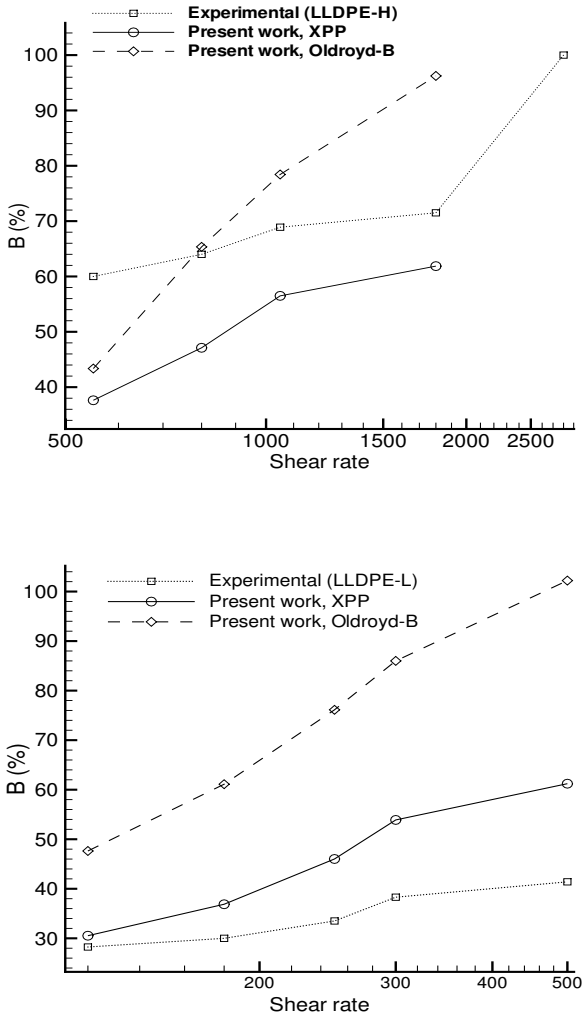

Figure 6.4: Comparison of the calculated swelling ratios with the experimental results from Yang et al. [138] : LLDPE-H (top), LLDPE-L (bottom).

samples, the discrete relaxation spectrum for sample A spans two orders of magnitude more than samples B and C. The question of whether or not this property can be systematically related to an eventual difference in polydispersity is one of the issues we are addressing in this section. A difference in behaviour between sample A and the other two samples, was detected in the experiments. According to the data in Meissner [80], it is natural to associate this difference to different weight-averaged molecular weights and molecular weight distributions. This is arguably the only discrepancy reported by Meissner [80] that can be related directly to the fluid dynamics of the LDPEs. The other two differences between the IUPAC samples are linked to the thermal stability of the melts and the amount of vinyl groups present within them. Therefore, since the numerical simulations are isothermal and the presence or absence of vinyl groups has never been reported to influence the rheological structure of a melt, it seems reasonable to consider weight-averaged molecular weights and molecular weight distributions as the only relevant source of discrepancy. Finally, the difference in melt memory index, which is actually measured through the swelling ratios, provides similar values for samples A and B, and smaller values for the sample C. However, the results reported in Meissner [80] clearly show that sample A exhibits the highest swelling ratio until a certain shear rate is reached. Then for $\dot{\gamma} = 10s^{-1}$, which is the largest shear rate employed in the experiments, sample B shows the highest value of the swelling ratio (see Fig. 12 in [80]). This feature may be due to the anisotropic effects we highlighted in the previous section. Whether or not such a switch in behaviour between samples A and B is related to the orientation characteristics of the melt is, in reality, not known. However, a couple of things can be noted from the nonlinear viscoelastic parameters q_i, r_i in Table 6.1. First, the longest relaxation time of sample A is associated with $q_1 = 22$, and is the only parameter which stands out from the others. This differentiates sample A from samples B and C, which possess similar parameters. In a way, this confirms the findings of Meissner [80]. On the other hand, even if such value could point to a difference in the isotropic behaviour of the melt, the values of r_i are very similar across the three samples. In fact, they are even in slight contrast with the observations made in the previous chapter: sample

B presents larger orientation relaxation time ratios than sample A. Therefore, for sample B, the curve of the swelling ratios against is expected to flatten with increasing shear rate. In a way, according to the viscoelastic parameters in Table 6.1, we would expect sample A and B to swap their swelling ratios! In conclusion, there is a partial difference in the parameters between the sample A and the other two samples, but no clear pattern can be recognized and such a difference it is definitely not strong enough to draw conclusions on an eventual correlation with elastic effects in extrusion.

The comparison between the values of the swelling ratios calculated through the simulations and those measured in the experiments is reported in Fig. 6.1 for the IUPAC-LDPE samples A, B and C. The results reported by Huang and Lu [54] are also included for the IUPAC sample A. They compared different K-BKZ models. The Wagner model [134], without the inclusion of a second normal stress difference, performed better than the others. We also report the results from Barakos and Mitsoulis [6], who employed the Papanastasiou-Scriven-Macosko (PSM) model [95] . Beside the clear failure of the Oldroyd-B model in reproducing the behaviour of the LDPE melts, it is also worth noticing how the predictions of Barakos and Mitsoulis, as well as those of Haung and Lu, depart from the others at larger values of the shear rate. In fact, all the K-BKZ models analyzed in [54], with the expection of the Wagner model, share the feature of overestimating the swelling ratios for $\dot{\gamma} > 1$. The better agreement of the Wagner model is likely to be attributable to its damping function being steeper than the others at larger shear rates.

The exit pressure loss is also shown in Fig. 6.2. It is obtained once again using the formula (5.6) employed in the previous chapter. Again, the values predicted by the Oldroyd-B model highly overestimate the experimental data. On the other hand, the agreement of our predictions for the XPP model with previous numerical and experimental results is reasonably good, even if, in our numerical simulations, sample A exhibits the highest swelling ratio at all shear rates, as can be seen in Fig. 6.3. It remains an open issue whether or not the switch found in the experiments in the swelling ratios

for samples A and B for $\dot{\gamma} = 10s^{-1}$ is really due to the presence of strong orientation of the polymer chains at higher flow rates. On the other hand, the numerical predictions of the swelling ratios in Fig. 6.3, together with the other simulations in Section 5.4, seem to support the hypothesis that broader relaxation spectra mimic the effect of polydispersity in extrusion.

Regarding the two samples extruded by Yang et al. [138], the low density polyethylene LLDPE-H is more polydisperse than LLDPE-L, as we can see from the values of the polydispersity indices in Table 1 in [138]. However, no substantial difference is observed between the parameters extracted from the linear LDPEs analyzed [138]. The two samples have significantly different polydispersity indices. Therefore, this does not support the hypothesis that information on polydispersity can be inferred from the relaxation parameters. However, the XPP model has been derived for branched rather than linear polymers and therefore it is not surprising that numerical simulations using the XPP model are unable to predict the experimental behaviour seen in Fig. 6.4.

6.3.1 Discussion on polydispersity and orientation

At the beginning of §5.4.2 we posed two questions: first, whether or not the discrete relaxation spectrum might be an indicator of polydispersity of the material. Second, in which way larger values of the shear rate affect the orientational relaxation process by aiding the anisotropy of the fluid. These topics are obviously related to the molecular structure of the fluid, therefore constituting two specific problems on their own, even without involving any specific fluid dynamics. However, since the swelling ratio has always been thought to be (and sometimes used as, see Meissner [80]) a measure of the memory and elasticity of a melt, it might be worth having a look at whether or not our findings can be inserted in a wider framework. In the last decade a notable amount of work has addressed to the direct and inverse problems of relating the molecular structure of polymeric liquids, and in particular their molecular mass distribution, to their rheological properties. In a series of papers Van Ruymbeke et al. [129, 128, 130, 131] embarked on the task to recover the dynamic moduli G', G'' from the molecular weight distribution for

several materials, including polystyrene, polybutadiene and poly-isoprene. Several models based on the reptation theory are investigated, and other mechanism such as fluctuation or constraint release are also considered.

On the other hand, the effect of the orientation of the macromolecules in a polymeric liquid is one of the main topics in constitutive modelling, as it is known to be one of the key relaxation processes, together with reptation, stretch and constraint release, taking place in viscoelastic fluids. From what we observed in our numerical simulations and from the experimental data it seems clear that, as far as the extrusion process is concerned and the nonlinear models that are used in the numerical simulations, these two mechanisms have to be considered together. In other words, it makes more sense to merge the two questions mentioned above, for the simple reason that the discrete relaxation times belong to the family of linear viscoelastic parameters, whereas orientation is a nonlinear process. In the XPP model, as well as in any other constitutive model based on the upper-convective derivative, the linear viscoelastic parameters are calculated practically from the theory of the linear Maxwell modes. This means that, in the limit of linear viscoelasticity, the XPP model does not differ from the UCM model. Bearing this in mind, it becomes clear that the analysis of the discrete relaxation spectrum alone cannot provide any more information than an UCM or Oldroyd-B model. However, from the molecular approach of the original pom-pom theory of McLeish and Larson [79], on which the XPP model is based, the backbone relaxation time is calculated as

$$\lambda_b = \frac{4}{\pi^2} s_b^2 \phi_b \lambda_a(0) q. \tag{6.1}$$

In Eq. (6.1), s_b is non-dimensional molecular weight of the backbone, ϕ_b is the fraction of the backbone segment which is fixed due to entanglement, $\lambda_a(0)$ is the relaxation time of the arms at the endpoints and q is the number of arms. Therefore it seems quite intuitive to associate longer relaxation times to heavier molecules. However, the conclusion that a broader relaxation spectrum corresponds to higher polydispersity is not straightforward. In fact, the IUPAC-LDPE sample A, together with other three polymer melts, IUPAC X, LDPE B and Melt 1, have been analyzed by Inkson et al.

[57] using the pom-pom model. Among these polymers, IUPAC sample A and Melt 1 have the highest polydispersity indices (22 and 24.6, respectively) and molecular weights (see Laun [66]). LDPE B is has a polydispersity index around 15. However, looking at table II, III and VI in Inkson et al. [57], IUPAC A presents parameters very similar to LDPE B rather than to Melt 1. The latter spans over 7 relaxation time decades, while the spectrum for IUPAC A and LDPE B narrows to 5 decades. What is different between IUPAC sample A and Melt 1 are the ratios $\frac{\tau_b}{\tau_s}$ between backbone orientation and stretch relaxation times, respectively. This can be seen, for instance, in Figs. 17 and 18 in [57]. In the case of sample A, these ratios are almost independent on the relaxation time, whereas for Melt 1 they decrease with increasing relaxation time. In a way, for Melt 1, the longer the mode (i.e. the heavier the molecule), the faster its orientation.

In conclusion, our simulations suggest that larger orientation relaxation times do contribute to the overall elasticity of the melt and such contribution becomes less relevant at larger shear rates. However, no clear pattern could be identified, by fitting the XPP model, in relating the corresponding viscoelastic parameters to the orientation relaxation process and polydispersity of the samples we investigated. At the end of the day, even if several procedures have been proved to be satisfactory in recovering the viscoelastic characteristics of a sample from its molecular structure (see, e.g., [129, 128, 130, 131, 21]), no clear pattern is recognized even for the distribution of the dynamic moduli G' and G''. For example, van Ruymbeke et al. [130] analyzed a vast amount of polystyrene, polybutadiene and poly-isoprene melts, with different molecular conformation (linear, star) and different polydispersity indices. The prediction of the dynamic moduli, obtained by means of a tube-based model including reptation, fluctuation and constraint release, are quite accurate, but only by looking at the master curves of G' and G'' there are no hints towards the class of polymeric liquid they belong. It would be practically impossible that such a thing would happen after fitting G' and G'' to find the corresponding discrete viscoelastic parameters.

Chapter 7

Conclusions and future work

In this thesis the die-swell problem has been investigated. The three-fields formulation of the problem has been treated in the weak form. A few remarks on this mathematical formulation have been addressed. In particular, a stability estimate for the stress tensor is proposed, following the same approach used for velocity and pressure.

The physical interpretation of the die-swell phenomenon for a Newtonian fluid has been revisited, in the attempt of supporting the well-known idea of readjustment of the velocity fields using numerical simulations specifically aimed to clarify a few aspects [109]. In particular, we numerically calculated the tensile and compressive stress in the outer and core layers of the fluid, respectively. These are the competing forces trying to expand and contract the fluid. In our simulations they seem to balance for $Re \simeq 20$. This is an important confirmation that the Newtonian swelling is entirely caused by the competition of these two components. In fact, in the experiments a value of Re around 18 has been reported as the critical swelling value, namely, the value of Re at which no swelling occurs. Moreover, if surface tension is included, the driving force which tends to minimize the curvature of the free surface acts in favour of the stress in the outer layer. However, this effect decreases with increasing Reynolds number and eventually, for Reynolds number very close to the critical swelling value, it disappears. In fact, for Reynolds number very close to the critical swelling value, the stress

balance is independent on the surface tension.

An algorithm based on the spectral element method has been implemented to predict the swelling of Newtonian and viscoelastic fluids. Two time-marching schemes are employed in the field equations, a first and second order OIFS. Both are employed for Netwonian fluids, whereas the second order is preferred in the simulations of viscoelastic fluids. Three different schemes for the update of the location of the free surface have been used in the Newtonian case. The stable, third order Adams-Bashforth scheme is retained for the simulation of the viscoelastic models. The viscoelastic models investigated are the UCM, Oldroyd-B and XPP models. Convergence with respect to temporal and spatial discretization steps has been studied for the different models. In the Newtonian case, the effects of inertia and surface tension have been considered.

As expected, the swelling ratio decreases with increasing inertia, until the aforementioned critical swelling Reynolds number is reached. Beyond it, the fluid contracts. A few simulations for larger values of Re have been also performed. The findings are in good agreement with previous works.
Last, the effect of surface tension has been investigated. The role of surface tension, through the action of the capillary forces, is to try to keep the fluid particles as aggregated as possible. Therefore, at fixed Re, the swelling ratio is less when capillary forces are present. This has also been reported in previous works. This work has been published in Computers and Fluids [111].

Numerical simulations of extrusion using UCM and Oldroyd-B models have then been performed for $We \in [0.25, 1]$. Beside swelling ratios, standard quantities related to the elasticity of the fluid, such as the normal stress difference and pressure loss, have been analyzed. They increase with increasing Weissenberg number, as expected. The agreement with previous work and the theory of Tanner [117] is reasonably good, and a few observations on the range of validity of Tanner's formula are reported. Flow fields and free surface profiles are also reported. In particular, the latter is a sensitive quantity

against which we tested the convergence properties of the algorithm.

In the last part of this thesis, the XPP model has been employed to model branched polymer melts. The single mode version has been used to test the convergence of our algorithm. Numerical simulations have then been performed over a range of different modes and parameters. Since the swelling ratio is a measure of elasticity, a link between the changes in the values of the swelling ratios and such parameters seemed intriguing. The effect of a broader discrete relaxation spectrum and larger orientation parameters have been explored. The idea that a broader discrete relaxation spectrum could represent a more polydisperse sample has been discussed. Further studies on the relation between the molecular characteristics of a sample and its rheology were analyzed, but no bottom line could be drawn. However, our simulations confirm a couple of things: first, larger orientation relaxation times do contribute to the overall elasticity of the melt, as it is predicted by all the models for entangled polymeric liquids; second, in the XPP model, such contributions becomes less relevant at larger shear rates, where the stretch mechanism is predominant. This is also evident by looking at the set of equations for the XPP model.

Several materials have also been characterized for quantitative comparisons. As expected, the XPP model predicts accurately the behaviour of branched LDPEs but fails in predicting linear LDPEs. Again, from the viscoelastic parameters, no clear pattern was discovered regarding the polydispersity of the three IUPAC LDPEs analyzed. IUPAC sample A is more polydisperse than sample B and C, and indeed displays a broader discrete relaxation spectrum. However, the behaviour of IUPAC sample A compared with the IUPAC Melt 1 discussed at the end of Chapter 6 seems to suggest a contrary behaviour. This work was presented at the 5th Annual European Rheology Conference in Cardiff, April 2009, and it is in press on Rheologica Acta in the proceedings of AERC 2009 [110]. The failure of the Oldroyd-B model in predicting the flow of polymer melts is also reported. This is well-known and is most likely due, among other things, to its inadequacy in describing extensional flow and to the absence of shear-thinning effect and mechanisms

such as entanglement and orientation, as also explained in §5.2.

Future work in the direction of this thesis would be mainly addressed to the improvement of the numerical algorithm. It could be made more dynamic, in the sense of using adaptive mesh refinement in particular regions of the domain. A parallel implementation would be extremely useful, since every single problem in each element could be diverted to a different processor and then assembled through the edges at the end of each time step. The extension to three dimensions is another option.

As far as the relationship between viscoelastic data and molecular structure of polymer melts is concerned, this has been investigated for a number of years already. It seems that no clear pattern is foreseen in relating the master curves of G' and G'' recovered from the molecular structure of the polymer to the polymer itself. In this regard some light could be shed by a systematic and homogeneous approach in fitting, understanding and testing the discrete linear and nonlinear viscoleastic parameters for different models.

Bibliography

[1] Baaijens F.T.P., Mixed finite element methods for viscoelastic flow analysis: a review, *J. Non-Newtonian Fluid Mech.* 79 (1998) 361–385.

[2] Babuška I., The finite element method with Lagrangian multipliers, *Numer. Math.* 20 (1973) 179–192.

[3] Bach A., Almdal K., Rasmussen H.K., Hassager O., Elongational viscosity of narrow molar mass distribution polystyrene, Macromolecules 36 (2003) 51745179.

[4] Bach A., Rasmussen H.K., Hassager O., Extensional viscosity for polymer melts measured in the filament stretching rheometer, *J. Rheol.* 47 (2003) 429–441.

[5] Bach A., Rasmussen H.K., Longin P.Y., Hassager O., Growth of non-axisymmetric disturbances of the free surface in the filament stretching rheometer: experiments and simulation, *J. Non-Newtonian Fluid Mech.* 108 (2002) 163–186.

[6] Barakos G., Mitsoulis E., A convergence study for the numerical simulatiions of the IUPAC-LDPE extrusion experiments, *J. Non-Newtonian Fluid Mech.* 58 (1995) 315–329.

[7] Batchelor J., Berry J.P., Horsfall F., Die swell in elastic and viscous fluid, Polymer 14 (1973) 297–299.

[8] Belblidia F., Matallah H., Puangkird B., Webster M.F., Alternative subcell discretisations for viscoelastic flow: stress interpolation, *J. Non-Newtonian Fluid Mech.* 146 (2007) 59–78.

[9] Belblidia F., Matallah H., Webster M.F., Alternative subcell discretisations for viscoelastic flow: velocity-gradient approximation, *J. Non-Newtonian Fluid Mech.* 151 (2008) 69–88.

[10] Bernardi C., Maday Y., Approximations spectrales de problémes aux limites elliptiques, Springer Verlag France, Paris, 1992.

[11] Bhattacharjee P.K., Nguyen D.A., McKinley G.H., Sridhar T., Extensional stress growth and stress relaxation in entangled polymer solutions, *J. Rheol.* 47-1 (2003) 269–290.

[12] Bird R.B., Curtiss C.F., Armstrong R.C., Hassager O., Dynamics of polymeric liquids, volume 2, John Wiley and Sons, New York, 1987.

[13] Bishko G.B., McLeish T.C.B., Harlen O.G., Nicholson T.M., Numerical simulations of the transient flow of branched polymer melts through a planar contraction using the pom-pom model, *J. Non-Newtonian Fluid Mech.* 82 (1999) 255–273.

[14] Blackwell R.J., McLeish T.C.B., Harlen O.G., Molecular drag-strain coupling in branched polymer melts, *J. Rheol.* 44-1.

[15] Bodard N., Bouffanais R., Deville M.O., Solution of moving-boundary problems by the spectral element method, *Appl. Numer. Math.* 58 (2008) 968–984.

[16] Brenner S.C., Scott L.R., The mathematical theory of finite element methods - second edition, Springer Verlag, New York, 2002.

[17] Brezzi F., On the existence, uniqueness and approximation of saddle-point problems arising from Lagrange multipliers, R.A.I.R.O. Anal. Numér. R2 8 (1974) 129–151.

[18] Brown R.A., Armstrong R.C., Beris A.N., Yeh P.W., Galerkin finite element analysis of complex viscoelastic flows, *Comput. Meth. Appl. Mech. Engrg.* 58 (1986) 201–226.

[19] Bush M.B., A numerical study of extrudate swell in very dilute polymer solutions represented by the Oldroyd-B model, *J. Non-Newtonian Fluid Mech.* 34 (1990) 15–24.

[20] Bush M.B., Milthorpe J.F., Tanner R.I., Finite element and boundary element methods for extrusion computations, *J. Non-Newtonian Fluid Mech.* 19 (1984) 37–51.

[21] Carrot C., Guillet J., From dynamic moduli to molecular weight distribution: A study of various polydisperse linear polymers, *J. Rheol.* 41 (1997) 1203–1220.

[22] Chandio M.S., Matallah H., Webster M. F., Numerical simulations of viscous filament strecthing flow, Int. Journal Num. Meth. Heat Fluid Flow 12 (2003) 899–930.

[23] Chang P.W., Patten T.W., Finlayson B.A., Collocation and Galerkin finite element methods for viscoelastic flui flow - ii : die swell problems with a free surface, *Comput. Fluids* 7 (1979) 285–293.

[24] Chilcott M.D., Rallison J.M., Creeping flow of dilute polymer solutions past cylinders and spheres, *J. Non-Newtonian Fluid Mech.* 29 (1988) 381–432.

[25] Ciarlet P.G., The finite element method for elliptic problems, North Holland, Amsterdam, 1978.

[26] Clemeur N., Rutgers R.P.G., Debbaut B., Numerical simulation of abrupt contraction flows using the Double Convected PomPom model, *J. Non-Newtonian Fluid Mech.* 117 (2004) 193–209.

[27] Clermont J.R., Normandin M., Numerical simulation of extrudate swell for Oldroyd-B fluids using the stream-tube analysis and a streamline approximation, *J. Non-Newtonian Fluid Mech.* 50 (1993) 193–215.

[28] Crochet M.J., Keunings R., Die swell of a Maxwell fluid: numerical prediction, *J. Non-Newtonian Fluid Mech.* 7 (1980) 199–212.

[29] Crochet M.J., Keunings R., Finite element analysis of die swell of a highly elastic fluid, *J. Non-Newtonian Fluid Mech.* 10 (1982) 339–356.

[30] Dangtungee R., Desai S.S., Tantayanon S., Supaphol P., Melt rheology and extrudate swell of low-density polyethylene/ethyleneoctene copolymer blends, *Polymer Testing* 25 (2006) 888–895.

[31] Dangtungee R., Yun J., Supaphol P., Melt rheology and extrudate swell of calcium carbonate nanoparticle-filled isotactic polypropylene, *Polymer Testing* 25 (2005) 2–11.

[32] Den Doelder C.F.J., Koopmans R.J., The effect of molar mass distribution on extrudate swell of linear polymers, *J. Non-Newtonian Fluid Mech.* 152 (2007) 195–202.

[33] Doi M., Edwards S.F., The theory of polymer dynamics, Oxford University Press, Oxford, 1988.

[34] Fattal R., Kupferman R., Constitutive laws for the matrix-logarithm of the conformation tensor, *J. Non-Newtonian Fluid Mech.* 123 (2004) 281–285.

[35] Fattal R., Kupferman R., Time-dependent simulation of viscoelastic flows at high Weissenberg number using the log-conformation representation, *J. Non-Newtonian Fluid Mech.* 126 (2005) 23–37.

[36] Fischer P.F., An overlapping Shcwarz method for spectral element solution of the incompressible Navier-Stokes equations, *J. Comput. Phys.* 133 (1997) 84–101.

[37] Fortin M., Fortin A., A new approach for the FEM simulation of viscoelastic flows, *J. Non-Newtonian Fluid Mech.* 32 (1989) 295–310.

[38] Georgiou G.C., Boudouvis A.G., Converged solutions of the Newtonian xtrudate-swell problem, *Int. J. Numer. Meth. Fluids* 29 (1999) 363–371.

[39] Gerritsma M.I., Phillips T.N., Discontinuous spectral element approximations for the velocity-pressure-stress formulation of the Stokes problem, *Int. J. Numer. Meth. Engrg.* 43 (1998) 1401–1419.

[40] Gerritsma M.I., Phillips T.N., Compatible spectral approximation for the velocity-pressure-stress formulation of the Stokes problem, *SIAM J. Sci. Comput.* 20 (1999) 1530–1550.

[41] Gerritsma M.I., Phillips T.N., Compatible approximation spaces for the velocity-pressure-stress formulation for creeping flows, *Appl. Numer. Math.* 33 (2000) 225–231.

[42] Gordon W.J., Hall C.A., Construction of curvilinear co-ordinate systems and applications to mesh generation, *Int. J. Numer. Meth. Engrg.* 7 (1973) 461–477.

[43] Goren S.L., Wronski S., The shape of low speed capillary jets of Newtonian liquids, *J. Fluid Mech.* 25 (1966) 185–198.

[44] Gould P.L., Introduction to linear elasticity, Springer-Verlag, New York, 1983.

[45] Graessley W.W., Entangled linear, branched and network polymer systems - molecular theories, Adv. Polym. Sci. 47 (1982) 67–117.

[46] Graham S.G., Likhtman A.E., McLeish T.C.B., Milner S.T., Microscopic theory of linear, entangled polymer chains under rapid deformation including chain stretch and convective constraint release, *J. Rheol.* 47 (2003) 1171–1200.

[47] Harlen O.G., Hinch E.J., Rallison J.M., Birefringent pipes: the steady flow of a dilute polymer solution near a stagnation point, *J. Non-Newtonian Fluid Mech.* 44 (1992) 229–265.

[48] Hassager O., Kolte M.I., Renardy M., Failure and non-failure of fluid filaments in extension, *J. Non-Newtonian Fluid Mech.* 98 (1998) 137–151.

[49] Hinch E.J., The flow of an Oldroyd fluid around a sharp corner, *J. Non-Newtonian Fluid Mech.* 50 (1993) 161–171.

[50] Ho L., Patera A.T., A Legendre spectral element method for simulation of unsteady incompressible viscous free-surface flow, *Comput. Meth. Appl. Mech. Engrg.* 80 (1989) 355–366.

[51] Ho L., Patera A.T., Variational formulation of three dimensional viscous free-surface flow: natural imposition of surface tension boundary conditions, *Int. J. Numer. Meth. Fluids* 13 (1991) 691–698.

[52] Ho L., Rønquist E.M., Spectral element solution of steady incompressible viscous free-surface flows, Finite Element in Analysis and Design 16 (1994) 207–227.

[53] Horsfall F., A theoretical treatment of die-swell in a Newtonian liquid, Polymer 14 (1973) 262–266.

[54] Huang S.X., Lu C.J., Stress relaxation characteristics and extrudate swell of the IUPAC-LPDE melt, *J. Non-Newtonian Fluid Mech.* 136 (2006) 147–156.

[55] Hulsen M.A., Fattal R., Kupferman R., Flow of viscoelastic fliuds past a cylinder at high Weissenberg number: stabilized simulations using matrix logarithms, *J. Non-Newtonian Fluid Mech.* 127 (2005) 27–39.

[56] Ianniruberto G., Marrucci G., A 2-D model for tube orientation and tube squeezing in fast flows of polymer melts, *J. Non-Newtonian Fluid Mech.* 128 (2005) 42–49.

[57] Inkson N.J., McLeish T.C.B., Harlen O.G., Groves D.J., Predicting low density polyethylene rheology in flows and shear with pom-pom constitutive equation, *J. Rheol.* 43 (1999) 873–896.

[58] Inkson N.J., Phillips T.N., Unphysical phenomena associated with the extended pom-pom model in steady flow, *J. Non-Newtonian Fluid Mech.* 145 (2007) 92–101.

[59] Jay P., Piau J.M., El Kissi N., Cizeron J., The reduction of viscous extrusion stresses and extrudate swell computation using slippery exit surfaces, *J. Non-Newtonian Fluid Mech.* 79 (1998) 599–617.

[60] Joseph D.D., Fluid dynamics of viscoelastic liquids, Springer-Verlag, New York, 1990.

[61] Karniadakis G.E., Sherwin S.J., Spectral/hp element methods for CFD, 2nd Edition, Oxford University Press, 2005.

[62] Keunings R., Simulation of viscoelastic fluid flow, C.L. Tucker, editor, Computer Modeling for Polymer Processing, Hanser, Munich, 1989, pp. 404–469.

[63] Keunings R., On the Peterlin approximation for finitely extensible dumbbells, *J. Non-Newtonian Fluid Mech.* 68-1 (1998) 85–100.

[64] Landau L.D., Lifshitz E.M., Fluid Mechanics, Course of theoretical Physics, vol.6, Pergamon Press, 1959.

[65] Larson R.G., Constitutive equations for polymer melts and solutions, Butterworth, 1988.

[66] Laun H.M., Prediction of elastic strains in polymer melts in shear and elongation, *J. Rheol.* 30(3) (1986) 459–501.

[67] Li X.K., Gwynllyw D.R., Davies A.R., Phillips T.N., On the influence of lubricant properties on the dynamics of two-dimensional journal bearings, *J. Non-Newtonian Fluid Mech.* 93 (2000) 29–59.

[68] Liang J., Estimation of the die swell ratio for polymer melts from exit pressure drop data, *Polymer Testing* 20 (2001) 29–31.

[69] Liang J., Characteristics of melt shear viscosity during extrusion of polymers, *Polymer Testing* 21 (2002) 307–311.

[70] Liang J., The elastic behaviour during capillary extrusion of LDPE/LLDPE blend melts, *Polymer Testing* 21 (2002) 69–74.

[71] Liang J., A relationship between extrudate swell ratio and entry stored elastic strain energy during die flow of tyre compounds, *Polymer Testing* 23 (2004) 441–446.

[72] Likhtman A.E., Graham S.G., Simple constitutive equation for linear polymer melts derived from molecular theory: Roliepoly equation, *J. Non-Newtonian Fluid Mech.* 114 (2003) 1–12.

[73] Maday Y., Patera A. T., Rønquist E.M., The $P^N \times P^{N-2}$ method for the approximation of the Stokes problem, Tech. rep., Laboratoire d'Analyse Numrique, Universitit Pierre et Marie Curie (1992).

[74] Maday Y., Patera A.T., Rønquist E.M., An operator-integration-factor splitting method for time-dependent problems: application to incompressible fluid flow, *J. Sci. Comput.* 5 (1990) 263–292.

[75] Marrucci G., Dynamics of entanglements: a nonlinear model consistent with the Cox-Merz rule, *J. Non-Newtonian Fluid Mech.* 62 (1996) 279–289.

[76] Marrucci G., Ianniruberto G., Interchain pressure effect in extensional flows of entangled polymer melts, Macromolecules 37 (2004) 39343942.

[77] Matallah H., Banaai M.J., Sujatha K.S., Webster M.F., Modelling filament stretching flows with strain-hardening models and sub-cell approximations, *J. Non-Newtonian Fluid Mech.* 134 (2006) 77–104.

[78] McKinley G.H., Hassager O., The Considère condition and rapid stretching of linear and branched polymer melts, *J. Rheol.* 43 (1999) 1195–1212.

[79] McLeish T.C.B., Larson R.G., Molecular constitutive equations for a class of branched polymers: the pom pom polymer, *J. Rheol.* 42 (1998) 81–110.

[80] Meissner J., Basic parameters, melt rheology, processing and end-use properties of three similar low density polyethylene samples, Pure and Applied Chemistry 42 (1975) 552–612.

[81] Mendelson M.A., Yeh P.W., Brown R.A., Armstrong R.C, Approximation error in finite element calculation of viscoelastic fluid flows, *J. Non-Newtonian Fluid Mech.* 10 (1982) 31–54.

[82] Metzner A.B., Houghton W.T., Sailor R.A., White J.L., A method for the measurement of normal stresses in simple shearing flow, Trans. of the Soc. of Rheol. 5 (1961) 133–147.

[83] Michael D.H., The separation of a viscous liquid at a straight edge, Mathematika 5 (1958) 82.

[84] Middleman S., Gavis J., Expansion and contraction of capillary jets of Newtonian liquids, *Phys. Fluids* 4 (1961) 355–367.

[85] Mitsoulis E., Three-dimensional non-Newtonian copmutations of extrudate swell with the finite element method, *Comput. Meth. Appl. Mech. Engrg.* 180 (1999) 333–344.

[86] Nickell R.E., Tanner R.I., Caswell B., The solution of viscous incompressible jet and free surface flows using finite element methods, *J. Fluid Mech.* 65 (1974) 189–206.

[87] Nielsen J.K., Rasmussen H.K., Hassager O., Stress relaxation of narrow molar mass distribution polystyrene following uniaxial extension, *J. Rheol.* 52 (2008) 885–899.

[88] Nielsen J.K., Rasmussen H.K., Hassager O., McKinley G.H., Elongational viscosity of monodisperse and bidisperse polystyrene melts, *J. Rheol.* 50 (2006) 453–476.

[89] Noll W., A mathematical theory of the mechanical behaviour of continuous media, Arch. Rat. Mech. Anal. 2 (1958) 197–226.

[90] Oldroyd J.G., On the formulation of rheological equations of state, Proceedings of the Royal Society of London. Series A, Mathematical and Physical Sciences 200-1063 (1950) 523–541.

[91] Omodei B.J., Computer solutions of a plane Newtonian jet with surface tension, *Comput. Fluids* 7 (1979) 275–289.

[92] Omodei B.J., On the die-swell of an axysimmetric Newtonian jet, *Comput. Fluids* 8 (1980) 275–289.

[93] Owens R.G, Chauvière C., Phillips T.N., A locally-upwinded spectral technique (LUST) for viscoelastic flow, *J. Non-Newtonian Fluid Mech.* 108 (2002) 49–71.

[94] Owens R.G., Phillips T.N., Computational Rheology, Imperial College Press, 2002.

[95] Papanastasiou A.C., Scriven L.E., Macosko C.W., An integral constitutive equations for mixed flows: viscoelastic characterization, *J. Rheol.* 27(4) (1983) 387–410.

[96] Patera A. T., A spectral element method for fluid dynamics: laminar flow in a channel expansion, *J. Comput. Phys.* 54 (1984) 468–488.

[97] Peterlin A., Hydrodynamics of macromolecules in a velocity field with longitudinal gradient, J. Polym. Sci., Polym. Lett. 4B (1966) 287–291.

[98] Phan-Thien N., Tanner R.I., A new constitutive equation derived from network theory, *J. Non-Newtonian Fluid Mech.* 2 (1977) 353–365.

[99] Pnueli D., Gutfinger C., Fluid Mechanics, Cambridge University Press, Cambridge, 1992.

[100] Rasmussen H.K., Nielsen J.K., Bach A., Hassager O., Viscosity overshoot in the start-up of uniaxial elongation of low density polyethylene melts, *J. Rheol.* 49-2 (2005) 369–381.

[101] Rasmussen H.K.and Hassager O., Three dimensional simulations of viscoelastic instability in polymeric filament, *J. Non-Newtonian Fluid Mech.* 82 (1999) 189–202.

[102] Reddy K.R., Tanner R.I., Finite element approach to die-swell problem of non-Newtonian fluids, in: Proc. 6th Aust. Hydraulics and Fluid Mech. Conf., Adelaide, Australia, 5-9 Dec, 1977, pp. 431–434.

[103] Reddy K.R., Tanner R.I., Notes: on the swelling of extrudate plane sheets, *J. Rheol.* 22 (1978) 661–665.

[104] Renardy M., A matched solution for corner flow of the upper convected Maxwell fluid, *J. Non-Newtonian Fluid Mech.* 58 (1995) 83–89.

[105] Richardson S., The die swell phenomenon, *Rheol. Acta* 9 (1970) 193–199.

[106] Richardson S., A stick-slip problem related to the motion of a free jet at low Reynolds number, *Proc. Camb. Phil. Soc.* 67 (1970) 477.

[107] Ruschak K.J., A method for incorporating free boundaries with surface tension in finite element fluid-flow simulation, *Int. J. Numer. Meth. Engrg.* 15 (1980) 639–648.

[108] Russo G., Phillips T.N., Spectral element simulations of extrudate swell of polymer solutions using the UCM and Oldroyd-B models, in preparation.

[109] Russo G., Phillips T.N., Die swell of a planar Newtonian jet: influence of stress jump at exit, Submitted to Theor. Comput. Fluid Dynamics.

[110] Russo G., Phillips T.N., Numerical prediction of extrudate swell of branched polymer melts, Rheol. Acta, In press, DOI: 10.1007/s00397-009-0426-0.

[111] Russo G., Phillips T.N., Numerical simulations of steady plane die swell for a Newtonian fluid using spectral elements method, *Comput. Fluids* 39 (2010) 780–792.

[112] Salamon T.R., Bornside D.E., Armstrong R.C., Brown R.A., The role of surface tension in the dominant balance in the die swell singularity, *Phys. Fluids* 7 (1995) 2328–2344.

[113] Schwab C., *p*- and *hp*- Finite Element Methods, Theory and Applications in Solid and Fluid Mechanics, Oxford University Press, New York, 1998.

[114] Spiegelberg S.H., Ables D.C., McKinley G.H., The role of end-effects on measurements of extensional viscosity in filament stretching rheometers, *J. Non-Newtonian Fluid Mech.* 64 (1996) 229–267.

[115] Spiegelberg S.H., McKinley G.H., Stress relaxation and elastic decohesion of viscoelastic polymer solutions in extensional flow, *J. Non-Newtonian Fluid Mech.* 67 (1996) 49–76.

[116] Sujatha K.S., Matallah H., Banaai M.J., Webster M.F., Computational prediction for viscoelastic filament stretching flows: ALE methods and free-surface techniques (CM and VOF), *J. Non-Newtonian Fluid Mech.* 137 (2006) 81–102.

[117] Tanner R.I., A theory of die swell, *J. Polymer Science* A8 (1970) 2067–2078.

[118] Tanner R.I., A new inelastic theory of extrudate swell, *J. Non-Newtonian Fluid Mech.* 6 (1980) 289–302.

[119] Tanner R.I., Engineering Rheology - 2nd Edition, Oxford University Press, Oxford, 2002.

[120] Tanner R.I., A theory of die swell revisited, *J. Non-Newtonian Fluid Mech.* 129 (2005) 85–87.

[121] Tanner R.I., Huang X., Stress singularities in non-Newtonian stick-slip and edge flows, *J. Non-Newtonian Fluid Mech.* 50 (1993) 135–160.

[122] Tirtaatmadja V., Sridhar T., A filament stretching device for measurement of extensional viscosity, *J. Rheol.* 37 (1993) 1081–1102.

[123] Tirtaatmadja V., Sridhar T., Comparison of constitutive equations for polymer solutions in uniaxial extension, *J. Rheol.* 36-9 (1995) 1133–1160.

[124] Tomé M.F., Grossi L., Castelo A., Cuminato J.A., McKee S., Walters K., Die-swell, splashing drop and a numerical technique for solving the Oldroyd B model for axisymmetric free surface flows, *J. Non-Newtonian Fluid Mech.* 141 (2007) 148–166.

[125] Tomé M.F., Mangiavacchi N., Cuminato J.A., Castelo A., McKee S., A finite difference technique for simulating unsteady viscoelastic free surface flows, *J. Non-Newtonian Fluid Mech.* 106 (2002) 61–106.

[126] Tuna N.Y., Finlayson B.A., Exit pressure calculations from numerical extrudate swell results, *J. Rheol.* 28 (1984) 79–93.

[127] Van Os R.G.M., Spectral element methods for predicting the flow of polymer solutions and melts, Ph.D. thesis, University of Wales, Aberystwyth (September 2004).

[128] van Ruymbeke E., Bailly C., Keunings R.and Vlassopoulos D., A general methodology to predict the linear rheology of branched polymers, Macromolecules 39 (2006) 6248–6259.

[129] van Ruymbeke E., Kapnistos M., Vlassopoulos D., Huang T., Knauss D.M., Linear melt rheology of pom-pom polystyrenes with unentangled branches, Macromolecules 40 (2007) 1713–1719.

[130] van Ruymbeke E., Keunings R., Bailly C., Prediction of linear viscoelastic properties for polydisperse mixtures of entangled star and

linear polymers: Modified tube-based model and comparison with experimental results, *J. Non-Newtonian Fluid Mech.* 128 (2005) 7–22.

[131] van Ruymbeke E., Keunings R., Stéphenne V., Hagenaars A., Bailly C., Evaluation of reptation models for predicting the linear viscoelastic properties of entangled linear polymers, Macromolecules 35 (2002) 2689–2699.

[132] Verbeeten W.M.H., Peters G.W.M., Baaijens F.P.T., Differential constitutive equations for polymer melts: the extended pom-pom model, *J. Rheol.* 45-4 (2001) 823–843.

[133] Verbeeten W.M.H., Peters G.W.M., Baaijens F.P.T., Viscoelastic analysis of complex polymer melt flows using the eXtended PomPom model, *J. Non-Newtonian Fluid Mech.* 108 (2002) 301–326.

[134] Wagner M.H., Analysis of time-dependent non-linear stress-growth data for shear and elongational flow of a low-density branched polyethylene melt, *Rheol. Acta* 15 (1976) 136–142.

[135] Warner H.R., Kinetic theory and rheology of dilute suspensions of finitely extendible dumbbells, Industrial and Engineering Chemistry Fundamentals 11 (1972) 379–387.

[136] Waters N.D., King M.J., Unsteady flow of an elastico-viscous liquid, *Rheol. Acta* 9 (1970) 345–355.

[137] Webster M.F., Matallah H., Sujatha K.S., Sub-cell approximations for viscoelastic flows - filament stretching, *J. Non-Newtonian Fluid Mech.* 126 (2005) 187–205.

[138] Yang X., Wang S., Chai C., Extrudate swell behaviour of polyethylenes: capillary flow, wall slip, entry/exit effects and low temperature anomalies, *J. Rheol.* 42 (1998) 1075–1094.

[139] Yao M., McKinley G.H., Numerical simulation of extensional deformation of viscoelastic liquid bridges in filament stretching devices, *J. Non-Newtonian Fluid Mech.* 74 (1998) 47–88.

[140] Yao M., McKinley G.H, Debbaut B., Extensional deformation, stress relaxation and necking failure of viscoelastic filaments, *J. Non-Newtonian Fluid Mech.* 79 (1998) 469–501.

[141] Yao M., Spiegelberg S.H, McKinley G.H., Dynamics of wakly strain-hardening fluids in filament stretching devices, *J. Non-Newtonian Fluid Mech.* 89 (2000) 1–43.

[142] Yoo J.Y, Na Y., A numerical study of the planar contraction flow of a viscoelastic fluid using the SIMPLER algorithm, *J. Non-Newtonian Fluid Mech.* 30 (1991) 89–106.

[143] Yuan X.F., Ball R.C., Edwards S.F., Dynamical modelling of viscoelastic extrusion flow, *J. Non-Newtonian Fluid Mech.* 54 (1994) 423–435.

[144] Zhu Z., Wang S., Experimental characterization of extrudate swell behaviour of linear polybutadiene, *J. Rheol.* 48 (2004) 571–589.